Journal of
Instrumentation

PAPER • **OPEN ACCESS**

Operation and performance of the CMS silicon strip tracker with proton-proton collisions at the CERN LHC

To cite this article: A. Hayrapetyan *et al* 2025 *JINST* **20** P08027

Published by IOP Publishing for Sissa Medialab

Received: *June 20, 2025*
Accepted: *July 8, 2025*
Published: *August 20, 2025*

Operation and performance of the CMS silicon strip tracker with proton-proton collisions at the CERN LHC

The CMS collaboration

E-mail: `cms-publication-committee-chair@cern.ch`

Abstract: Salient aspects of the commissioning, calibration, and performance of the CMS silicon strip tracker are discussed, drawing on experience during operation with proton-proton collisions delivered by the CERN LHC. The data were obtained with a variety of luminosities. The operating temperature of the strip tracker was changed several times during this period and results are shown as a function of temperature in several cases. Details of the system performance are presented, including occupancy, signal-to-noise ratio, Lorentz angle, and single-hit spatial resolution. Saturation effects in the APV25 readout chip preamplifier observed during early Run 2 are presented, showing the effect on various observables and the subsequent remedy. Studies of radiation effects on the strip tracker are presented both for the optical readout links and the silicon sensors. The observed effects are compared to simulation, where available, and they generally agree well with expectations.

Keywords: Large detector systems for particle and astroparticle physics; Particle tracking detectors; Particle tracking detectors (Solid-state detectors)

ArXiv ePrint: 2506.17195

https://doi.org/10.1088/1748-0221/20/08/P08027

Contents

1 Introduction

The silicon strip tracker (SST) of the CMS experiment [1] at the CERN LHC [2] is the world's largest silicon-based detector with an active area of 200 m^2. The SST detects charge deposits (hits) at discrete points along the paths of charged particles arising from the collisions produced by the LHC. These hits, together with those detected in the CMS pixel detector [1, 3–5], are used to reconstruct the trajectories of charged particles traversing the detector. Because of the bending of the particle trajectories in the 3.8 tesla field of the CMS solenoid magnet, the transverse momenta of the particles are measured. The SST was initially proposed in 1997 [3] as a part of a larger tracker featuring micro-strip gas chambers, but the central tracker was changed to an all-silicon design in the year 2000 [6]. It was assembled and tested at the Tracker Integration Facility at CERN [7, 8], installed in CMS in late 2007, and subsequently commissioned in 2008 [9].

The LHC started data operation with proton-proton (pp) collisions at 7 TeV in early 2010. The center-of-mass energy was increased to 8 TeV in 2012. After the LHC Long Shutdown 1 (LS1), during the years 2013–14, the LHC restarted at an increased center-of-mass energy of 13 TeV . The data-taking period 2010–2012 is commonly referred to as LHC Run 1, the years 2015–2018 as LHC Run 2. During Run 1 the bunch spacing in the LHC machine was 50 ns. During Run 2 the bunch spacing was reduced to its design value of 25 ns, after an initial period of about 6 weeks with 50 ns bunch spacing. The peak instantaneous luminosity to which the SST has been exposed has changed by orders of magnitude from a few $10^{32}\,\mathrm{cm}^{-2}\,\mathrm{s}^{-1}$ during 2010 to up to a maximum of $2.13 \times 10^{34}\,\mathrm{cm}^{-2}\,\mathrm{s}^{-1}$ during 2018, more than twice the design luminosity, as shown in figure 1. The mean number of pp collisions (pileup) in a single LHC bunch crossing was around 31 during the years 2017 and 2018, with the tails of the pileup distribution extending to values around 70. The total integrated luminosity of pp collisions delivered to CMS in Runs 1 and 2 was $192.3\,\mathrm{fb}^{-1}$. At the time of publication, LHC Run 3 is ongoing at a center-of-mass energy of 13.6 TeV . The SST was designed for a total integrated luminosity of $500\,\mathrm{fb}^{-1}$ and a lifetime of at least 10 years with no ability to access the detector for maintenance during this time.

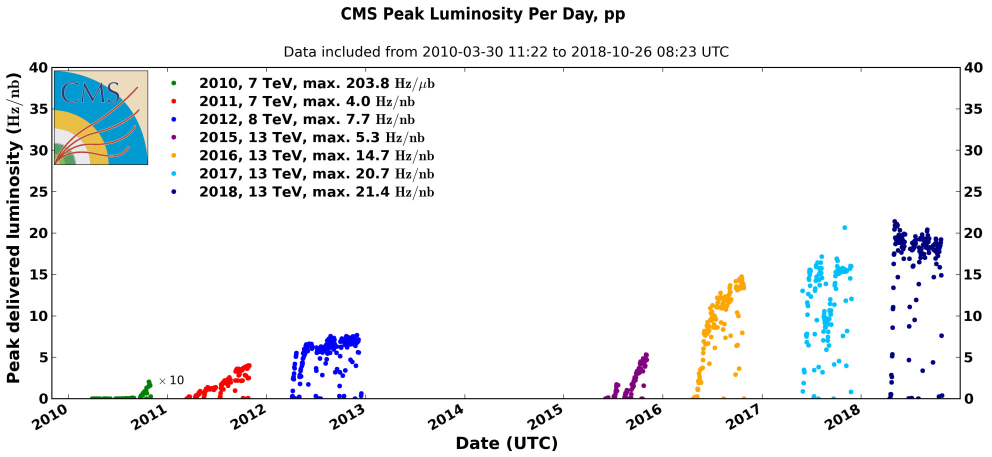

Figure 1. Peak luminosity delivered to CMS during stable pp collisions for 2010–2012 and 2015–2018, as a function of time [10]. The luminosity for the year 2010 is multiplied by a factor of 10.

This paper covers the years of data taking up to the start of the LHC Long Shutdown 2 (LS2) in late 2018 and is organized as follows. A brief overview of the SST and the detector status at the start of LS2 is given in sections 2 and 3. A description of the calibration procedures and the variation of system properties such as optical link gain and noise is shown for different operating temperatures in section 4. In section 5, the ingredients necessary to simulate collision events in the SST and model its performance are described. The performance of the SST with LHC collisions, including quantities such as occupancy, hit efficiency, and the signal-to-noise ratio, is shown in section 6. Section 7 is dedicated to the description of radiation effects in the SST, their change with time and integrated

2025 JINST 20 P08027

luminosity, as well as studies of the longevity of the existing tracker until the end of Run 3, when it is expected to be replaced. A summary and an outlook for the future of the SST are given in section 8. A glossary is supplied in section A for special terms and acronyms used in this paper. A description of the track and vertex reconstruction performance with the full CMS tracking system in Run 1 is given in ref. [11]. Some results prepared for this paper have already been made public in ref. [12].

2 Overview of the silicon strip tracker

The SST is located at the center of the CMS experiment inside the solenoidal magnet, which provides a homogeneous magnetic field of 3.8 T parallel to the beam line. The inner bore of the SST houses the CMS pixel detector. The original CMS pixel detector [1, 3] was operated during the years 2009 to 2016. It was replaced by the Phase-1 pixel detector [4, 5] in 2017. The SST is surrounded by the electromagnetic and hadron calorimeters, which are also placed inside the solenoid, and the steel flux-return yoke of the magnet is instrumented with muon chambers. A more detailed description of the CMS apparatus is report in refs. [1, 12].

The kinematic variables and spatial coordinates relevant for this paper are described in the following. CMS uses a right-handed coordinate system with the origin at the nominal interaction point inside the experiment. The x axis points towards the center of the LHC ring, the y axis points upwards (perpendicular to the LHC plane), and the z axis points along the beam line in the direction of the counter-clockwise circulating beam. The azimuthal angle ϕ is measured from the x axis in the x-y plane, and the radial coordinate in this plane is denoted by r. The polar angle θ is measured from the z axis. The pseudorapidity is defined as $\eta = -\ln\tan(\theta/2)$.

The SST occupies a cylindrical volume of 6 m in length and 2.2 m in diameter around the beam line. It is composed of 15 148 individual silicon detection modules comprising 9.3 million readout strips. An r-z view of the SST is shown in figure 2. The barrel section of the SST consists of the tracker inner barrel (TIB) and the tracker outer barrel (TOB), composed of 4 and 6 concentric layers of silicon modules, respectively. The strips in the TIB and TOB are oriented parallel to the beam line, enabling a precise measurement of the r-ϕ coordinate of a charged-particle track. The first two layers of both TIB and TOB are made of “stereo modules”, where two independent silicon modules are mounted back-to-back with the sensor strips in the second module at a 100 mrad “stereo” angle to enable a three-dimensional point reconstruction. The SST is complemented in the forward region by the two small tracker inner disk (TID) subdetectors and the larger tracker endcaps (TECs). On each side of the barrel region, the TID consists of three disks each with three rings of modules. Each of the two TECs consist of 9 disks; the number of rings decreases from 7 in the first three disks to 4 in disk 9 to reduce the number of silicon modules while ensuring coverage for $|\eta| < 2.5$. The rings 1 and 2 of the TID and rings 1, 2, and 5 of the TEC also contain stereo modules. The modules in the TID and the TEC are wedge-shaped with the strips pointing radially outwards from the nominal beam line to enable a precise measurement in ϕ. Within each layer, modules are arranged so that there is a small overlap between neighboring modules. This arrangement ensures full acceptance and allows the use of tracks passing through overlapping modules for alignment purposes and other studies that benefit from a short extrapolation distance. The SST can reconstruct tracks with transverse momenta upward of a few hundred MeV with full efficiency being reached from around 1 GeV.

The control and readout system of the SST is shown in figure 3. The basic building blocks of the detector are the detector modules. These contain the silicon sensors, the APV25 front-

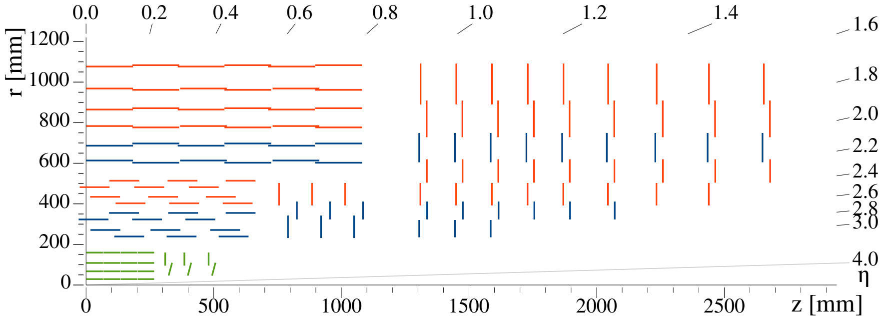

Figure 2. An r-z view of one quarter of the CMS silicon strip tracker. Layers with stereo modules (details are given in the main text) are drawn as blue lines, layers with single modules as red lines. The Phase-1 pixel detector, installed in 2017, is shown in green.

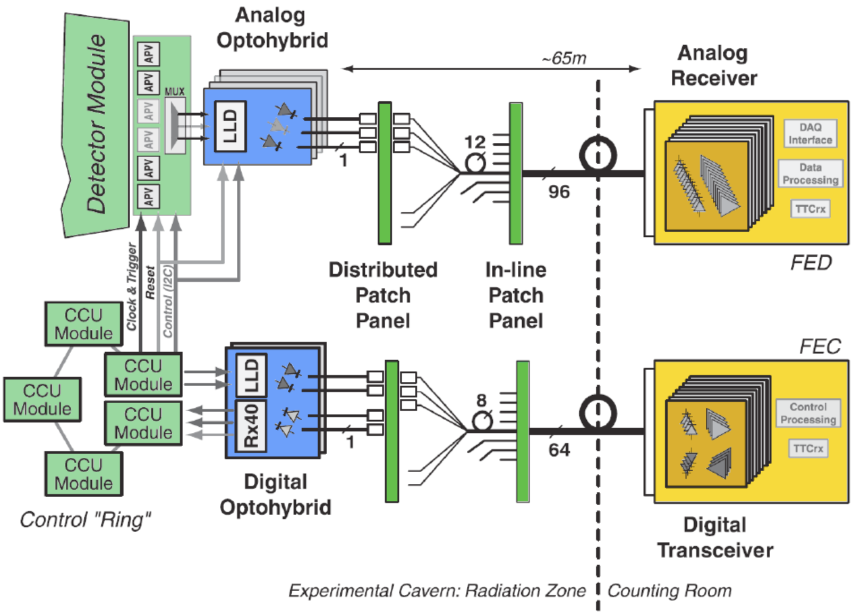

Figure 3. Overview of the control and readout scheme of the SST.

end chips [13], and other auxiliary application-specific integrated circuits (ASIC) for readout and monitoring. The detector module readout is performed via an optical link. The data from pairs of APV25 chips are time-multiplexed and passed to a Linear Laser Driver (LLD) [14], located on an Analog Optohybrid (AOH) [15], which sends the data via an optical fiber to the Front-End Driver (FED) back-end boards [16] located in the service cavern. The modules are controlled by Communication and Control Units (CCUs) [17], which are electrically daisy-chained into control rings. The control information is sent from Front-End Controller (FEC) boards [18], also located in the service cavern, via a bi-directional digital optical link to a Digital Optohybrid (DOH) [15] that serves as an entry to, and exit from, a control ring.

Silicon strip detector modules. The SST detector module consists of one or two silicon strip sensors and a front-end hybrid (FEH) printed circuit board, which houses the readout and auxiliary electronics, on a light-weight carbon fiber frame. The silicon sensors are of the float-zone p-in-n type, with a uniform n^{++} back-side implant with phosphorous doping for the n-bulk material. The unprecedented scale of the CMS SST prompted the move from 4 inch to 6 inch diameter wafers, and a ⟨100⟩ lattice orientation was chosen [19] since this was shown to result in improved radiation tolerance of the surface interface layer [20]. The spacing between the individual p^{+} implants of the readout strips (pitch) varies between 80 and 205 μm, depending on the radial position in the tracker, with the pitch mostly increasing with radius. The readout strip is connected via a polysilicon bias resistor to a p^{+} bias ring, held at ground, which also defines the active area of the sensor. A high voltage bias supply is connected to the aluminum-covered, deep-diffused n^{++} layer of approximately 20–30 μm thickness that provides a robust barrier to charge injection. In the inner parts of the tracker, silicon sensors of 320 μm thickness are used, referred to as "thin" in the following. In the outer parts of the tracker (TOB and rings 5–7 of the TECs), where occupancy and radiation exposure are lower, two silicon sensors are daisy-chained to increase the cell size to about 20 cm in length. To maintain a sufficiently high signal-to-noise ratio, 500 μm thick silicon sensors, referred to as "thick" in the following, are used for those modules.

The p^{+} implants of the individual strips are covered by a thin silicon oxide and nitride multilayer and overlaid by an aluminum strip. This structure serves as a capacitor that AC-couples signals from the sensor to the 128 individual inputs of an APV25 chip. To enable the connection of the different sensor pitches to the APV25 chip pitch, glass pitch adapters are used. A detector module has either 512 or 768 strips and is read out by either four or six APV25 chips. Modules with six APV25 chips are used to instrument TIB layers 1 and 2, TOB layers 5 and 6, TID rings 1 and 2, and TEC rings 1, 2, and 5. All other layers/rings have modules with four APV25 chips. Pictures of all SST module types can be seen in figure 4. A summary of the strip pitch for different detector locations, as well as the number of APV25 chips per module is given in table 1. More details about the physical dimensions of the silicon sensors are reported in ref. [19].

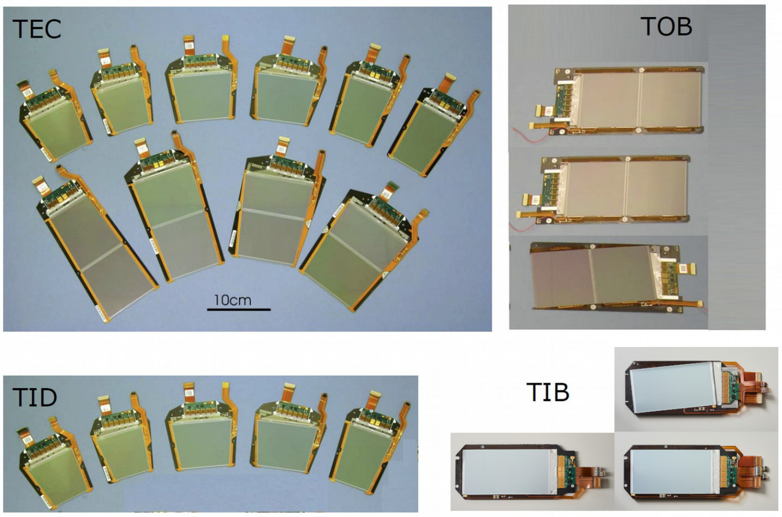

Figure 4. Module types of the SST.

The APV25 chip is used to read out groups of 128 strips. In the name, APV stands for "analog pipeline voltage" in the memory pipeline, and the "25" in the name refers to the 250 nm processing technology. For each event, information from all strips is collected and stored on the chip in an analog pipelined memory for potential readout. A functional schematic of a single APV25 chip readout

Table 1. Summary of number of APV25 chips per module and strip pitch (strip pitch range) for barrel (endcap) sensor geometries.

Sub-detector	Layer	No. of APV25s	Pitch [μm]
TIB	1, 2	6	80
TIB	3, 4	4	120
TOB	1–4	4	183
TOB	5, 6	6	122

Sub-detector	Ring	No. of APV25s	Pitch range [μm]
TID	1	6	80.5–119
TEC	1	6	81–112
TID/TEC	2	6	113–143
TID/TEC	3	4	123–158
TEC	4	4	113–139
TEC	5	6	126–156
TEC	6	4	163–205
TEC	7	4	140–172

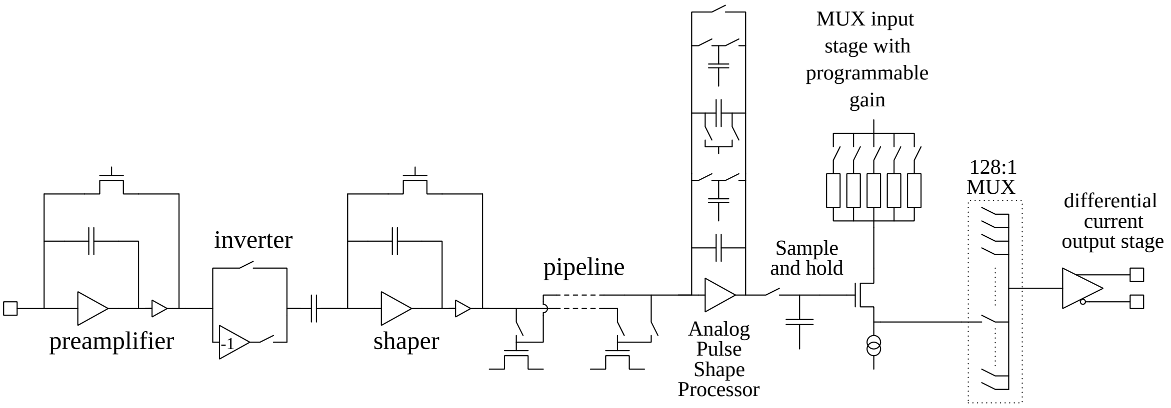

Figure 5. Functional schematic of a single channel of the APV25 chip.

channel is shown in figure 5. The APV25 chip samples at the LHC bunch crossing (BX) frequency of 40 MHz. It has a preamplifier, a unit-gain inverter stage that can be activated or deactivated, a shaper, a 192 BX deep analog memory pipeline, and a deconvolution circuit. The pipeline enables buffering of the information of a given event for a maximum of 4 μs.

The APV25 chip has two principal readout modes, called peak and deconvolution mode. In peak mode, a single cell from the pipeline is read out for a given level-1 trigger accept signal (L1A). In deconvolution mode, an algorithm described in the following is used, as the shaper of the APV25 chip has a shaping time of 50 ns, which is too long to properly distinguish between hits resulting from collisions in consecutive bunch crossings. The deconvolution algorithm [21], implemented in the analog pulse shape processor (APSP) as a switched-capacitor network, effectively shortens the pulse length to approximately 25 ns, thereby reducing substantially the contribution of hits from particles traversing in adjacent (earlier or later) bunch crossings. The algorithm performs a three-sample weighted sum to determine the charge value to be sent out for a particular bunch crossing. The shorter effective peaking time comes at the expense of increased noise, about a factor of 1.5 higher compared with the peak mode. The peak mode is used during special commissioning periods and during runs using cosmic triggers, whereas the deconvolution mode is used for collision data taking. The APV25 chip can reserve pipeline cells for readout of 31 events in peak mode and 10 events in deconvolution mode. A special pipeline emulator board in the underground service cavern close to the central trigger system can block triggers using the CMS trigger throttling system (TTS) to prevent buffer overflow in the chips.

Upon reception of an L1A, the APV25 chip outputs a sequence of analog signals corresponding to the charge present on each strip for the corresponding event, at 20 MHz frequency. An example of an APV25 chip data frame is shown in figure 6. Each APV25 chip first sends a digital header with a start-of-frame marker, the address of the readout pipeline cell and an error bit, followed by the analog strip payload. The payload consists of a series of 128 analog signals with an amplitude proportional to the charge on the individual strips. A digital signal called a tick mark is issued as a synchronization signal and end-of-frame marker. A tick mark is also issued every 70 clock cycles if no L1A is received by the APV25 chip. The signal from two APV25 chips is time-multiplexed at 40 MHz via a dedicated ASIC called the APVMUX (MUX in figure 3). The resulting data frame is then transferred electrically to the AOH, where the electrical signal is transformed to an analog optical signal by the LLD with four selectable gain stages based on InGaAsP edge-emitting laser diodes. The signal from two APV25 chips is sent via a single optical fiber at 40 MHz to one of the back-end readout boards.

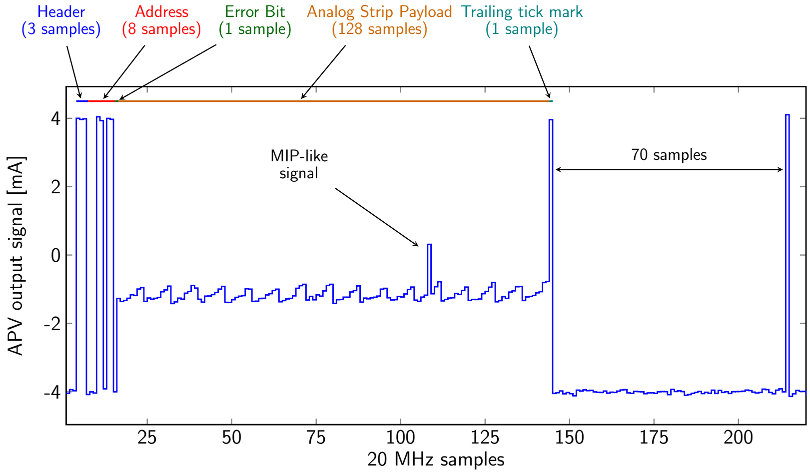

Figure 6. Example of an APV25 chip output signal. A data frame consists of a 3-bit start-of-frame marker, an 8-bit pipeline address, an error bit, the 128 strip analog payload, and the trailing tick mark. In the absence of a level-1 trigger accept signal, the APV25 chip issues tick mark synchronization pulses every 70 clock cycles.

Each detector module contains a Detector Control Unit (DCU) [22] and a phase-locked loop (PLL) [23] chip. The DCU reads the temperature and leakage current of the silicon sensor as well as low voltages (LV) and temperatures on the FEH. The PLL chip can delay the clock and trigger signals sent to the module to perform a precise adjustment of the readout timing in steps of 1.04 ns.

Optical links and back-end readout. The readout signal from the LLD is transmitted via optical fibers out of the underground experimental cavern to the service cavern where it is received by the FEDs. A total of 440 FEDs are used to read out the SST. Twelve readout fibers are bundled into a ribbon, and a total of 8 ribbons are combined into multiribbon cables of 40–60 m length, bridging the path between the caverns. The FED is a 9U VME board with 8 identical inputs; each receives the signals from one ribbon or 12 individual fibers. A FED can thus read the signals from up to 192 APV25 chips; the actual number varies depending on the location of the modules in the detector and other considerations such

2025 JINST 20 P08027

as load balancing. The FED has a 10-bit analog-to-digital converter (ADC) at the input. In normal physics data taking, the FED runs in zero-suppressed (ZS) mode. In this mode it performs pedestal and common mode subtraction as well as cluster finding on the data, before sending the zero-suppressed data to the CMS central data acquisition (DAQ). Candidate hits from charged particle tracks are identified by comparing the strip signal to a corresponding noise level. Dedicated runs outside of the physics data-taking periods are used to determine the pedestal and noise level of each strip. Data from a single strip with a signal above five times its noise level will be transmitted. Additionally, data from a strip whose signal is higher than twice its noise level will be sent out if at least one of its neighbors also has a signal exceeding two times its noise level. Each signal is reduced to 8-bit precision before transmission with the two most significant bits dropped. The highest two ADC values have a special role: 254 implies a digitized strip signal between 254 and 1022 counts, and 255 indicates that the actual value was 1023 counts, i.e., saturating the ADC. The FED can also send unsuppressed (NZS for “no zero suppression”) data that contain the full information from all connected strips in the SST with 10-bit precision. The event size from the SST is 0.5–1.0 MB in the ZS mode, depending on the occupancy, and about 14 MB in NZS data taking, which is used only in special data-taking periods.

Detector control. The central feature of the SST control system is control rings made of CCUs that are electrically daisy-chained into a ring-like architecture. A DOH serves as the optical entry and exit point for each control ring. The FEC boards form the back-end hardware for the detector control system. These 9U VME boards are equipped with up to 8 mezzanine cards, called mFECs, each of which communicates via a bi-directional optical link with one of the 356 control rings in the SST. The optical signal from the mFEC is received by the DOH and transmitted electrically around the control ring.

Each CCU is connected to 2–12 detector modules and transmits clock and trigger signals to them via dedicated lines. In addition, configuration parameters are sent using the I^2C protocol [24], and slow-control data from the DCUs are read back. Each control ring consists of between 3 and 12 CCUs, and control rings vary in size between about 30 and 60 individual modules. The control ring has a secondary path to allow bypassing individual CCUs in case of failure. A redundant DOH is available in case the primary DOH fails.

Readout partitions. The strip tracker is organized into four readout “partitions”, each of which can be operated independently. This means, for example, that for calibration runs the readout partitions can be triggered independently and different calibration procedures can be performed in parallel. The four readout partitions of the tracker are formed by the TIB and the TID together, the TOB, and each of the two endcaps (TEC±).

Services. The SST silicon sensor modules require 1.25 V and 2.5 V low voltage (LV) to be supplied for the front-end readout electronics, and up to 600 V high voltage (HV) for biasing the silicon strip sensors [25]. These are provided by a set of 962 CAEN A4601 power supply modules (PSM). Each PSM consists of two independent and identical power supply units (PSU). Each PSU has two LV channels that can supply up to 6 A at 1.25 V and 13 A at 2.5 V, as well as two HV channels, each capable of supplying up to 12 mA at 600 V. The SST was operated at a nominal HV of 300 V. Between 2 and 12 modules are supplied with LV and HV by a single PSU. Such a set of modules is called a “power group”. The control rings are supplied with 2.5 V LV by 110 CAEN 4602 power supply modules, which can power four control rings each. The power supplies are located in the experimental cavern and are distributed among 29 racks. They are controlled by 29 branch controllers, which are housed inside 8 CAEN 2527 mainframes. The total power consumption at the end of Run 2 was about 32 kW consumed in the front-end electronics and about 60 kW delivered. The difference is dissipated along the 40–60 m long power cables.

The SST is cooled by two cooling plants that circulate liquid C_6F_{14}. Each plant feeds 90 independent sets of cooling loops. The total cooling capacity is about 90 kW, which is sufficient to remove the heat produced by the readout electronics and to keep the silicon sensors at subzero temperatures over the entire lifetime of the detector. The tracker support tube contains a thermal screen system, which includes heating foils and cooling plates. Toward the outside, the heating foils maintain a temperature of $+18^{\circ}$C to avoid possible condensation and to prevent any thermal effect on the CMS electromagnetic calorimeter. The cooling plates in the tracker support tube are fed by two independent cooling plants with 8 loops each. These plants also circulate liquid C_6F_{14}. The thermal screen cooling prevents heating of the tracker from the outside and can be used as backup cooling when the SST is powered off, independently of the two main cooling plants, to ensure that the tracker volume can be kept cold at all times.

3 Detector status

The SST was installed in CMS in December 2007, and, after commissioning, 98.6% of the channels were fully operational [9]. Over time, a number of failures developed; the most significant are described below, representing the status of the end of the running year 2018.

A total of 3 out of the 356 control rings can no longer be operated. This amounts to an inactive channel fraction of 0.7%. There is one inactive control ring in TIB layer 1, one in TIB layer 2, and one in TOB layer 4. The detector regions corresponding to the defective control rings do not overlap in η or ϕ. A total of 6 out of the 1924 power groups are inoperable and the corresponding modules are excluded from data taking. Six out of the 3848 HV channels cannot be put under bias because of short circuits or excessive currents, and again all modules connected are excluded from data taking. The above failures sum up to about 1.1% of the modules in the SST.

In late 2009 the cooling circuits connected to one tracker cooling plant suffered from an overpressure incident. Both the supply and the return valve of the 90 cooling loops were closed while the coolant was still at $+4^{\circ}$C. The coolant gradually warmed up to room temperature and the thermal expansion led to high pressure inside the cooling lines. A few lines developed leaks in the process and a total of 5 of the 180 cooling loops were inoperable by the end of Run 2: three in TIB layer 3, one in TID− disk 2, and one in TOB layer 3. The modules on these cooling pipes continue to be operated but are cooled only from the neighboring detector parts via the carbon fiber structure. As a result of the over-pressure incident, some TIB cooling pipes, which have an oval cross section to fit within space constraints, were deformed and came into contact with the back side of the silicon sensor, creating a short circuit on the HV line rendering all modules connected to the same HV line unusable for data taking. These modules are mostly located in TIB layers 3 or 4, and some are related to the faulty HV channels mentioned above. For some other modules the cooling contact between the cooling line and the module has been partially or fully detached leaving the modules with insufficient cooling. These modules are mostly located in TIB layer 1 or 2. They continue to be operable, but show high temperatures compared with properly cooled detector parts. Layers and rings with stereo modules in addition generally show elevated temperatures compared to single-sided ones. This information is summarized in figure 7, which shows a tracker map where each silicon module is represented by a rectangle in the barrel region and a trapezoid in the endcap region, and one part of a stereo module constitutes one half of this area. The large purple regions in TIB layer 2 and TEC− disk 8 are detector parts that are functional in the data acquisition, but where the readout of slow control data via the DCUs fails. Owing to the multiple overlapping layers of the SST, there is no appreciable loss of physics performance from all failures listed above. More details on the total number of active channels during data taking can be found in section 6.2.

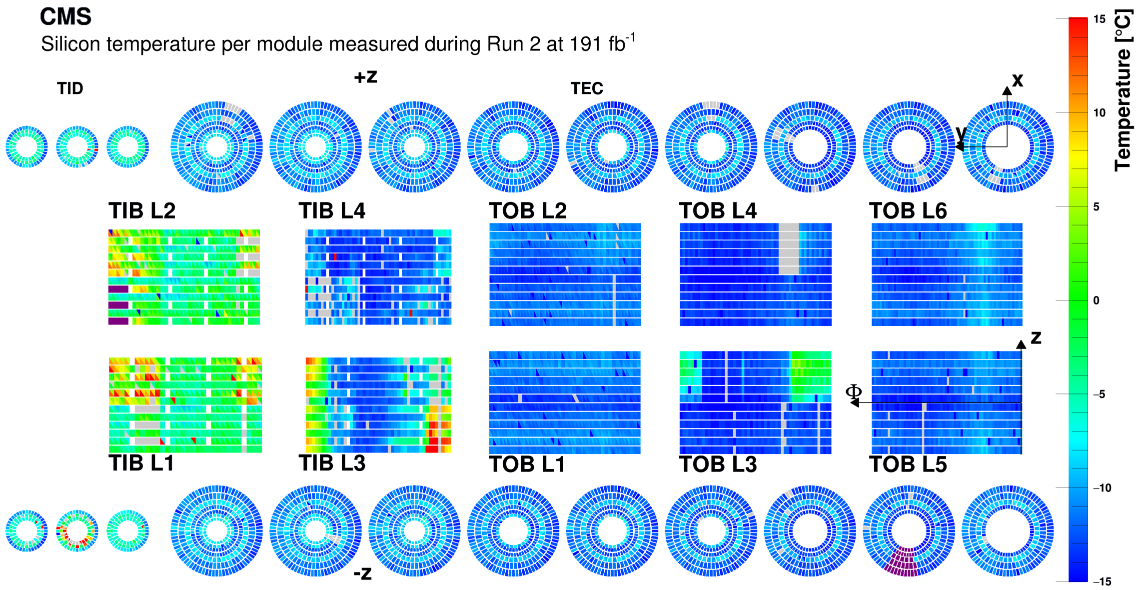

Figure 7. Tracker map where each silicon module is represented by a rectangle in the barrel and a trapezoid in the endcap; in stereo modules each submodule constitutes one half of this area. In the TID and TEC the disks are shown with the distance from the interaction point increasing from left to right. The color scale represents the silicon sensor temperature measured by DCUs after 191 fb^{-1} of integrated luminosity at a cooling plant set point of −20°C. Modules in gray are excluded from the data acquisition. The large gray regions in TIB layers 1, 2 and TOB layer 4 are nonfunctioning control rings. The large purple regions in TIB layer 2 and TEC− disk 8 are detector parts that are functional in the data acquisition, but have problems in the readout of slow control data via the DCUs.

The SST was operated at +4°C coolant temperature during Run 1. The reason to choose a temperature set point much higher than foreseen was insufficient humidity control in the tracker service channels and in the interface region between the SST volume and the environmental seal towards the outside (called the bulkhead). The SST volume itself had very low humidity values at all times with dew points well below −30°C. In LS1 a number of measures were undertaken to enable operation at low temperature. A dry gas delivery system with much larger capacity and fine-grained distribution was installed, and vapor insulation was improved with seamless sealing from the edge of the solenoid magnet to the bulkhead. To avoid condensation on the surface of the cooling ducts and the outside of the tracker cold volume, additional heating elements were added. Monitoring of humidity was also improved by installing a fine-grained system with both in situ humidity sensors and a gas extraction system with remote humidity measurements.

The cooling system also underwent a major refurbishment including new and improved heat exchangers with better regulation and instrumentation, and new housings with better insulation for the plant core. The tracker now has the ability to operate safely with coolant temperature as low as −25°C until LS3 — the foreseen end of life for the SST — when the highest power demand is expected because of accumulated radiation damage. The evolution of the cooling plant temperature set points is summarized in table 2.

Table 2. Cooling plant set points of the SST during different operating periods and integrated luminosity acquired during each period.

Operating period	Cooling set point [°C]	$\mathcal{L}_{\text{int}}$ [fb^{-1}]
2009–2012	+4	29.4
2015–2017	−15	95.0
2018	−20	67.9

The coolant temperature is of great importance because of the temperature dependence of the effects of radiation damage to the silicon sensors (section 7). Charged and neutral particles crossing the detector will cause damage to the silicon lattice structure that results in the introduction of additional energy levels in the silicon bandgap and resulting changes in the macroscopic sensor properties. The most relevant changes for the SST are an increase in the dark or leakage current of the silicon diodes and a change in the full depletion voltage due to a change in the effective doping concentration of the silicon bulk material. At temperatures above about 0°C, defects in the silicon lattice will undergo slow migration processes that result in a reconfiguration of the defects. This migration of defects is commonly referred to as "annealing". For the leakage current, annealing results in a reduction of the additional leakage current caused by irradiation. For the full depletion voltage a short-term (days to a few weeks) process called "beneficial annealing" causes a reversal of the effective doping concentration change. This effect then saturates and at longer timescales (weeks to months and beyond) a process called "reverse annealing" becomes dominant, which results in a further degradation of the sensor material, on top of the initial damage caused by irradiation. The annealing typically occurs over periods without irradiation, but it will also occur while radiation damage is being incurred, provided temperatures are sufficiently high.

4 Detector commissioning and calibration

The procedures for commissioning the SST are described in detail in refs. [9, 26]. The most important aspects of the procedures are reviewed below, and the results of commissioning at different temperatures are shown and compared with expectations and with previous results where available.

An initial step, which only needs to be performed once, is to validate the connection scheme between on- and off-detector components. For this, a unique pattern of high and low signals is generated by each laser driver. This is received by the FED and allows unique identification of the individual connections.

Next, the following calibrations are performed to ensure the optimal performance of the SST:

- internal time alignment,
- tuning of laser driver gain and bias,

- adjustment of FED frame-finding thresholds,
- tuning of the APV25 chip baseline,
- calibration of the APV25 chip pulse shape,
- pedestal and noise measurement, and
- synchronization to external triggers.

Several commissioning steps make use of the periodically issued tick mark of the APV25 chip. A high-resolution time domain picture of two 25 ns wide time-multiplexed tick marks can be seen in figure 8. The tick mark is a digital 1, which corresponds to a +4 mA electrical signal or +400 mV at the input of the AOH. The digital 0 corresponds to a level of −4 mA and −400 mV.

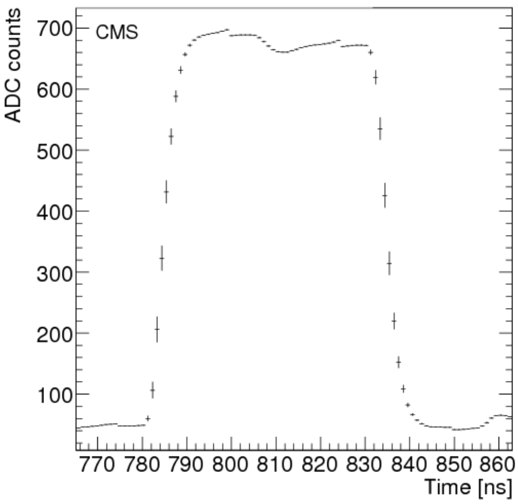

Figure 8. High-resolution time domain capture of the tick marks from two APV25 chips (1 laser) from one module. The signals from the two APV25 chips are time multiplexed. The tick-height corresponds to an amplitude of about 800 mV.

The SST is recalibrated several times per year to compensate for the effects of radiation damage to the readout electronics and the silicon sensors, and to compensate for potential drifts of calibration constants. In addition, changes of the operating temperature, e.g., from −15 to −20°C between 2017 and 2018, necessitate a recalibration.

4.1 Laser driver tuning

Because of the analog nature of the data transmission to the back-end electronics, the LLDs must be tuned in order to match the expected range of charge deposits in the silicon sensors and the 10-bit dynamic range of the FED receivers. This provides more precise charge measurements, leading to improvements in spatial resolution from better determination of charge sharing between strips, and improved particle identification via the specific energy loss ($\mathrm{d}E/\mathrm{d}x$). The LLD has four switchable gain stages to adjust the amplitude of the output signal for differences in the optical link gain, caused

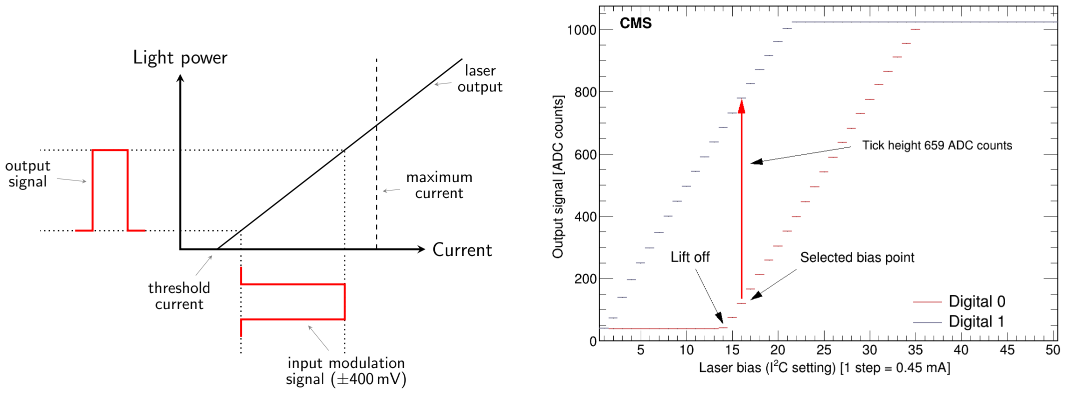

Figure 9. Illustration of pulse modulation by the LLD (left) and visualization of the bias setting scan during the optical link setup run for one LLD gain setting (right).

by, for example, differences in the laser-to-fiber alignment, or by sample variations of the components. Gain setting 0 has the lowest gain and thus proportionally lowest light power output; gain setting 3 has the highest. Figure 9 (left) shows how an input modulation signal is transformed to an output signal with a certain gain when the laser is pre-biased at its working point.

The optical link setup run (called a gain scan or opto scan) consists of a nested loop over the four gain stages of the laser driver and the laser bias setting (0–22.5 mA). For each configuration of laser gain and bias setting scanned in the loop, the signal received by the FED is analyzed when sending a digital 0 and a digital 1 (tick mark), as shown in figure 9 (right). The laser bias is chosen to ensure that the lowest point of the 4 mA differential APV25 chip output (digital 0) still produces a signal within the dynamic range of the FED receiver.

The gain setting is chosen to correspond to the value of the tick mark height closest to 690 ADC counts. The FED receiver has a response of about 1 ADC count/mV, so the tick mark height target corresponds to a link gain of 0.863 V/V when comparing the voltage levels at the LLD input and the FED receiver. This central gain value means that charges of up to 2–3 times that of a minimum-ionizing particle (MIP) are resolved in 8 bits of dynamic range for thin sensors and up to 1.5–2 times a MIP for thick sensors. Larger charge deposits will be flagged using the overflow bits (section 2).

Figure 10 shows the change in distribution of the chosen gain settings when decreasing the cooling plant set point from +4 to −25°C in steps of 4 or 5°C. The gain of the LLD is expected to increase with decreasing temperature by about 0.8% per °C [27]. As a result of this, the number of optical links with lower gain settings increases as temperature decreases. In figure 11 two examples of the resulting height of the tick mark as seen by the FED are shown. The spread of the distributions is about 270 ADC counts (from 552 to 824 ADC counts). The vast majority of the links fall into this range with sharp edges of the distributions on both sides caused by LLDs switching into lower or higher gain settings, if available. Tick heights below about 550 ADC counts correspond to links with malfunctioning components. Such malfunctions can arise from temporary or permanent issues with the programming of the LLDs, from damaged fibers, or from other problems. Links with tick heights near zero are mostly caused by nonfunctioning or (temporarily or permanently) unpowered APV25 chips. Effects of radiation damage on the optical links will be discussed in section 7.

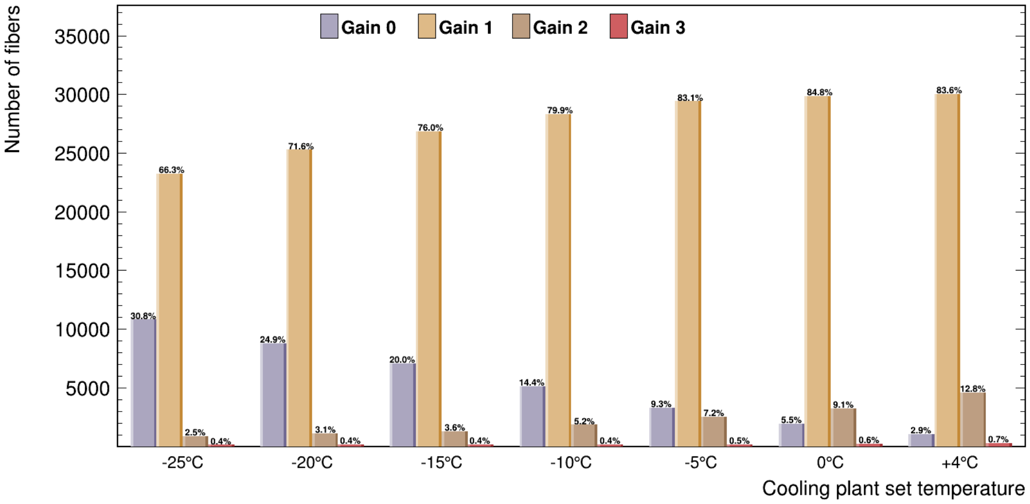

Figure 10. Chosen gain settings at different operating temperatures. The expected migration to lower gain settings with decreasing temperature is seen.

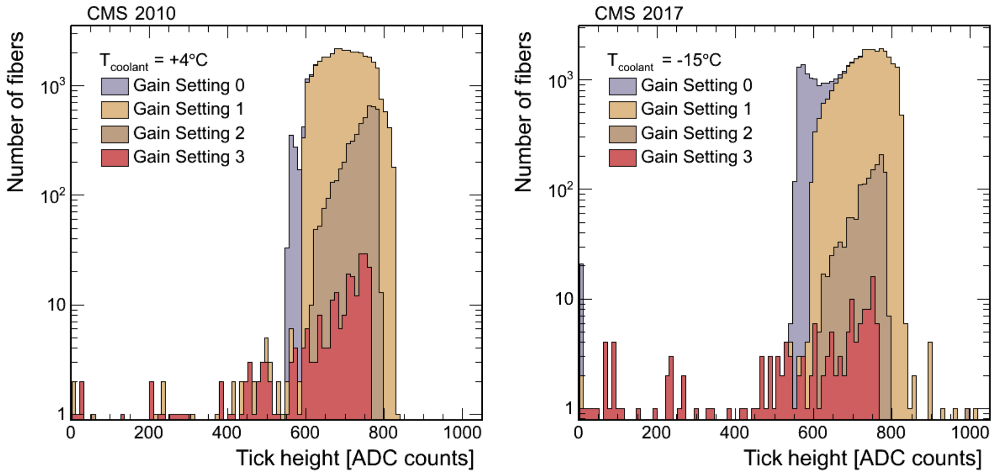

Figure 11. Example distributions of tick heights for each of the four laser driver gain settings for data taken in 2010 at +4°C coolant temperature (left) and in 2017 at −15°C coolant temperature (right). Distributions from different gain settings are stacked.

4.2 Noise measurement

The noise performance of the strip tracker is of crucial importance because the noise is used both in the online zero-suppression of the data in the tracker FEDs and in the offline identification of clusters originating from traversing particles. The noise is measured from runs taken in the NZS readout mode in periods with no beam using low frequency triggers. These are called pedestal runs. The pedestal of a strip is calculated as the mean of the ADC values over several thousand events. All channels of an APV25 chip can experience coherent event-to-event fluctuations or "common mode" shifts. The common mode shift for an APV25 chip in a given event in the analysis of pedestal runs is calculated as the mean of all strip ADC values after pedestal subtraction. The square root of the variance of the resulting quantity over many events is the “common mode subtracted noise” of a given strip. In the event processing inside the FEDs when running with zero-suppression, this common mode value, in this case taken as the median of all strip ADC values after pedestal subtraction, is subtracted from the pedestal-subtracted signal of each strip in the event before cluster finding.

The noise measured with this procedure is the combination of many sources including the silicon sensor, the APV25 chip, the LLD, and the FED receiver. The combined noise from the LLD and the FED receiver (referred to as “link noise”) is measured in gain scan runs from the fluctuations on the link output when the APV25 chip output is biased at −4 mA, i.e., the digital 0. Measurements were performed at operating temperatures between +4 and −20°C and are summarized in figure 12, where the mean link noise is shown for the four different gain stages of the LLD. The noise increases slightly for higher gain settings, as expected, but is quite stable as a function of temperature. Under all conditions the measured link noise is below 1 ADC count, compared with a total noise of 3–8 ADC counts measured during pedestal runs, showing that the link noise is not the dominant noise source.

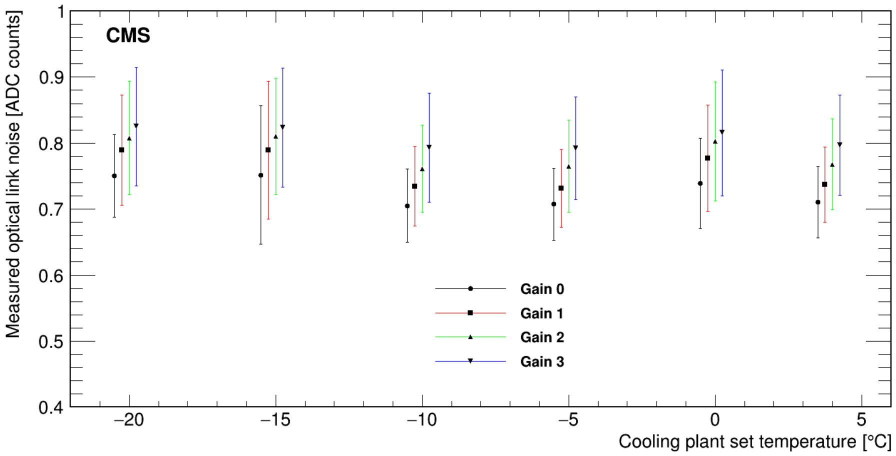

Figure 12. Noise measured in the optical link chain during optical link setup runs at temperatures between +4°C and −20°C coolant temperature for the four laser driver gain settings. The error bars show the root-mean-square (RMS) of the individual noise distributions and are a measure of the spread of the noise among all optical links in the SST. Points for different gain settings at the same temperature are slightly displaced for visibility.

To obtain the noise in units of electrons, the readout gain needs to be taken into account. The tick mark at the input corresponds to a signal of about 8 MIPs or 175 000 electrons in 320 μm of silicon. Using this information, the equivalent noise charge (ENC) in units of the electron charge e is extracted from the noise measurement in ADC counts. The tick mark height is measured in a separate run. Runs used for the tick mark scaling are required to be taken within 48 hours of the corresponding pedestal run and under otherwise identical conditions. APV25 chips with very high (>15 ADC counts) and low (<2 ADC counts) average noise are not used in the analysis. Runs in which more than 100 of the about 72 000 APV25 chips show very high or low noise are rejected completely.

The capacitive noise of a silicon sensor increases with the strip length. As a consequence the total noise is also expected to increase since other noise components do not change for modules with different strip length. An example of this behavior from pedestal and tick mark runs taken at −15°C with the APV25 chips in deconvolution mode is presented in figure 13.

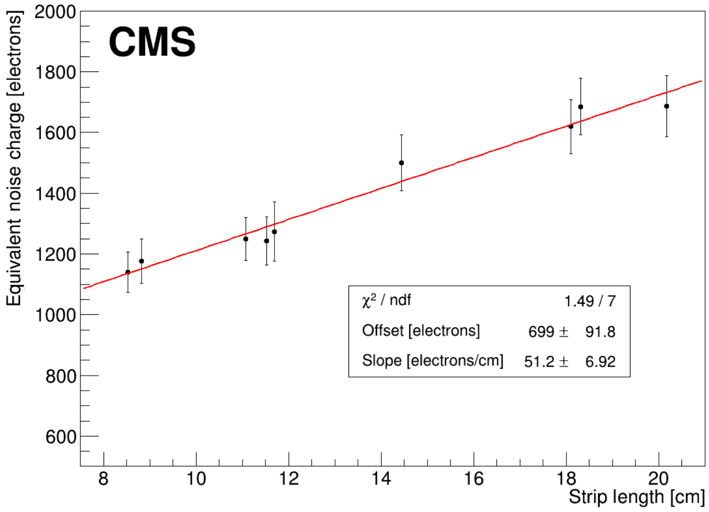

Figure 13. Equivalent noise charge as a function of the strip length.

The expected linear scaling behavior is observed. A straight-line fit to the data yields the following scaling behavior for the equivalent noise charge in deconvolution mode ($\mathrm{ENC}_{\mathrm{deconvolution}}$):

$$\mathrm{ENC}_{\mathrm{deconvolution}} = \mathrm{ENC}_{\mathrm{offset}} + \mathrm{ENC}_{\mathrm{slope}} L = (699 \pm 92)\ e + (51.2 \pm 6.9)\ \frac{e}{\mathrm{cm}}\ L \tag{4.1}$$

where $\mathrm{ENC}_{\mathrm{offset}}$ and $\mathrm{ENC}_{\mathrm{slope}}$ are the offset and slope of the fit, respectively, and L is the strip length in cm. The same analysis is performed for all runs available from Run 2. The fit is only performed if data are available from all readout partitions. The results are summarized in figure 14, where the slopes and offsets are reported as a function of the integrated luminosity, $\mathcal{L}_{\mathrm{int}}$. The offset shows a slight increase with the accumulated integrated luminosity. A linear fit to the data yields

$$\mathrm{ENC}_{\mathrm{offset}}(\mathcal{L}_{\mathrm{int}}) = (677 \pm 26)\ e + (0.6 \pm 0.3)\ \frac{e}{\mathrm{fb}^{-1}}\ \mathcal{L}_{\mathrm{int}}. \tag{4.2}$$

The $\mathrm{ENC}_{\mathrm{slope}}$ is constant as a function of the accumulated integrated luminosity. The central value is

$$\mathrm{ENC}_{\mathrm{slope}} = (49.4 \pm 1.3)\ e/\mathrm{cm}. \tag{4.3}$$

When fitting with a first-order polynomial, the result for the increase with integrated luminosity is compatible with zero. In ref. [1] a compatible scaling behavior was observed at low operating temperatures.

4.3 Time alignment and trigger synchronization

A precise time alignment of the detector readout to the LHC collisions is required to obtain an optimal signal-to-noise ratio, while minimizing the contributions from particles in adjacent bunch crossings. The time alignment of all APV25 chips in the tracker is performed in multiple steps, several of which take place before collision data taking. Initially the known length of the readout fibers from the modules to the back-end electronics is taken into account. After this, the time alignment of the tick marks of the individual APV25 chips is performed. The readout sampling is adjusted to account for

2025 JINST 20 P08027

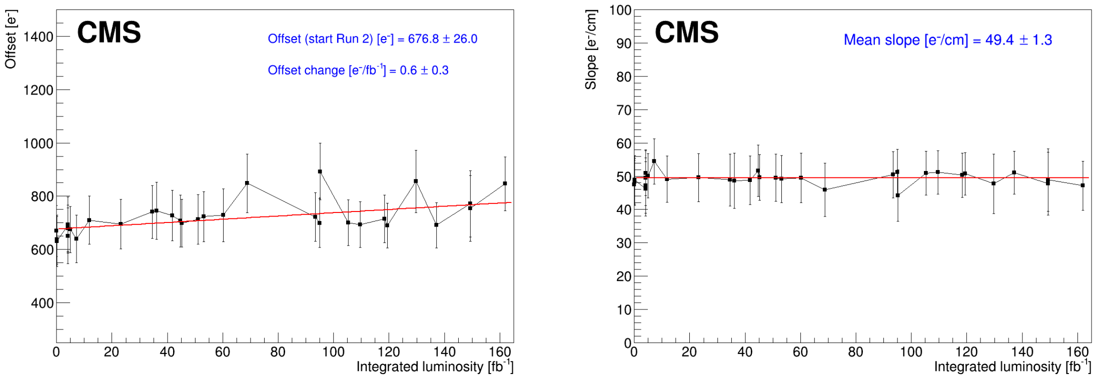

Figure 14. Offsets (left) and slopes (right) as a function of the integrated luminosity, derived from straight-line fits to the equivalent noise charge as a function of the strip length.

the time of flight of the particles through the detector, assuming that these move at the speed of light along straight trajectories starting at the nominal collision point. The required time adjustment ranges from about 1 ns for the central region of the inner barrel to about 9 ns in the outer rings of the last disk of the tracker endcaps. The internal latency of each APV25 chip is adjusted to ensure that, for a given L1A, the information from the appropriate BX is read out from the APV25 chip pipeline buffer. This uses data triggered on cosmic muons, and is done before the start of beam operation [26]. These adjustments already give good time alignment for recording pp collision data. In addition, the time alignment of each module is verified with pp collisions. For each module in the SST, a random time shift in a window of ±10 ns around the current setting is applied, i.e., in a window with the width of about one LHC BX. By shifting only up to a maximum of ±10 ns it is expected that most detector modules are sufficiently close to their original working point to still efficiently detect particle hits. By shifting modules randomly, the likelihood of having inefficient modules in consecutive tracking layers is minimized. A certain number of tracks is collected with these settings. Only tracks with a transverse momentum above 1 GeV are used for the final analysis. The timing of each module is then shifted by +1 ns relative to its current (random) setting. Modules which reach a shift of +10 ns compared with their initial setting are next set to −10 ns relative to the initial timing. This procedure is repeated 21 times to ensure that all modules have taken data with timing settings in the window [−10 ns, +10 ns] with respect to their initial working point in steps of 1 ns. For each of these delay steps, the leading strip charge of clusters associated to reconstructed particle tracks is studied to find the timing point that maximizes this charge. Simulations show that maximizing the entire cluster charge would lead to higher contributions from collisions from adjacent bunch crossings, due to inter-strip cross talk [28]. Modules can be synchronized with a precision of around 1 ns with this method. Most modules require little or no adjustment after the time-of-flight adjustment.

Figure 15 summarizes the adjustments required for each layer and disk of the SST. The endcaps are split according to the thickness of the sensors. Figure 15 (left) shows the net delay required on average in each layer; figure 15 (right) shows the delay curves in which the signal decreases when moving away from the optimal working point. Each data distribution is fit with a Gaussian function, which approximates the pulse shape of the APV25 chip in deconvolution mode well in the central part of the distribution.

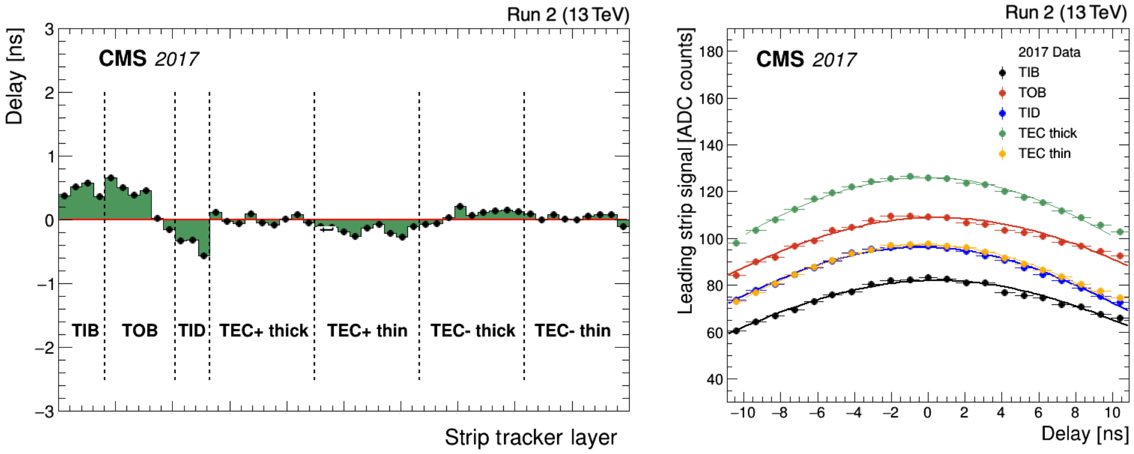

Figure 15. Left: average delay adjustment relative to the original sampling point for each layer of the tracker. Right: leading strip charge in a cluster as function of the change in sampling point for different parts of the strip tracker. The data are fit with a Gaussian function to determine the position of the maximum. The smallest possible delay adjustment is 1 ns.

5 Simulation

An accurate simulation is required to design and optimize a detector and to better understand its operation. Ultimately, those simulations are used as a fundamental tool to analyze and interpret the recorded data. The simulation chain starts with the generation of the pp collision products, then propagates the particles inside the CMS detector through the passive components and sensitive elements, and finally models the response of the readout electronics. The reconstruction that follows is identical for data and simulated events.

A dedicated software package [29] based on the Geant4 toolkit [30] has been developed by the CMS Collaboration. Each particle is propagated through the detector volume. The particle entry and exit points are recorded for each sensitive element, together with the energy deposited. The granularity of the information saved matches the design of the detector and its sensitive elements, which are strips in the case of the SST.

To properly reproduce the interactions of the particles, taking into account, e.g., nuclear interactions, photon conversions, and electron bremsstrahlung, an accurate description of the passive and active detector components was prepared following the completion of the construction and integration of the SST in CMS in 2007. Individual components had been weighed during construction, and the results were then compared with the estimated weights of the corresponding components in the simulation. The sum of these weights for each partition and for the entire SST is given in table 3, showing agreement within 5%. The TOB was never a standalone entity so could not be weighed independently.

The SST material budget given in units of radiation length (X_0) and interaction length (λ_0) is shown in figure 16 as a function of η, with different contributions stacked. The sensitive elements contribute only about 9% of the total. The dominant contribution comes from the support structures (≈36%) and services (power cables, cooling pipes). In the barrel-to-endcap transition regions, $1.2 < |\eta| < 1.8$, the material budget reaches 1.8 X_0, due to the routing of the cables and cooling pipes from the inner regions. In the central part of the tracker ($|\eta| < 0.8$) the material budget remains below 0.8 X_0.

Table 3. Simulated and measured weights of the SST and of three of its partitions.

	Measured weight [kg]	Simulated weight [kg]	Difference [%]
SST	3990^{+90}_{-130}	4037	−1
TIB/TID	450^{+20}_{-12}	427	+5
TEC+	704.3	691.7	+1.8
TEC−	700.2	691.7	+1.2

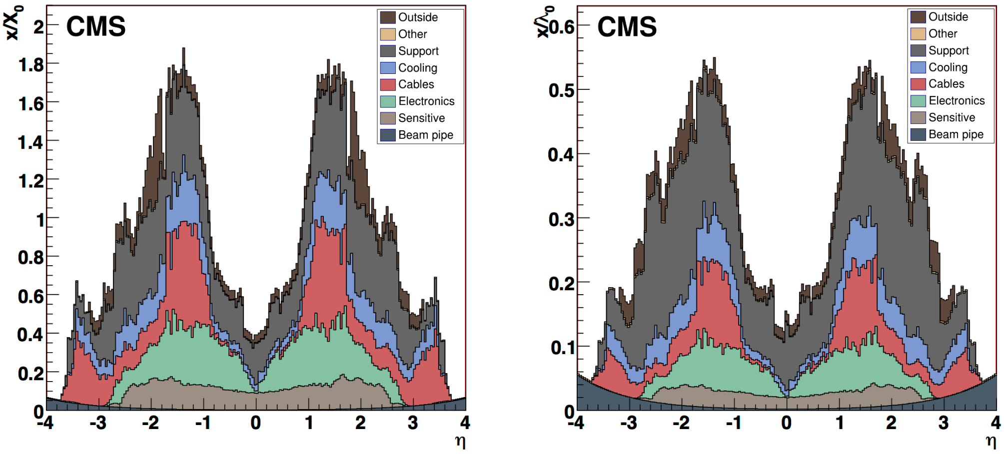

Figure 16. Material budget in units of radiation length (left) and interaction length (right) as a function of η in the SST simulation, shown for the different material categories: beam pipe, silicon sensitive volumes, electronics, cables, cooling pipes and fluid, support mechanics and outside structures (support tube, thermal screen and bulkheads).

After the GEANT4 energy deposition step in the sensitive material described above, the SST simulation proceeds as follows. First, the behavior of charges in the silicon is simulated: the energy deposited by GEANT4 is distributed along the path of the particle in the silicon. Then each individual subdeposit is migrated to the surface of the sensor, taking into account local effects in the silicon sensor, e.g., the drift due to the magnetic and electric fields, together with the effect of thermal diffusion. The result is a charge on the surface, with a position and a width. The charge contributions are merged for each strip. The resulting signal is then processed to include the effects of the electronics and digitization to derive the so-called digis, which are the detector event data as output by the electronics. By design, the digis have the same data format as data from the detector.

The simulation implements the following steps:

- modeling of the signal pulse shape, in peak or deconvolution mode,
- addition of noise (and the pedestal value in NZS readout mode),
- addition of in-time and out-of-time pileup contributions by adding signals from 12 bunches before and 3 after the actual collision bunch, using simulated minimum bias collisions,

- modeling of the time of the signal hits: the time of each simulated hit is shifted taking into account the bunch of its origin, and the shifted time for each hit is considered when generating the pulse shapes. The signals from out-of-time particles are scaled down in size according to the time response of the electronics,
- application of conversion factors (gains) for electronic channels,
- addition of inter-strip cross talk.

In deconvolution mode the signal is processed with an algorithm to reduce its duration to a 25 ns time window. The deconvolution pulse shape is parametrized in the simulation based on the results obtained from ref. [28], with the shape shown in figure 17.

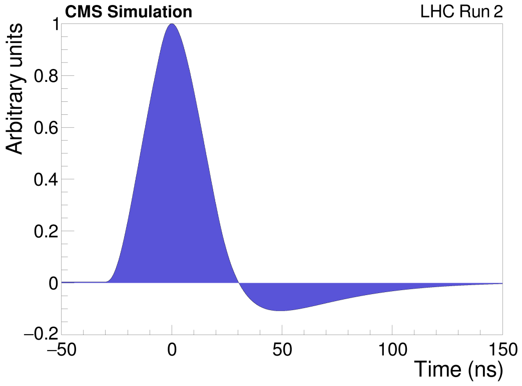

Figure 17. Simulated APV25 pulse shape (deconvolution mode) in the CMS simulation software. The peak is centered at 0, corresponding to a perfect timing alignment with respect to LHC collisions.

Inter-strip cross talk is caused by inter-strip capacitance. The total charge deposited by a particle is visible in three neighboring strips. In 2018, during a planned CMS maintenance with 0 magnetic field, the cross talk was measured in NZS data using cosmic ray muons [31]. Table 4 summarizes the measurements obtained during this dedicated campaign. The majority of the charge (between 75 and 86%) is collected in the leading strip and its two neighbors (6–10%).

One of the main figures of merit for the SST simulation is the comparison between the simulated and measured cluster charge, corresponding to the charge deposited by a particle crossing the sensor. In figure 18 the simulated cluster charge is in sufficient agreement with the measured charge for each SST partition, as can be seen.

Table 4. Cross talk measured in the barrel in 2018, obtained with cosmic ray data taken without magnetic field. Results are summarized as the average fraction f_0 of observed charge for the leading strip, the fraction f_1 on each of the two neighboring strips, and the fraction f_2 on each of the strips next to these neighboring strips.

	f_0	f_1	f_2
TIB Layers 1, 2	0.836 ± 0.009	0.070 ± 0.004	0.012 ± 0.002
TIB Layers 3, 4	0.862 ± 0.008	0.059 ± 0.003	0.010 ± 0.002
TOB Layers 1–4	0.792 ± 0.009	0.083 ± 0.003	0.020 ± 0.002
TOB Layers 5, 6	0.746 ± 0.009	0.100 ± 0.003	0.027 ± 0.002

2025 JINST 20 P08027

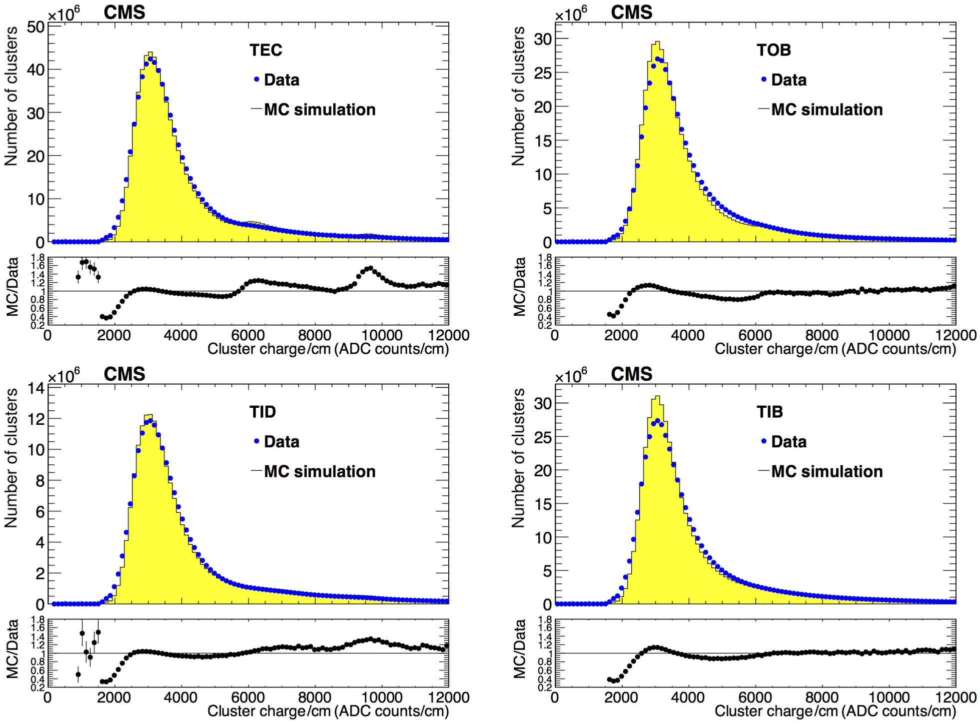

Figure 18. Simulated and measured cluster charge normalized with the track path length for the different SST subdetectors: TEC (upper left), TOB (upper right), TID (lower left), and TIB (lower right). The measurements are shown by points, whereas the simulations are shown by yellow histograms. Lower panels show the ratios of the simulated predictions to data.

6 Detector performance with LHC collisions

In this section, the performance of the SST during LHC collision periods Run 1 (2009–2012) and Run 2 (2015–2018) is presented.

The steps required to reconstruct charged-particle tracks from SST hit data are summarized below. More details are reported in ref. [11]. A good spatial alignment of the detector is a prerequisite for the precise reconstruction of particle tracks. Details about the CMS strategy for the alignment of the SST and the pixel detector are reported in ref. [32].

Cluster finding.

Clusters of strips are reconstructed starting from strips with charges above threshold that are identified by the zero-suppression logic implemented inside the FEDs. Further requirements are imposed for a strip to be included in a cluster. A three-threshold algorithm is used. A strip is considered a seed for a cluster if its charge is larger than three times its noise. The seed strip forms a proto-cluster to which more strips can be added. Strips adjacent to cluster candidates are added to it if their charge is larger than twice their noise. This procedure is repeated until no more strips are found for addition to the cluster. No holes are allowed in a cluster unless a bad strip, as defined in section 6.2, is encountered in which case the search is continued. If a second consecutive bad strip is encountered the search is terminated. A cluster candidate is retained if the summed signal of all strips in the cluster candidate

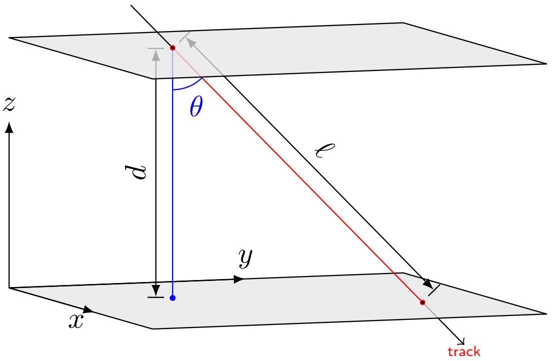

Figure 19. Path length ℓ of a particle crossing a detector of thickness d at an angle θ.

is larger than five times the cluster noise, defined as

$$\sigma_{\text{cluster}} = \sqrt{\sum_{i=1}^{n_{\text{strips}}} \sigma_{\text{i}}^2}, \tag{6.1}$$

where σ_{i} is the noise of an individual strip and the sum runs over all n_{strips} in the cluster candidate.

Path length correction.

For several of the measurements presented in this paper, the cluster charge is corrected for the length ℓ of the particle trajectory inside the active silicon volume (figure 19). The charge of a cluster from a track that passed through the sensor with thickness d at an angle θ with respect to perpendicular incidence on the sensor is scaled as $\cos\theta = d/\ell$ so that $S_{\text{corr}} = S_{\text{raw}} \cos(\theta)$, where S_{raw} is the cluster charge before any correction is applied and S_{corr} is the corrected cluster charge. With this correction cluster charges are normalized to the one expected under vertical incidence.

Cluster signal-to-noise ratio.

A frequently used quantity is the signal-to-noise ratio (*S/N*) of a cluster. In this paper we define this as the corrected cluster charge S_{corr}, defined above, divided by the RMS noise of the individual strips in the cluster. This can be expressed as $S_{\text{corr}}/\left(\sigma_{\text{cluster}}/\sqrt{n_{\text{strips}}}\right)$ with the cluster noise definition from eq. (6.1). The distribution of the energy loss in silicon follows a Landau distribution [33]. An example of the resulting *S/N* distribution from a pp collision run is shown in figure 20. The central part of the distribution is fitted with a Landau convolved with a Gaussian distribution, and the most probable value (MPV) of the Landau distribution is taken as a measure of the *S/N*.

Track finding.

Tracks are reconstructed from hits in the pixel detector and the SST. Multiple iterations of track finding are performed. Early iterations reconstruct prompt tracks originating from the interaction region. Later iterations reconstruct topologies such as displaced tracks. Clusters already associated with high quality particle tracks are not reused in later iterations (excluding regional iterations near high transverse momentum jets or muons). Track seeds are constructed preferentially from hits in the pixel

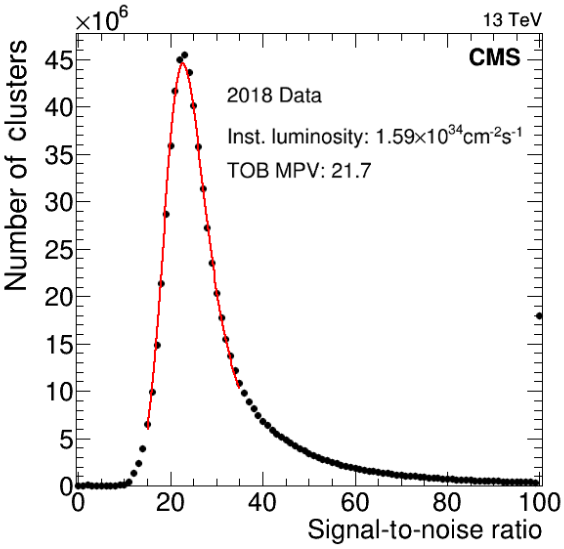

Figure 20. Example of a signal-to-noise distribution from the TOB recorded during 2018 at an instantaneous luminosity of $1.59{\times}10^{34}\,\mathrm{cm}^{-2}\,\mathrm{s}^{-1}$. The central part of the distribution is fitted with a Landau convoluted with a Gaussian distribution. The bin at 100 serves as the overflow bin.

detector (triplets for the original, quadruplets for the upgraded pixel detector). Seeding in subsequent iterations relies on triplets or doublets of pixel hits or a mix of hits in the pixel and innermost layers of the SST, taking into account constraints from the size of the interaction region. Later iterations also use combinations of TOB and TEC layers for track seeding. The final track fit is performed using a Kalman filter algorithm. Clusters associated with a reconstructed track are called on-track clusters.

6.1 Detector occupancy

The mean detector occupancy, defined as the average fraction of detector cells that are traversed by one or more particles per event, is an important quantity to consider when designing detectors, in particular when defining the granularity of the sensors. The SST was designed to ensure the occupancy is at most a few percent. The occupancy depends on the pitch, the strip length, and the particle flux in a given location within the detector. It is measured via the strip occupancy, defined as the ratio between the total number of strips in the reconstructed clusters associated with a particle crossing a sensor and the total number of strips in the detector. Figure 21 shows the average strip occupancy at the beginning of an LHC fill for a mean number of pp interactions of about 55 per bunch crossing, which can be translated into an instantaneous luminosity of $2 \times 10^{34}\,\mathrm{cm}^{-2}\,\mathrm{s}^{-1}$. Even at this high value of pileup, more than twice the design value, the occupancy is at most a few percent, in line with the design values defined in ref. [6].

The lowest occupancy (0.7%) occurs in the last layer of the barrel (TOB) whereas the highest occupancy (5.6%) occurs in the innermost ring of the TID. Readout deadtime due to the FED buffer occupancy, leading to a loss of data-taking efficiency, is expected at a level-1 trigger rate of 100 kHz only for occupancies above 8% [34], a value that is not reached in the SST.

The occupancy is monitored daily, because a deviation from typical values can be a sign of a detector issue, e.g., an increase of the noise, or a localized detector failure.

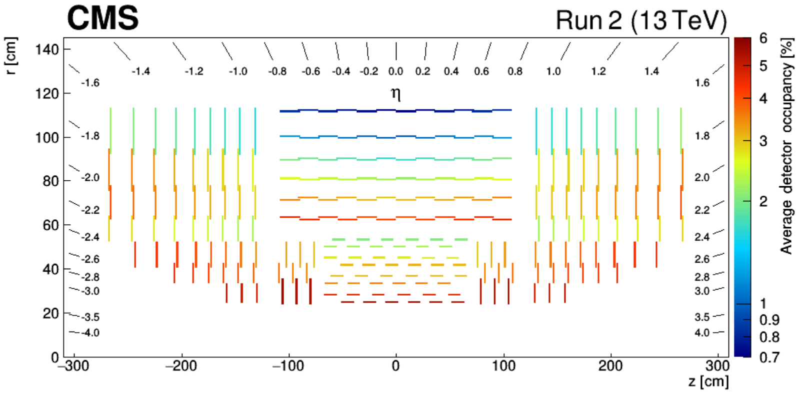

Figure 21. View of the SST mean strip occupancy in the r-z plane recorded at the beginning of a typical LHC fill where the pileup was at its maximum (of the order of 55).

6.2 Bad component identification

Failure of components of the SST can occur for various reasons, ranging from radiation damage to thermal and electrical issues. Although some external failures, e.g., of the power supplies or the cooling plants, can be repaired on a short time scale, interventions within the detector itself are practically impossible. The detector is monitored continuously so that any failures can be rapidly recognized, and if possible, repaired. Likewise miscalibration or other operational issues can be identified and corrected. When noisy or inefficient electronic channels are identified, the information is propagated to the offline data processing so these channels can be removed before reconstructing the tracks. Since the detector has considerable redundancy, the omission of such channels does not degrade the track reconstruction performance in almost all cases.

During data taking, the identification of bad components in the SST is performed automatically in the 48 hours that CMS maintains between data taking and the start of offline reconstruction, during which an express processing of the CMS data is performed. An automatic analysis identifies defects at the level of the APV25 each time 150 000 clusters are reconstructed within the SST during this express processing. During standard LHC operation, this occurs about once per day. An iterative comparison is made between the median occupancy of each APV25 chip and the mean of the medians of all APV25 chips in a given layer and the same z region in the barrel, or in a ring and the same r region in the endcap. At each iteration, APV25 chips with a median occupancy more than 3 standard deviations from the mean of the respective comparison sample of APV25 chips are removed from the next iteration. At the end of this process, all APV25 chips with outlier occupancies are removed from the offline reconstruction. A last iteration targets issues at the level of single strips. For the APV25 chips not identified as problematic in this process, the mean occupancy of each hit strip is estimated assuming a Poisson probability distribution. Single strips for which this probability is too low ($\leq 10^{-7}$) or that are outliers with respect to the mean occupancy in the considered chip are also ignored in the offline reconstruction.

Figure 22 summarizes the channel status for a representative run at the end of 2017. Fully operational modules appear as gray, whereas modules with issues are colored. Disabled modules are also shown in red (these are the permanent defects described in section 3). Broken optical fibers affect a small number of modules (colored green). Modules colored blue suffer from other problems, ranging from a single dead strip to an entire defective APV25 chip.

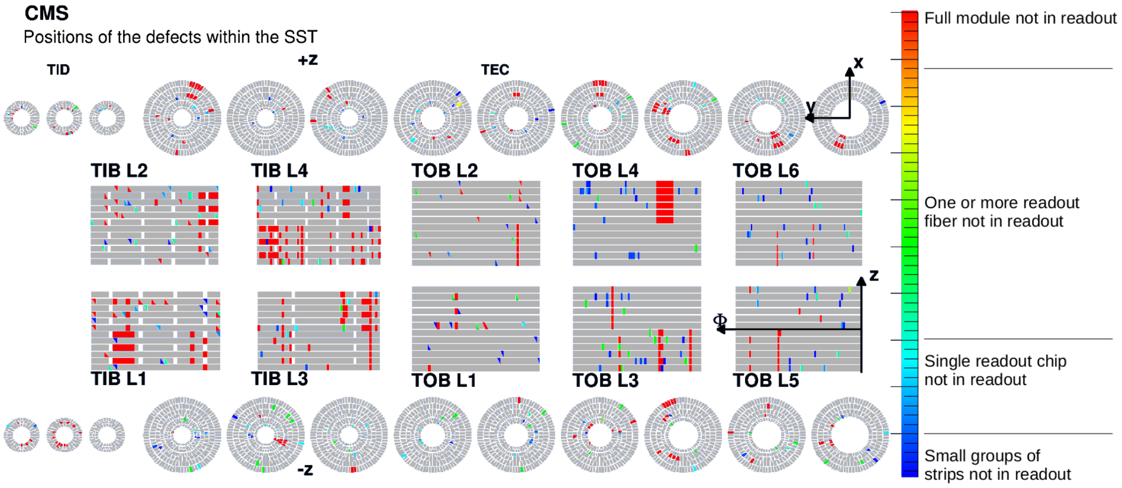

Figure 22. Positions of the defects within the SST at the module level at the end of 2017. Disabled modules are shown in red. Those with at least one fiber not in the readout appear in green. The range blue to green indicates damage varying from single strips (dark blue) to all strips of a single chip. The total number of defects represents less than 5% of the total number of the SST channels.

Table 5. Fraction of live channels in the different readout partitions of the SST at the end of data taking in 2018.

Partition	Percentage of live channels
TIB/TID	91.5 %
TOB	96.7 %
TEC+	96.9 %
TEC−	97.4 %
SST	95.5 %

Overall, the operational fraction of the strip tracker at the end of LHC Run 2 was 95.5%. Table 5 shows the fraction of live channels for each SST partition. As shown in figure 23, the number of defects within the SST remained stable during Run 2 with an average fraction of bad channels just above 4%. The fluctuations visible in the live-channel fraction are mostly due to transient power supply issues or temporary failures of component configuration. Both these causes generally affect only a small part of the detector, and only for relatively short times (typically from a few hours to a few days).

6.3 The APV25 preamplifier saturation

In late 2015 and early 2016 the strip tracker experienced a decrease in signal-to-noise ratio, also associated with a loss of hits on tracks, with the effect becoming more pronounced with increasing instantaneous luminosity. It was eventually found that the problem arose from saturation in the preamplifier of the APV25 chip at high occupancies. The capacitor in the feedback loop (figure 5) is charged by the signal current, and then discharges through a resistance formed by the channel of a field-effect transistor (FET) in parallel with the capacitor, over a time which is long compared with the 25 ns bunch crossing. Although the effect of high hit rates was studied during prototyping, no effects were observed during CMS data taking until the instantaneous luminosity regularly exceeded $3 \times 10^{33}\,\mathrm{cm}^{-2}\,\mathrm{s}^{-1}$., which means more than 20 interactions per bunch crossing.

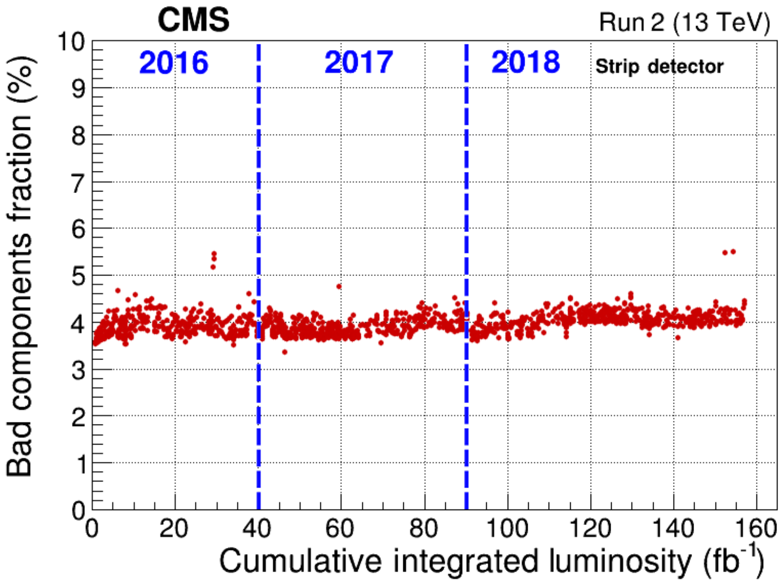

Figure 23. Fraction of bad channels as a function of the delivered LHC integrated luminosity. The vertical lines indicate the start of each calendar year.

In the absence of a build up of charge on the feedback capacitor from previous particle crossings, the response of the preamplifier is linear up to about 3 MIPs but for higher charges the response is no longer linear [13]. The maximum signal size accommodated in the system is ≈ 7 MIPs, limited by the magnitude of the output voltage of the APV25 and the ADC inside the FED, whereas the preamplifier alone maintains good linearity to about 30 MIPs.

The significant reduction of the operating temperature for Run 2 resulted in a large and unexpected increase of the preamplifier discharge time compared to Run 1 when the SST was operated at +4°C. The slow discharge speed together with the high-occupancy conditions resulted in a gradual build up of charge in the preamplifier and consequently a very nonlinear and reduced response of the amplifier to newly deposited charges. Once the problem was understood, it was resolved by adjusting the preamplifier feedback voltage bias (abbreviated as VFP for voltage feedback preamplifier), which controls the feedback FET channel resistance, to reduce the preamplifier discharge time constant (τ).

The simulated behavior of the preamplifier is shown in figure 24. The charge state of the preamplifier is changed (in this case, reduced) by the arrival of a charge from the sensor. The charge then drains away until the original charge state is recovered. One can see that for VFP = 30, the value used in Run 1 and early in Run 2, the discharge time increases strongly with lower temperatures. With VFP = 0 the discharge time is below 1 μs even at low temperature. Given that no adverse effects were seen from this change, the setting was retained at 0, the lowest possible value, for the remainder of Run 2. The effect of the preamplifier saturation in the early 2016 data taking will be discussed in the following sections.

Since the inefficiency cannot be recovered in the data affected by the saturation effects (about 20 fb^{-1}), the effect has to be included in the simulation. A model of the preamplifier saturation was developed, which is applied on top of the detector simulation described in section 5. The charge state of an APV25 preamplifier depends on the specific layer of the SST, on the z position of the detector module within the layer, and on the pileup.

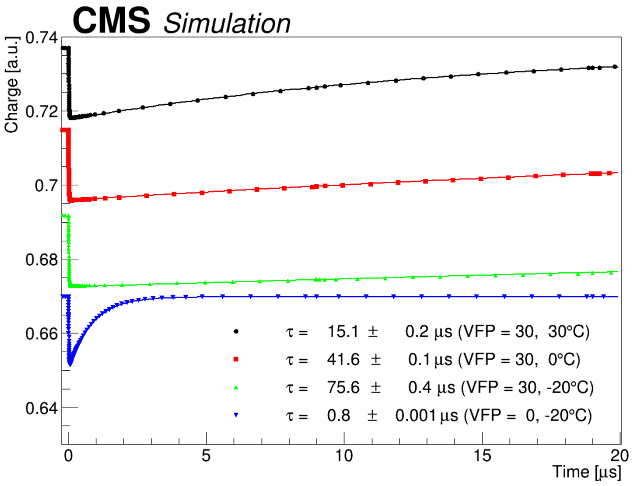

Figure 24. Simulated discharge behavior of the APV25 preamplifier for different temperatures with preamplifier feedback voltage bias (VFP) at 30 (Run 1 and 2015–2016) and at 0 (second half of 2016–2018). An exponential decay function with a discharge time constant τ is fitted to each set of simulated data. The resulting values for τ are displayed in the legend.

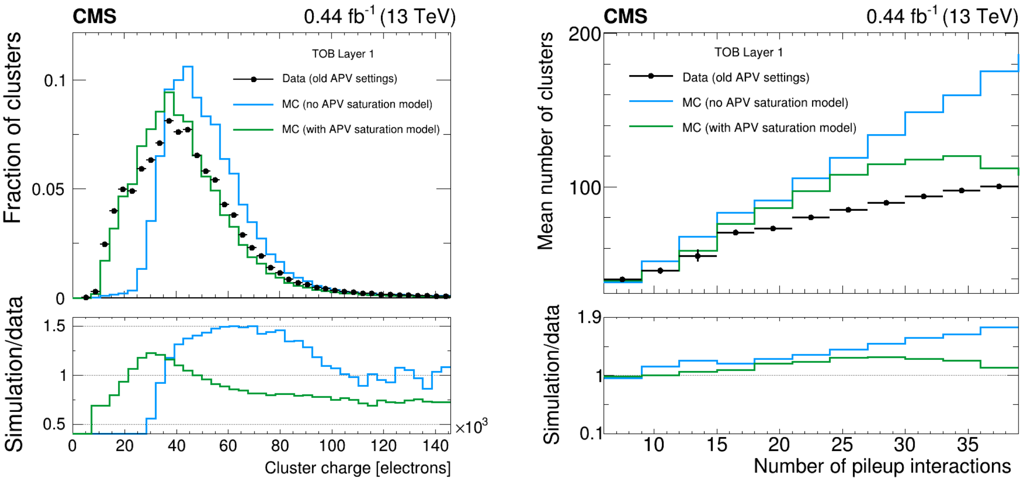

Figure 25. Left: cluster charge distribution for clusters on reconstructed particle tracks in the TOB layer 1. Right: multiplicity of clusters on reconstructed particle tracks in the TOB layer 1 as a function of the number of pileup interactions. The data from early 2016 (black dots) are compared with two different MC simulations; one (blue) does not contain any special treatment of the APV25 preamplifier saturation, the other (green) contains a modeling of the preamplifier saturation to account for the reduced charge response of the amplifier under high-occupancy conditions. Lower panels show the ratio of MC predictions to data.

The effect of applying the model to simulated events can be seen in figure 25. For both the charge of on-track clusters (left) and the multiplicity of clusters as function of pileup (right), the Monte Carlo (MC) events including the APV25 preamplifier saturation describe the data significantly better than without it. The effect on the muon reconstruction efficiency measured using a tag-and-probe method [35] is shown in figure 26 for an inclusive muon track collection [36]. Two sets of data

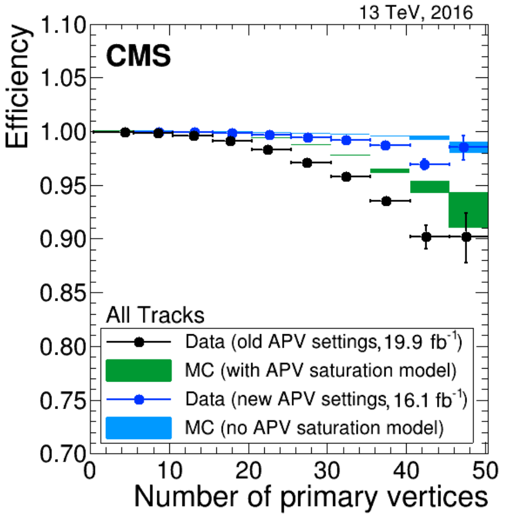

Figure 26. Tracking efficiency estimated using a tag-and-probe method as a function of the number of primary vertices for an inclusive muon track collection [36]. Data from early 2016 (black dots) and late 2016 (blue dots) are compared with two different MC simulations: one (blue) does not contain any special treatment of the APV25 preamplifier saturation, the second (green) contains a modeling of the preamplifier saturation to account for the reduced charge response of the amplifier under high-occupancy conditions.

are shown: data from early 2016 (black) affected by the preamplifier saturation and data from late 2016 (blue) after the VFP parameter change. They are compared with two MC simulations, one containing a modeling of the preamplifier saturation (green) and one without it (blue). The sample with the preamplifier saturation model describes the data from early 2016 significantly better than the sample without this model. Similarly the data after the VFP change are better described by the MC without any preamplifier saturation model, as expected.

6.4 Signal evolution

After the identification and exclusion of nonoperational components, the stability of the signal induced by charged particles in the detector can be studied. The cluster charge per unit path length as a function of the integrated luminosity is shown in figure 27 for 2017 and 2018. Each point in the distribution is a run during an LHC fill with more than 1200 proton bunches colliding in CMS. Only runs for which the data have been certified as good are included [37]. A Landau function is fitted to the cluster signal distribution. The MPV from the fit is plotted, with the error bar being the uncertainty on the MPV from the fit. Large error bars arise from runs with few events. Data from 2016 are excluded because of the APV25 preamplifier saturation described above. The MPV decreases as a function of time with some discontinuities. The overall decrease is caused by the accumulating effects of radiation exposure. The discontinuities occur at recalibrations, particularly of the optical links (section 4.1).

6.5 Signal-to-noise performance

In this section the signal-to-noise performance of the SST is discussed. The *S*/*N* value is very important for the SST, as the FED zero suppression and the offline selection of clusters for the track reconstruction both depend on it.

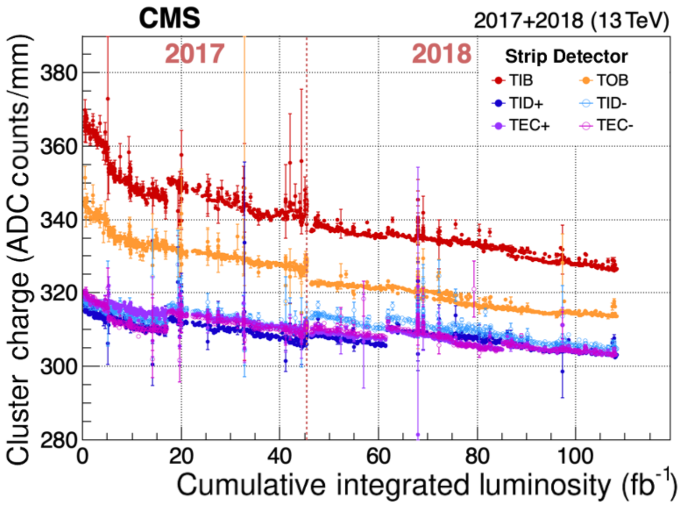

Figure 27. Evolution of the cluster charge normalized to unit length as a function of the integrated luminosity for different parts of the SST. The zero point of the plot is after the integrated luminosities of Run 1 and the years 2015 and 2016 for a total of 75.3 fb^{-1}.

The impact of the APV25 preamplifier saturation in early 2016 on the *S/N* performance of the system is illustrated in figure 28, where the *S/N* for hits on tracks is shown for TOB layer 1, which was the most affected region of the detector. With the old settings, the shape of the *S/N* deviates from the expected Landau-like shape. A downward shift of the MPV and an increased population in the low-end tail of the distribution can be seen. The second run (new APV settings) was taken after the change of the VFP parameter. Under very similar running conditions (peak instantaneous luminosity around $1 \times 10^{34}\,\mathrm{cm}^{-2}\,\mathrm{s}^{-1}$) the *S/N* distribution after the VFP change is completely recovered and shows the expected Landau-like shape, with only a very small population in the low-end tail.

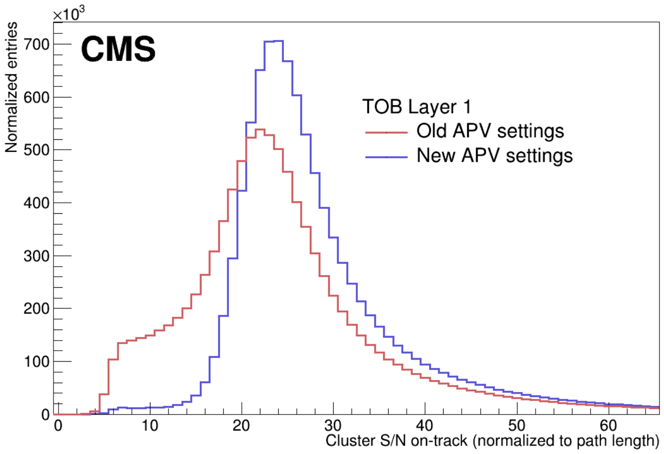

Figure 28. Signal-to-noise ratio for clusters on reconstructed particle tracks in TOB layer 1 for two runs in 2016. The first run (red curve) is affected by saturation effects in the APV25 preamplifier. In the second run (blue curve), the preamplifier voltage feedback (VFP) has been changed to shorten the discharge time of the preamplifier. Both curves are normalized to the same number of entries.

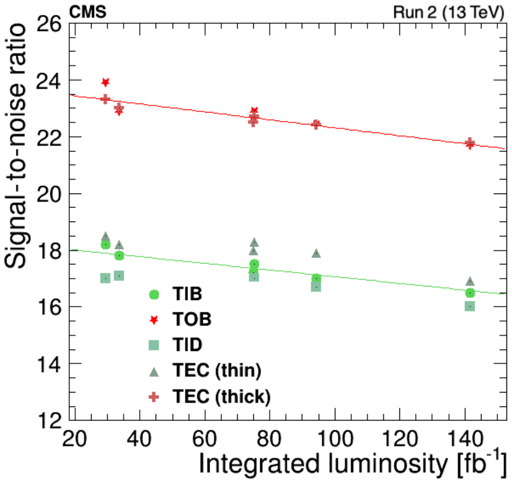

Figure 29. Signal-to-noise ratio as a function of the integrated luminosity for modules from different parts of the tracker. Trend lines are obtained by separately fitting a linear function to the points for thin and thick sensors.

The *S/N* distributions for the different regions of the SST are each fitted with a Landau convoluted with a Gaussian distribution. The MPV of the respective Landau fit curve is quoted as the *S/N* value for a specific detector region. The evolution of the *S/N* as a function of the integrated luminosity is summarized in figure 29. In the TEC the *S/N* is plotted separately for thin and thick sensors. Trend lines are fitted to the two populations of thin and thick sensors. The trend lines show a decrease of 0.12/ fb^{-1} for thin and 0.14/ fb^{-1} for thick sensors. Differences due to the different radial positions beyond the separation of thin and thick sensors are neglected in this plot. Extrapolating both curves to the design end of life of the SST, i.e., to 500 fb^{-1} of integrated luminosity, yields an expected *S/N* of 12.4 for thin and 16.7 for thick sensors, in good agreement with the measurements in ref. [1]. These predictions exceed the detector design specification of an *S/N* value of 10.

6.6 Signal equalization using particles

The energy deposited by a charged particle crossing a sensor in the SST is reconstructed as a cluster of charge signals on individual strips. Residual nonuniformities at the level of 15% in the signal response are expected to come from the LLD even after the signal equalization described in section 4.1. These cannot be corrected by the calibrations performed with the tick height method described in section 4.2. Particle identification using energy loss in the sensors is sensitive to these inhomogeneities. Therefore, signals from MIPs crossing the SST are used to calibrate the detector for uniform response across the full SST as well as for individual modules [38]. This equalization compensates also for the signal loss due to the radiation inasmuch as it is not corrected through the change of LLD gain following an opto scan.

For each APV25, the calibration requires the distribution of the charge normalized to the path length for all clusters associated with MIPs reconstructed in the appropriate silicon module. The MPV is then extracted from a Landau fit to this distribution. The calibration constant (or gain factor G) is determined by normalizing the MPV of the Landau distribution to the same value (300 ADC counts/mm), corresponding to the value expected for a MIP.

As an illustration of the method, the charge normalized to the path length is shown in figure 30, before (left) and after (right) applying the gain factor G to each APV25 of the SST for data recorded during LHC Run 1. The result is a clear alignment of the MPVs over the different regions, corresponding to different positions, sensor thicknesses, and radiation exposures of the modules. When performing the clustering of strips, this gain factor is used as a correction to the strip charge signal in order to guarantee stability and uniformity of the most probable value of the cluster charge over time.

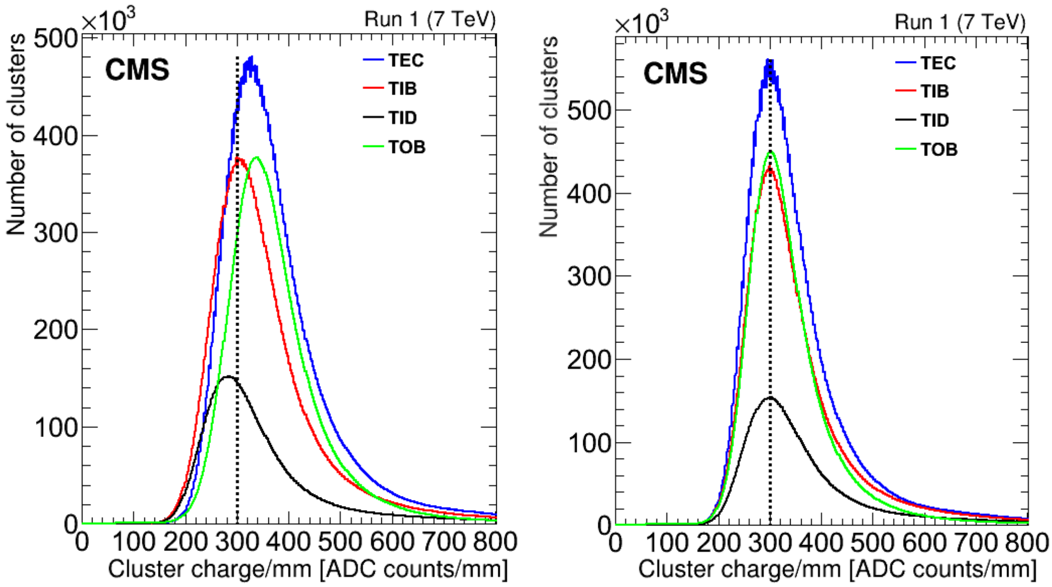

Figure 30. The distribution of the charge normalized to the path length after the tick mark calibration before (left) and after (right) applying the signal equalization. The dashed line represents the calibration value (set to 300 ADC counts/mm).

The cluster charge is monitored over time and is displayed in figure 31 for the different SST parts during LHC Run 2. For daily monitoring of the gain stability, a simpler fitting procedure than that presented in section 6.4 is used over a restricted cluster charge range, which leads to a slightly biased value for the MPV, 310 ADC counts/mm instead of the actual 300 ADC counts/mm set by the calibration procedures just discussed. Despite the bias the overall stability is clear. This bias does not affect monitoring of the stability.

The large fluctuations of the cluster charge in the first 20 fb^{-1} of the data taken in 2016 were caused by the saturation of the preamplifier of the APV25 chip (section 6.3). This effect had a strong instantaneous luminosity dependence and resulted in significant deviation from a Landau distribution, leading to these fluctuations in the calibration. After the APV25 saturation issue was solved in mid 2016, the SST cluster charge remained stable. The discontinuities occur at intended updates of the LLD gain, pedestal, and noise values.

6.7 Lorentz angle measurement

The SST is operated in a homogeneous 3.8 T magnetic field $\vec{B}$ oriented parallel to the beam axis. In the detector modules, the electric field $\vec{E}$ generated by the bias voltage is oriented perpendicular to the sensor plane. In the SST disks the $\vec{E}$ and $\vec{B}$ fields are approximately parallel, whereas in the inner and outer barrels, the electrical and magnetic fields are perpendicular to each other. This causes the charge carriers produced in the n-doped silicon bulk of both the inner and the outer barrel detectors to experience a Lorentz force in addition to their drift to the readout strips under the

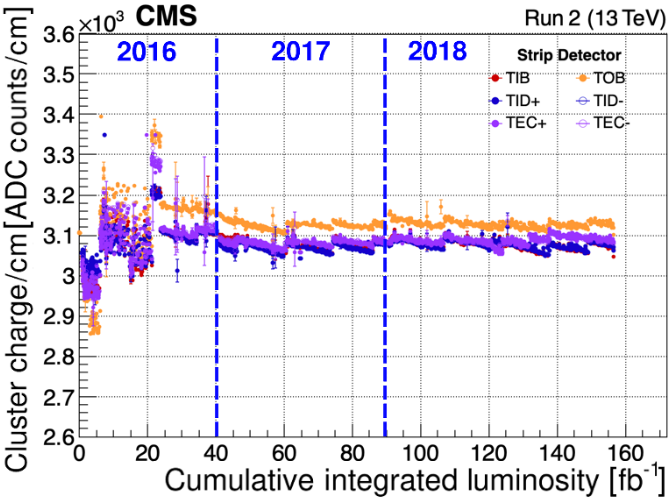

Figure 31. Cluster charge normalized to the path length after the offline calibration for the SST barrel (TIB and TOB) and the plus and minus sides of the TID and TEC as a function of the delivered integrated luminosity. The vertical lines indicate the start of each calendar year. The large fluctuations in 2016 are a consequence of the APV25 saturation issue, see text for details.

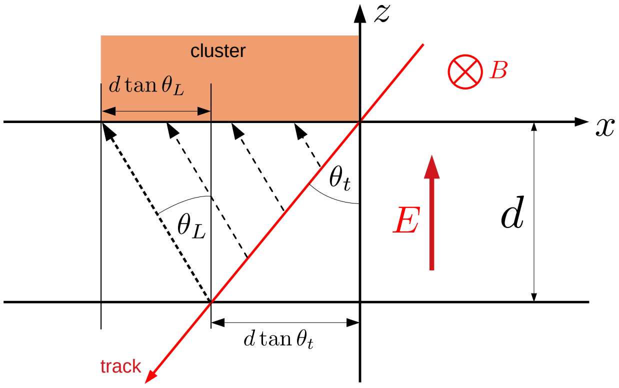

Figure 32. Illustration of the shift due to the Lorentz force along the sensitive coordinate x of a sensor of thickness d. The Lorentz angle is θ_L and the z axis is perpendicular to the sensor. The particle crosses the sensor with an incident angle θ_t. The dashed arrows represent the direction of drift of charge carriers produced in the silicon. The cluster is represented by the orange rectangle. The cluster size $d\tan\theta_\mathrm{t}$ is increased by $d\tan\theta_\mathrm{L}$ in the presence of the magnetic field.

influence of the electric field. As illustrated in figure 32, because of the deflection induced by the Lorentz force, the cluster measured on the sensor surface is distorted in length and displaced. In this sketch, the z axis is perpendicular to the sensor, d is the sensor thickness, and θ_t is the incident angle of the track on the sensor in the projection perpendicular to the strips. The charge carriers inside the sensor are deflected by an angle θ_L, called the Lorentz angle, with respect to the electric field direction. This leads to a shift of the cluster position on the sensor surface measured in the local coordinate x (perpendicular to the strip direction, parallel to the sensor). The size of a cluster ($d\tan\theta_\mathrm{t}$) is increased by $d\tan\theta_\mathrm{L}$ in this direction.

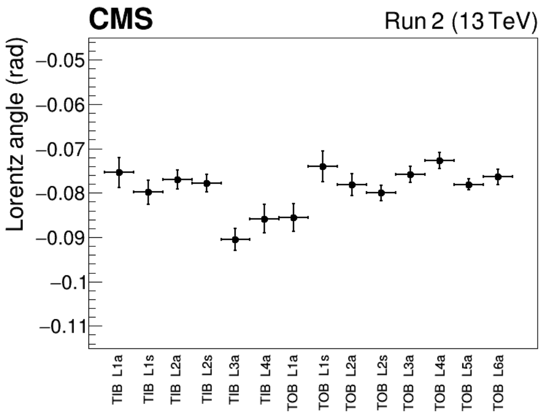

Figure 33. Lorentz angle measured at the end of Run 2 for the different SST layers of the TIB and TOB. The measurement is displayed separately for modules with strips oriented along the z direction, labeled a, and modules with the strips rotated by an angle of 100 mrad with respect to the z direction, labeled s.

To measure the Lorentz angle, the minimum of the distribution of the cluster size as a function of the particle incident angle with respect to the module surface is used [39]. Without a magnetic field, when the Lorentz force and the Lorentz angle are zero, this minimum is observed for perpendicular incidence. With a magnetic field, the minimum occurs when the incident angle is equal to the Lorentz angle, where the charge carrier drift is parallel to the particle trajectory. The results of the Lorentz angle measurement performed at the end of Run 2 for the different layers within the barrel are presented in figure 33.

Once θ_L is known, a correction to the reconstructed cluster position can be applied to derive the actual position on the sensor surface of the charged particle hitting this sensor. This correction is used in the offline reconstruction and as input for the offline tracker alignment procedure [32]. In addition, the Lorentz angle is monitored, because changes could arise from degradation of the sensor performance due to radiation damage. Figure 34 shows measurements of the Lorentz angle for modules with strips oriented along the z direction, belonging to the first layer of the TIB, and for modules with the strips rotated by an angle of 100 mrad with respect to the z direction, belonging to the TOB, as a function of integrated luminosity during Run 2. No significant degradation with accumulated luminosity is observed.

6.8 Hit reconstruction efficiency

6.8.1 Measurement of the hit efficiency

The efficient detection of a hit, defined as the response of the sensor and electronics to the passage of a charged particle, is important in the process of efficiently reconstructing the trajectory of the particle. The hit efficiency is defined as the ratio of detected hits to the number of expected hits belonging to a track. Regular measurements of the hit efficiency are made using collision and cosmic data.

Only high-quality tracks are selected in this analysis. This track selection, defined in ref. [11], is based on a standard set of selection criteria, in particular on the chi-squared normalized to the degrees of freedom and on the compatibility of the tracks with originating from the interaction region. To avoid inactive regions, such as the bonding region for modules with two sensors, trajectories passing near the edges of sensors or close to their readout electronics are excluded from consideration. A module is

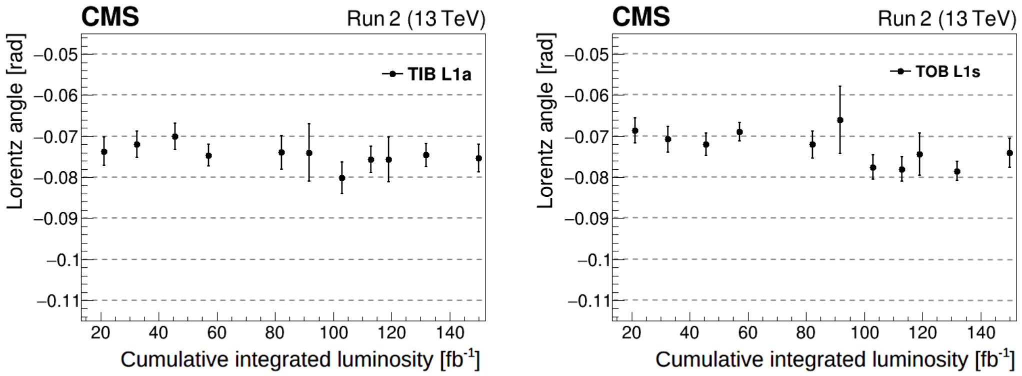

Figure 34. Evolution of the Lorentz angle during Run 2, for modules with strips oriented along the z direction belonging to the first layer of the TIB, L1a (left), and for modules with the strips rotated by an angle of 100 mrad with respect to the z direction belonging to the TOB, L1s (right). The dashed lines are drawn to guide the eye.

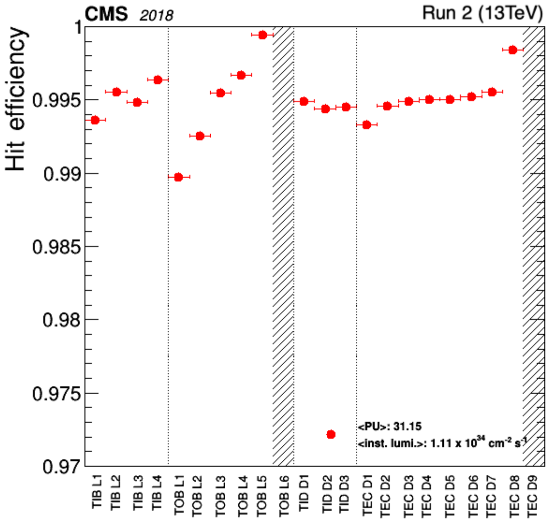

Figure 35. Hit efficiency for the various layers of the SST at the end of Run 2. Known faulty modules are masked. The two gray bands correspond to the outermost layers where the efficiency cannot be measured.

considered as efficient if the distance between the trajectory crossing point and the hit position is less than 15 strips (depending on the sensor type, this corresponds to distances of about 1 to 3 mm).

If the trajectory starts or ends in a module, it is not used for computing the efficiency of this module. Thus, the measurement in the first layer of the inner barrel relies on tracks with inner pixel detector hits, and no measurement is possible in the last layers, i.e., the last layer of the outer barrel and the last disk of the two endcaps. To avoid biases, known bad modules (section 6.2) are excluded from the measurement. Likewise, modules with low efficiency, defined as those with efficiency 10% below the layer average, are not included in the computation of the overall average efficiency. For layers with stereo modules, both sensors are taken into account.

The average hit efficiency at the end of Run 2 is above 99%, as shown in figure 35 for typical beam conditions with an average number of interactions of 31 per bunch-crossing and an instantaneous luminosity of $1.1 \times 10^{34}\,\mathrm{cm}^{-2}\,\mathrm{s}^{-1}$.

6.8.2 Effect of the APV25 preamplifier saturation on the hit efficiency

The effect on the single-hit reconstruction efficiency from the APV25 preamplifier saturation is presented in figure 36, again for modules in TOB layer 1 (as shown also in figure 28). In runs affected by the preamplifier saturation, a notable drop of the efficiency is already seen at luminosities of a few $10^{33}\,\text{cm}^{-2}\,\text{s}^{-1}$, with the effect reaching more than 7% at $1\times10^{34}\,\text{cm}^{-2}\,\text{s}^{-1}$. After the VFP parameter change, only a very slight decrease of the efficiency is observed, even at instantaneous luminosities above the design value of $1\times10^{34}\,\text{cm}^{-2}\,\text{s}^{-1}$.

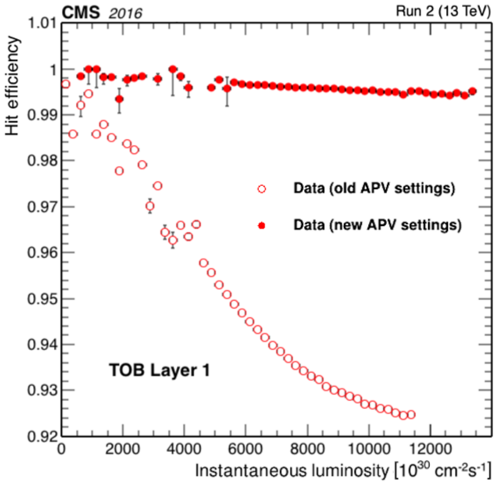

Figure 36. Hit efficiency as a function of the instantaneous luminosity for the modules in the TOB layer 1 for runs before (open circles) and after (filled circles) the change of the APV25 preamplifier discharge speed. Error bars are statistical only.

6.8.3 Highly ionizing particles as the main source of the hit inefficiencies

Although the hit efficiency after eight years of operation is confirmed to remain very high, there is typically a 1% inefficiency, as shown in figure 35. To identify the origin, a measurement of this efficiency as a function of the number of pileup interactions has been carried out. This indicates an almost linear dependency of the hit efficiency on the number of overlapping pp interactions, as shown in figure 37.

Highly ionizing particles (HIPs), generated from nuclear interactions in the SST sensors, give rise to large energy deposits (equivalent to several hundred MIPs) within the silicon sensors. These HIP events, though rare, are the source of a temporary saturation of the APV25 chip, leading to a deadtime of about five bunch crossings during the recovery process. This leads to a loss of efficiency, proportional to the interaction rate.

The effect of HIPs on the APV25 has been studied in ref. [40]. This study was performed during the design of the SST and is summarized in this section.

The HIP events are identified by the presence of a large signal in the affected APV25 chips, whereby the outputs of all other channels connected to the same APV25 are driven down to a level well below their pedestals. To illustrate this behavior, an example of a HIP event identified during a pp collision is shown in figure 38. The typical signature of these events is a large charge deposited in the

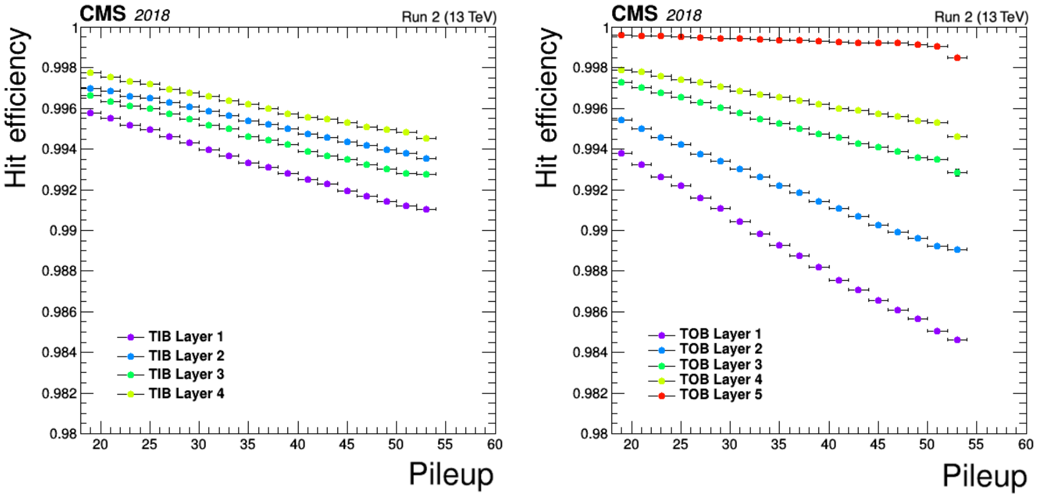

Figure 37. Hit efficiency for different layers in the TIB (left) and TOB (right) as a function of the average pileup multiplicity.

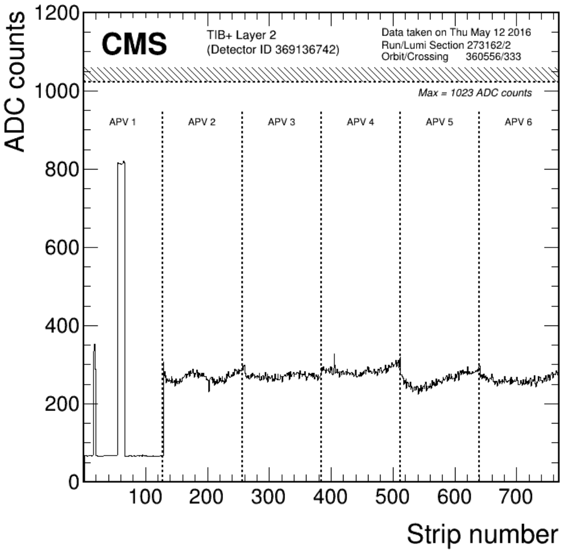

Figure 38. ADC counts of the six APV25 chips in a TIB module during a collision in 2016. The large charge (at ≈ 800 ADC counts located around strip number ≈ 60) together with a drop of the baseline in the first chip is the signature of a HIP event.

sensor, together with a dramatic drop of the baseline of the corresponding APV25, and accompanied by smaller-than-usual channel-to-channel fluctuations of this baseline.

The probability of occurrence of such events within the SST was measured in several special NZS runs in 2018. The selection of the HIP events is based on the typical signature described above. The average probability for a HIP event to occur per pp interaction is shown in figure 39.

A model of the resulting inefficiency was developed, taking into account the HIP probability and the LHC bunch structure with trains of bunches of protons separated by 25 ns. The trains are separated by a gap of 3 μs. The deadtime, during which the chip is assumed to be fully inefficient after the

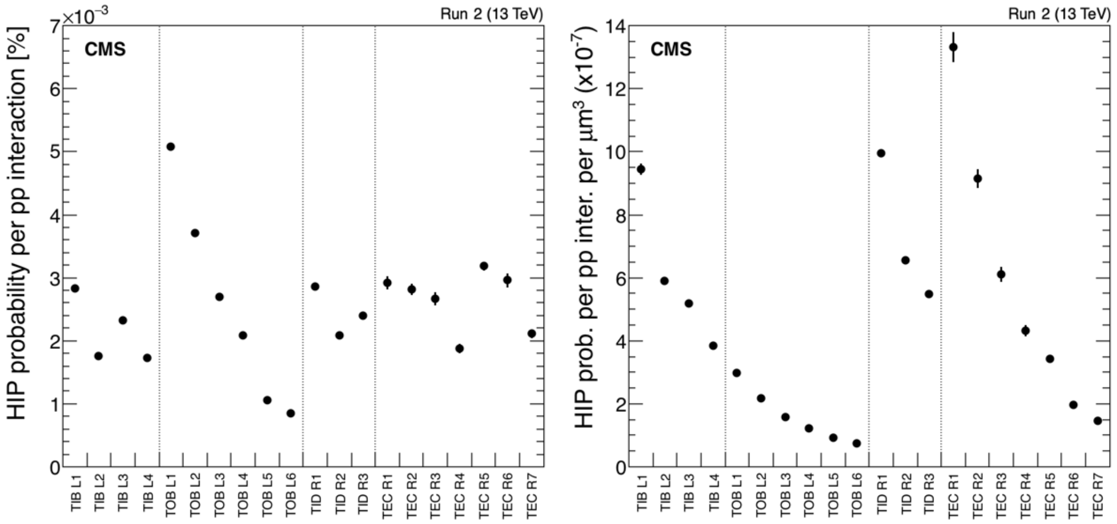

Figure 39. Average probability of HIP event occurrence per pp interaction (left) and normalized to unit volume (right) for all layers of the silicon strip tracker. In the endcaps, the probability is reported per ring.

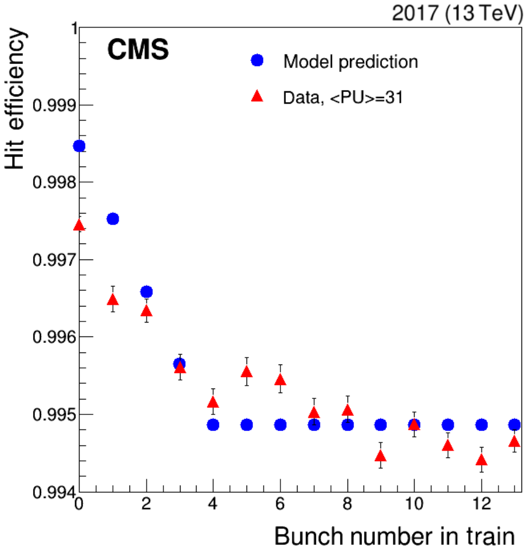

Figure 40. Evolution of the hit efficiency as a function of bunch number within the train for TIB layer 1 modules, obtained from a representative selection of CMS 2017 data with an average pileup of 31. Bunches are separated by 25 ns. The data are represented by red triangles and the model prediction is shown with blue circles.

occurence of a HIP, is used as a parameter. The prediction of this model for the first layer of the TIB is compared with the measured efficiency in figure 40, using data from 2017 with an average pileup of 31, which is representative for the pileup during LHC Run 2. The agreement between this model and the data indicates that the time dependence within a train is well described, that HIP events are the dominant source of the hit inefficiency, and that HIP events lead to a typical deadtime of five bunch crossings, compatible with the measurements from previous dedicated beam tests, as presented in ref. [41].

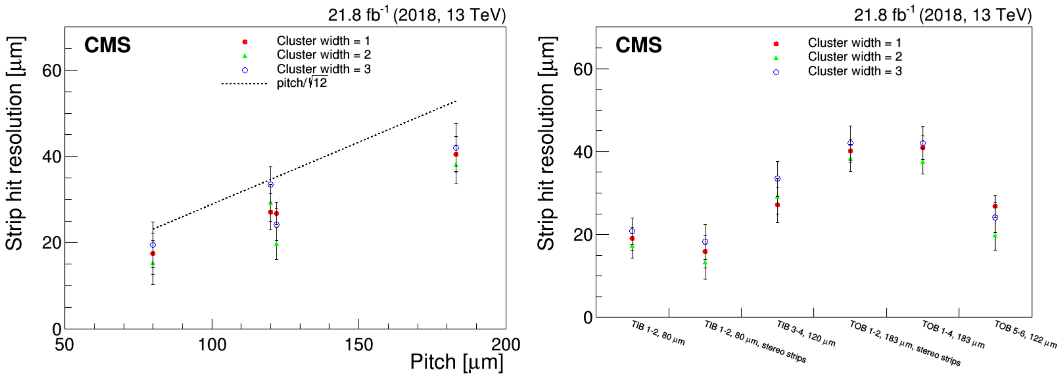

Figure 41. Single-hit resolution as a function of the strip pitch (left) and for different detector regions (right). In the left plot, the expected resolution for binary readout (pitch/$\sqrt{12}$) is also shown for comparison.

6.9 Single-hit resolution

The procedure to measure the spatial resolution of hits within the SST is explained in ref. [42], which also documents the measurements performed during LHC Run 1. The single-hit resolution measured during LHC Run 2 is presented in this section.

In the SST, silicon sensors slightly overlap with their neighbors to ensure a hermetic tracking coverage within the entire η range, so that a particle can cross two sensors in the same layer. To compute the hit resolution, hits from tracks passing through regions where modules overlap within a layer are considered. Tracking is redone without the hits in the layer, and the reconstructed track is used to predict the position of the impact point in each of the two overlapping modules A and B of the layer. For each module, the residual, i.e., the difference between the measured and predicted hit position, is determined. Then the so-called double-difference is calculated as:

$$(\text{hit}_A - \text{prediction}_A) - (\text{hit}_B - \text{prediction}_B), \tag{6.2}$$

where $\text{hit}_{A,B}$ refers to the position of a hit in module A or B, and $\text{prediction}_{A,B}$ refers to the position of a predicted impact point of the track in module A or B.

The advantage of this method is that most uncertainties in the track propagation are cancelled in the difference $\text{prediction}_A - \text{prediction}_B$. For a perfectly aligned detector, the difference of residuals is expected to be zero on average. The width of this difference is a measure of the SST hit resolution, which depends on the thickness, the orientation, and the pitch of the sensor as well as the size of the clusters.

The SST hit resolution measurements performed during the last year of Run 2 are shown in figure 41 41 functions of these parameters. In a detector without analog charge measurement, the typical resolution is limited to $p/\sqrt{12}$ where p is the strip pitch. This binary resolution limit is displayed in the figure, highlighting the improvement achieved through the measurement of the charge sharing, which is made possible by the analog readout of the charge from each channel. By measuring the fraction of charge collected by adjacent strips, the hit position can be interpolated more precisely, leading to a resolution significantly better than the binary limit.

With typical values between 20 and 40 μm, the SST hit resolution matches the expectation from the detector design [43], without any sign of degradation compared to previous measurements [42].

6.10 Particle identification by ionization energy loss

Although the primary function of the strip tracker is to provide precise hit information for track reconstruction, and hence precise momentum determination, the wide linear range of the analog output also provides a measurement of the ionizing energy loss of the incident particles, which can be used for particle identification.

The mean ionization energy loss per unit length $\mathrm{d}E/\mathrm{d}x$ of a particle crossing a layer of material is given by the Bethe-Bloch formula [33]. In a restricted range of momentum p of the incident particle of mass m ($0.2 < \beta\gamma < 0.9$, where β is the velocity and γ the Lorentz factor), the Bethe-Bloch formula can be linearized in m^2/p^2 [38], where K and C are constants and can be extracted from a fit of the mean energy loss measurement:

$$\left\langle \frac{\mathrm{d}E}{\mathrm{d}x} \right\rangle = K\frac{m^2}{p^2} + C. \tag{6.3}$$

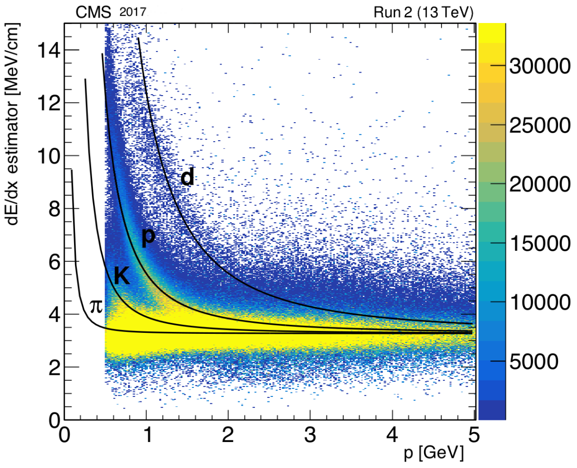

Figure 42. Energy loss measurement in the SST during LHC Run 2. Expected losses for pion, kaon, proton, and deuteron particles are also shown (black lines). Tracks with momentum below 0.5 GeV are not included in this plot.

In the SST, the mean ionization energy loss per unit length is computed by measuring the cluster charge generated in all the sensors along the trajectory of a particle normalized to the path length through each sensor. Because the SST sensors are thin, the fluctuation of the energy loss within a sensor follows a Landau-like distribution. The most probable energy loss is estimated by combining the measurements along the particle trajectory. Several estimators providing the most probable energy loss have been evaluated. The harmonic-2 estimator, which is the harmonic mean of power −2 defined as:

$$I_\mathrm{h} = \left(\frac{1}{N} \sum_{i=1}^{N} (\mathrm{d}E/\mathrm{d}x)_i^{-2} \right)^{-1/2}, \tag{6.4}$$

where N is the number of measurements, is chosen for its stronger discrimination power [38]. The distribution of the most probable energy loss obtained from this estimator as a function of the particle momentum is shown in figure 42. The region corresponding to the energy loss distribution for protons was fitted using the function from eq. (6.3) with K and C as fit parameters. The black lines in figure 42 represent the calculated energy loss for deuterons, kaons, and pions. However, the region for pions at rising energy loss values is not visible due to the cutoff at low momenta. Particle identification using the energy loss measurement within the SST is used in searches for long-lived charged particles in pp collisions [44].

7 Radiation effects

Because of the continuous exposure to particles arising from the high-energy pp collisions of the LHC, the detector modules of the SST and their individual components are exposed to large levels of radiation over their lifetime. The effect of the heavy ion data-taking periods can be neglected because of the very low integrated luminosity. Since the start of collision data taking, two effects have been regularly monitored: radiation damage to the optical link system and radiation damage to the silicon sensors of the SST modules. In both cases the dominant damage mechanism is displacement damage in the crystal lattice through hadronic interactions. The damage mechanism is commonly expressed through the NIEL (non ionizing energy loss) concept [45] in which radiation damage from different particle types is scaled to the equivalent damage from neutrons. As a result, fluences for silicon sensors are expressed in units of 1 MeV neutron equivalent per cm^2 (1 MeV $n_{\mathrm{eq}}/\mathrm{cm}^2$). For radiation damage in the InGaAsP laser diodes in use in the SST, equivalent damage factors for different particle types, that allow scaling to a common reference, is reported in the literature, e.g., in ref. [46].

Simulated fluences in this section are obtained from the FLUKA radiation simulation framework [47, 48], within which the geometry and material distribution of the full CMS experiment have been simulated.

7.1 Optical link radiation damage monitoring

The optical link system is expected to degrade with increasing radiation exposure. The two main radiation-induced effects expected are a decrease in link gain and an increase in laser threshold current. The laser bias setting is retuned during gain scans at regular intervals to account for the change in threshold current (section 4.1). The threshold current is thus measured regularly and its change as a function of time and luminosity can be studied.

The radiation level in the SST varies strongly as a function of the radial distance from the beam line, but has only a weak dependence on the z position. Accordingly results are combined for modules at equal radius in layers (TIB/TOB) and rings (TID/TEC). Measurements of the laser driver thresholds are summarized in figure 43. The threshold current is shown as a function of time to better show annealing effects during periods where no integrated luminosity is accumulated. A reference point in early 2016, to which subsequent runs are compared, is defined for each readout partition. The threshold current change compared with the selected reference point is shown for the TIB and TEC+. Both detector parts show an increase of the threshold current during running periods, and the increase is larger for modules located closer to the beam line. The increase in threshold current closely follows the increase in integrated luminosity. Annealing of the current increase (section 3) is visible in periods with no beam, most prominently during the interruptions of the LHC data taking of 2–3 months, typically starting at the end of a given calendar year, where the SST was kept at room temperature typically for at least a few days. The step in the distribution at the beginning of 2018 corresponds to the reduction of the operating temperature of the SST to −20°C. Such a change

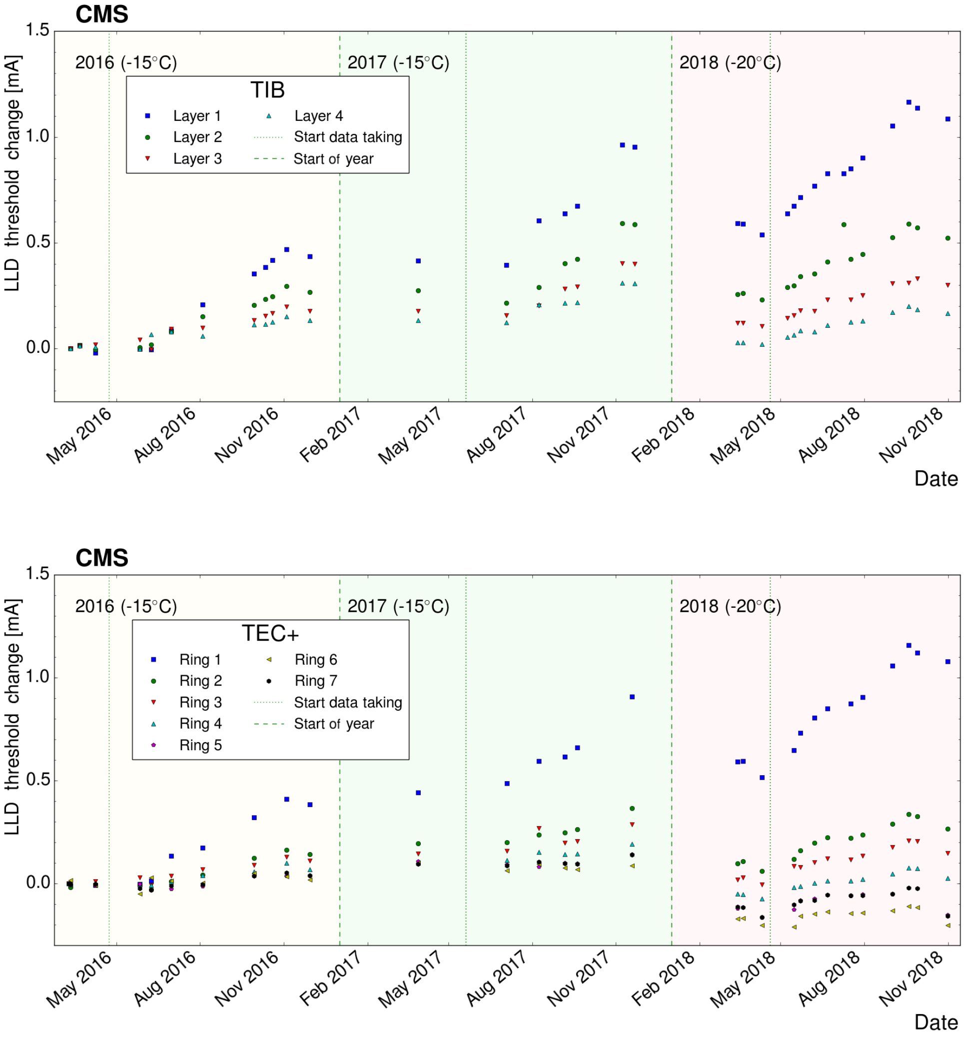

Figure 43. Laser driver threshold increase versus time for laser drivers in TIB (upper) and TEC+ (lower). A point in early 2016, to which subsequent runs are compared, is defined for both readout partitions.

arises from the dependence of the threshold current of the laser on the temperature. The current, for identical radiation exposure and annealing, varies as

$$I_{\mathrm{th}} = I_{\mathrm{th}}(0)\exp\left(\Delta T/T_0\right), \tag{7.1}$$

where $I_{\mathrm{th}}(0)$ is the threshold current at a reference temperature, ΔT is the temperature difference between the laser and the reference value and T_0 is the characteristic temperature of the laser diodes, measured to be around 65 K [49]. The characteristic temperature is used to indicate the temperature sensitivity of the laser diode.

The threshold current increased by 1 mA from the beginning of the 2016 run to the end of the 2017 run (91.4 fb^{-1}) and by 0.75 mA over the 2018 running period (67.9 fb^{-1}), which does not reflect the ratio of luminosities in the two periods. This is believed to be an effect of the different operating temperatures, namely −15°C in 2016–2017 and −20°C in 2018, which reduced the beneficial annealing effect in 2018.

The integrated luminosity over these three years was about 160 fb^{-1}. The absolute threshold current was between 3 and 4 mA in 2016. The maximum possible threshold current is 22.5 mA, which suggests that there should be ample margin for operation up to 500 fb^{-1}, the expected integrated luminosity prior to the HL-LHC upgrades and replacement of the existing system.

From irradiation tests on similar devices [50], a threshold increase of less than 6 mA is expected over the full lifetime of the SST.

7.2 Silicon sensor radiation damage monitoring

The two main effects of radiation on the p-in-n silicon sensors are an increasing leakage current under HV bias, also leading to increased noise, as well as a change of effective bulk doping concentration N_{eff} of the initially n-type bulk, that will eventually cause type inversion to p-type and hence a change of polarity of the bulk material. The depletion voltage decreases before type inversion and increases again afterwards.

Measurements of both the leakage current and the depletion voltage are described below. Both quantities are compared with the predictions from simulations and to preinstallation results. A more detailed discussion of the effects of bulk damage in silicon detectors is reported elsewhere, e.g., in ref. [45].

Simulations of the evolution of the leakage current and depletion voltage have been performed assuming an integrated luminosity of 500 fb^{-1} and a detector operating temperature of −25°C until the start of the LHC LS3.

7.2.1 Leakage current evolution

In radiation-damaged silicon sensors, the leakage current increases linearly with the fluence [45]. This increase is commonly expressed by the “current-related damage rate” or α-parameter, which is defined as the current increase, scaled to +20°C, per sensor volume and 1 MeV $n_{\mathrm{eq}}/\mathrm{cm}^2$. The leakage current increase ΔI_{leak} can then be written as

$$\Delta I_{\mathrm{leak}} = \alpha \Phi_{\mathrm{eq}} V, \tag{7.2}$$

where Φ_{eq} is the particle fluence in units of 1 MeV $n_{\mathrm{eq}}/\mathrm{cm}^2$ and V is the volume of the sensor under consideration. The leakage current of a radiation-damaged sensor is strongly temperature dependent with the leakage current roughly doubling for every 7°C of temperature increase. The leakage current at a reference temperature T_{ref} can be expressed as [45]

$$I_{\mathrm{leak}}(T_{\mathrm{ref}}) = I_{\mathrm{leak}}(T_{\mathrm{sil}}) \left(\frac{T_{\mathrm{ref}}}{T_{\mathrm{sil}}}\right)^2 \exp\left[-\frac{E_{\mathrm{g}}}{2k_{\mathrm{B}}}\left(\frac{1}{T_{\mathrm{ref}}} - \frac{1}{T_{\mathrm{sil}}}\right)\right], \tag{7.3}$$

where E_{g} is the bandgap energy of silicon (1.11 eV), k_{B} is Boltzmann’s constant, and T_{sil} is the temperature of the silicon sensor. The temperature of the sensor depends on the available cooling capacity for the module in question, which here is defined as the increase in temperature due to an increase in power on the sensor. In the SST this is measured using the DCUs on the individual modules during a bias voltage scan. The increase in the total sensor power P, given by $V_{\mathrm{bias}} I_{\mathrm{leak}}$, can be correlated with the increase in sensor temperature to extract the thermal contact coefficient $\mathrm{d}T/\mathrm{d}P$. With sufficient cooling power available, the additional heat generated by the increased current will not result in a (significant) increase in the temperature of the silicon sensor. In regions of the detector without adequate cooling, the increase is sizable and can lead to thermal runaway [51]. Thermal runaway occurs when an increase in leakage current results in additional power dissipation in the sensor which in turn results in a rise in temperature (self-heating) and thus a further increase in leakage current, and this feedback loop continues uncontrollably. Figure 44 shows an example of this in a power group in a stereo layer of the TIB during the 2017 running.

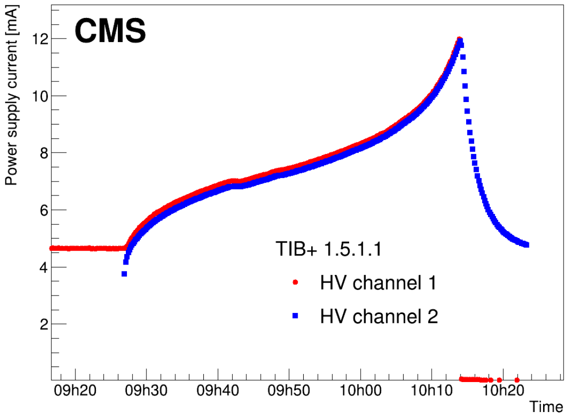

Figure 44. Thermal runaway observed in one power group of the TIB during the 2017 running. A power group consists of two high-voltage channels. The maximum high-voltage current of each channel is 12 mA. Once one of the two channels reaches this limit it is switched off (red dots). The modules connected to the other channel cool down as a result of this and the current decreases (blue squares).

Separate HV channels provide bias to the two sides of each stereo module in this power group. Initially one of the two HV channels is off. Switching on this channel causes the temperature of both sets of modules to increase and the leakage currents increase accordingly. The increase continues until one of the HV channels reaches the maximum power supply current of 12 mA, at which point the voltage is abruptly ramped down. The current for the second channel remains just below the 12 mA trip point and decreases rapidly once the temperature decreases. It was possible to operate both HV channels of this power group by lowering the bias voltage and thus reducing the power dissipated on the sensors. A few more power groups experienced thermal runaway during the late stage of operation at -15°C; no thermal runaway has been observed when operating at -20°C during Run 2.

The leakage current is measured with two complementary approaches, one measuring the total current for a group of modules in the power supply units, the other measuring the leakage current of the individual modules using the DCU. The behavior for different parts of the strip tracker is investigated. The leakage current is extracted for a particular integrated luminosity and then scaled to $+20^{\circ}$C using eq. (7.3). These measurements are then plotted as functions of the fluence that the individual parts of the detector have received up to this moment, where the fluence generally decreases with increasing distance from the beam line. Results are reported in figure 45, where the leakage current per unit volume, scaled to $+20^{\circ}$C, is shown as a function of the fluence. A linear fit is performed to the data to extract the α-parameter. It should be noted that the amount of annealing for the individual sensors is not always the same because of the strong temperature differences in the SST (section 3), hence resulting in an “effective” α-parameter being derived rather than the one defined in eq. (7.2), which does not include annealing effects. Nevertheless, the fit describes the data reasonably well

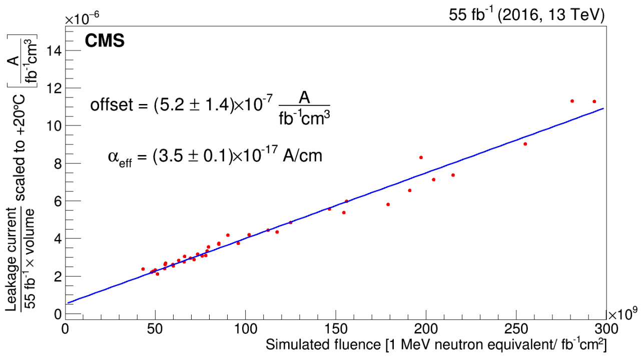

Figure 45. Leakage current per unit volume and integrated luminosity, scaled to +20°C, measured after an integrated luminosity of 55.4 fb^{-1} as a function of the simulated fluence for modules at different radii. A linear fit to the data is performed and used to extract the effective current related damage rate, α_{eff}.

and a value of $(3.5 \pm 0.1) \times 10^{-17}$ A/cm is obtained, which is in good agreement with the value of $(3.79 \pm 0.27) \times 10^{-17}$ A/cm found in ref. [1], in measurements on irradiated SST sensors.

Simulation is used to predict the future variation of the leakage current. Such simulations require the fluence as a function of the position inside the detector, the sensor temperature, and the available cooling power for each module as input parameters. The temperature change due to changes in operating conditions (e.g., change of coolant temperature) and self-heating can then be predicted. The self-heating is included iteratively in the simulation until either thermal runaway occurs or the procedure converges (that is, the increase in leakage current due to self-heating from the previous iteration is less than 1 nA).

At sufficiently high temperature, the radiation damage to the sensors will undergo annealing, which leads to a reduction of the leakage current. The simulation must include simultaneous annealing and radiation damage effects. This is done by calculating the increase in leakage current on a given day, based on the integrated luminosity or radiation dose on this day. This damage is then annealed based on the sensor temperature over the following days. The leakage current on any given day is thus a superposition of the initial leakage current measured before radiation exposure and the increments from each successive day.

The predicted leakage current and sensor temperature from the simulation are compared with measurements at specific times.

Figure 46 shows two examples of the variation of leakage current and temperature in both data and simulation as a function of time. The simulation tracks the measurements reasonably well. For both modules the temperatures during the Run 1 period agree well between simulation and measurement. The leakage current is well described for the TIB module during Run 1, with the simulation slightly overestimating the leakage current towards the end. For the TOB module the simulations similarly describe the data well with a slight underestimation towards the end of Run 1. During LS1 and two periods of Run 2, the simulation has many more points than are present in the data. This is because during periods when the detector is off there are no per-module measurements of temperature and leakage current, but the temperature can still be estimated rather precisely from nearby temperature sensors that are continuously read out. These temperature measurements are good proxies of the module temperature when the LV of the system is off and the system is thus in thermal equilibrium.

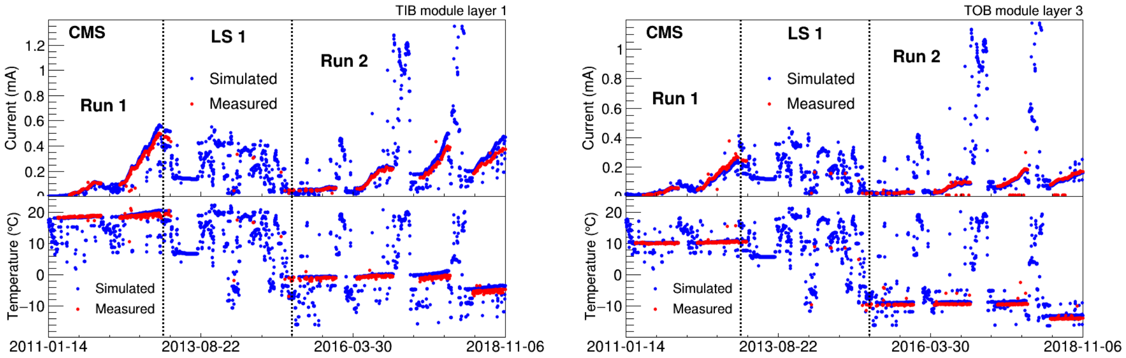

Figure 46. Leakage current and temperature measured by the DCU compared with simulation for a single module in the TIB layer 1 (left) and a module in TOB layer 3 (right).

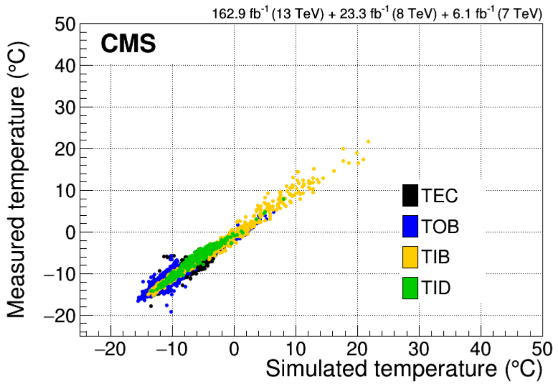

Figure 47. Silicon temperature as measured by the DCUs of the individual modules after 192.3 fb^{-1} of integrated luminosity, compared with simulation.

The temperature measurements can also be used in the simulation of annealing effects in periods without DCU readings. The peaks visible during Run 2 correspond to periods where the SST cooling plants were switched off. The high simulated current corresponds to the expected value under these conditions; in reality the sensors were never put under bias.

The measured and simulated sensor temperatures after exposure to 192.3 fb^{-1} of integrated luminosity are shown for all modules of the SST in figure 47. The simulated values agree well with those measured. The corresponding plot for the leakage current is shown in figure 48. Again, most modules are well described by the simulation. The simulation slightly underestimates the measured values in the TID, TOB, and TEC, but slightly overestimates them in the TIB.

The average leakage current for each layer, normalized to unit volume and scaled to a common temperature (0°C), is shown as a function of the integrated luminosity in figure 49 for the TIB (left) and the TOB (right). In general, the simulation reproduces the features of the data well, but underestimates the leakage current by about 20% consistently for all layers, even given the variation in their radial position. This discrepancy is not yet understood; possible factors are an imperfect modelling of the radiation environment in FLUKA, and uncertainties in the cooling contact, which can lead to an incorrect estimate for the self-heating.

2025 JINST 20 P08027

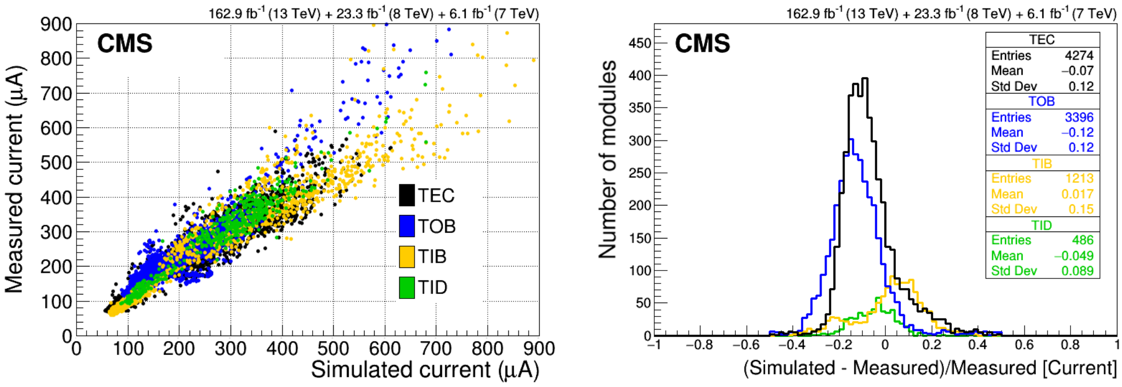

Figure 48. Left: leakage current as measured by the DCUs of the individual modules after 192.3 fb^{-1} of integrated luminosity, compared with simulation. Right: relative difference between predicted and measured leakage current after 192.3 fb^{-1}.

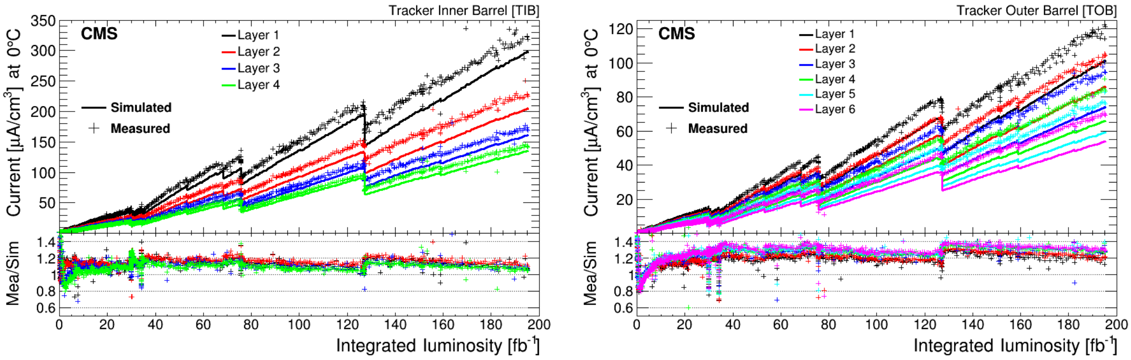

Figure 49. Leakage current for each layer scaled to unit volume and 0°C as a function of the total delivered integrated luminosity in the TIB (left) and TOB (right). The lower part of each plot shows the ratio of the measured and simulated current.

7.2.2 Depletion voltage evolution

The full-depletion voltage V_{dep} of a silicon sensor is the applied bias voltage at which the active silicon volume is completely depleted of free charge carriers. After installation, when direct measurements on the silicon sensors are no longer possible, the full-depletion voltage can be determined from the signal created by MIP-like particles. The variation of cluster charge and cluster size with bias voltage is investigated. This is called a ‘bias scan’ in the following. At the full-depletion voltage there is a noticeable change in behavior, an example of which is shown in figure 50 where the mean cluster size for on-track clusters is presented as a function of the bias voltage.

The cluster size increases below the full depletion because of the incomplete collection of the charge which results in lower strip charges, that have a higher probability to be below the zero-suppression threshold, especially in the tails of a cluster. Above the full depletion voltage the cluster decreases due to the increased charge collection speed which reduces the charge sharing between neighboring strips.

The kink in the measured data indicates that the full-depletion voltage has been reached. To determine the precise full-depletion voltage while accounting for the finite step size of the scan, the

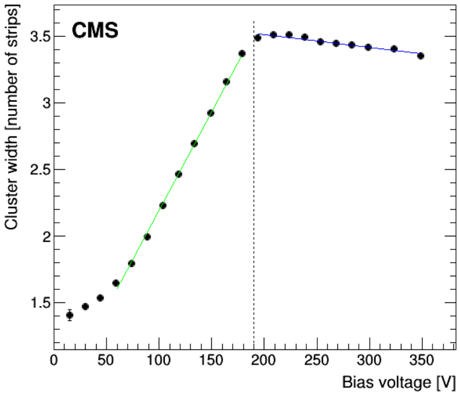

Figure 50. Example of the determination of the full-depletion voltage using the intersection of two linear fits to the cluster size data of one module. The dashed line indicates the derived full-depletion voltage.

measurements are fitted with two linear functions, one before the kink and one after it. The abscissa of the intersection point of the two functions is the full depletion voltage.

The effective doping concentration N_{eff} of silicon sensors changes with radiation dose due to the creation of point and cluster defects in the lattice structure [45]. Defects can be caused by energy deposition from both charged particles (mostly charged pions and protons) and neutral particles (mostly neutrons). The defects lead to (incomplete) donor removal and the creation of stable acceptor levels. For the n-type sensors of the SST this initially leads to a reduction of the effective doping concentration to the point of type inversion, after which the bulk becomes increasingly p-type effectively. The full-depletion voltage V_{dep} can be related to the effective doping concentration N_{eff} and to the resistivity ρ via

$$V_{\text{dep}} = \frac{|N_{\text{eff}}|\, d^2 q_0}{2\epsilon\epsilon_0} \quad \text{and} \quad V_{\text{dep}} = \frac{d^2}{2\epsilon\epsilon_0\mu\rho}, \tag{7.4}$$

where d is the sensor thickness, q_0 is the unit charge, μ is the electron mobility, and ϵ and ϵ_0 are the permittivity of silicon and the vacuum, respectively. The left formula is valid for the radiation fluences in the SST for which the effect of charge trapping can be neglected. The initial resistivity of the thin and thick sensor types is chosen to have similar initial depletion voltages. The values are in the range of $\rho = 1.55$–$3.25\,\text{k}\Omega\,\text{cm}$ for the $320\,\mu\text{m}$ thick sensors and $\rho = 4$–$8\,\text{k}\Omega\,\text{cm}$ for the $500\,\mu\text{m}$ thick sensors. Because of the higher resistivity of their bulk material, thick sensors are expected to reach type inversion at lower fluences than the thin sensors.

The evolution of the full-depletion voltage is monitored continuously during the operation of the SST by means of regular bias scans. In figure 51 (left) an example of the scan data used to extract the full-depletion voltage at various times is shown. The evolution of the full-depletion voltage as determined from these data is shown and compared with the expectations from simulation in figure 51 (right). In general, the simulation agrees well with the data. A small step downwards is visible around $30\,\text{fb}^{-1}$ in both data and simulation, with different magnitude. This corresponds to reverse annealing that happened during LS1 where the SST was at room temperature for extended periods of time. Comparing the size of this step in many modules suggests that the amount of reverse annealing is underestimated in the simulation.

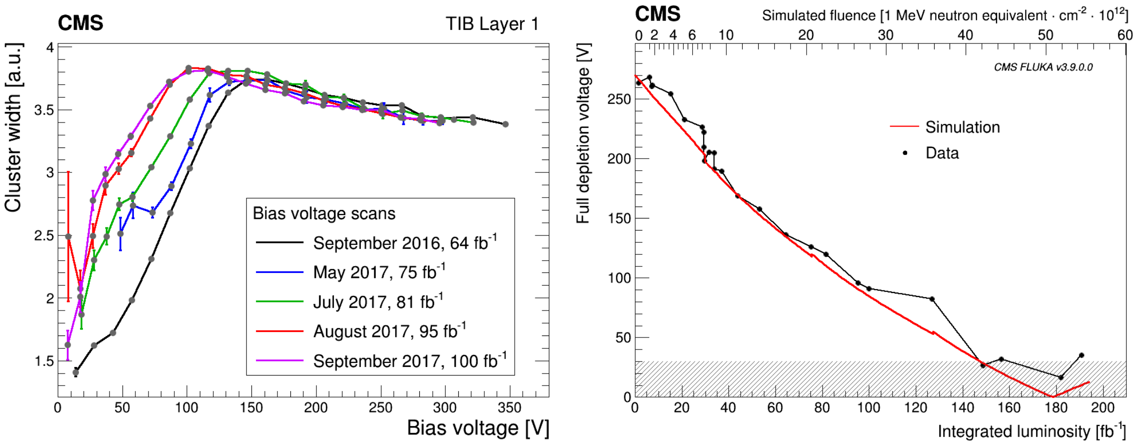

Figure 51. Left: mean cluster width as a function of the sensor bias voltage for one module in the TIB layer 1 for bias scans taken at various integrated luminosities. The curves have been normalized to the same cluster width at the highest bias voltage of the scans. Right: evolution of the full-depletion voltage for one TIB layer 1 module as a function of the integrated luminosity (lower x axis) and fluence (upper x axis) using the data from bias scans. The red line shows the predicted full-depletion voltage. The gray hashed area indicates the region where depletion voltage estimates from data have a large uncertainty.

The average change of the full-depletion voltage for each layer in the TIB and TOB as a function of the fluence is shown in figure 52 for both data (left) and simulation (right). For data the integrated luminosity is converted to the expected fluence for each module using a FLUKA simulation. As expected, different behavior for the thin and thick sensors is clearly visible in the data and reproduced in simulation. Furthermore, the change of V_{dep} is similar for different sensor geometries. The range of simulated fluence stops just before the sensors reach type inversion; here the determination of V_{dep} becomes unreliable. At the end of Run 2 many sensors of the SST are at or close to type inversion.

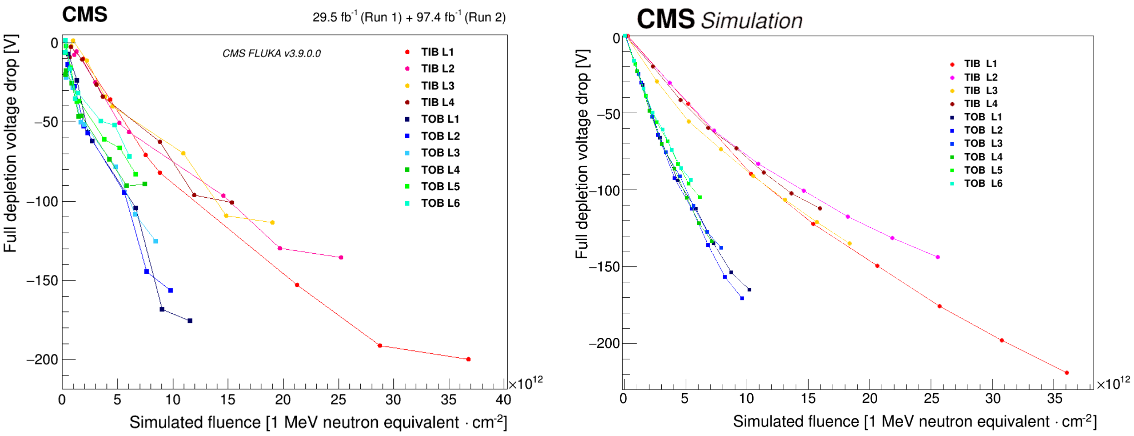

Figure 52. Left: change of the full-depletion voltage in different tracker layers as a function of the particle fluence in data. Scans at different integrated luminosities are shown. The luminosity is converted to particle fluence for each position in the detector using a FLUKA model. Right: simulated change of the full-depletion voltage for single modules in different tracker layers as a function of the particle fluence.

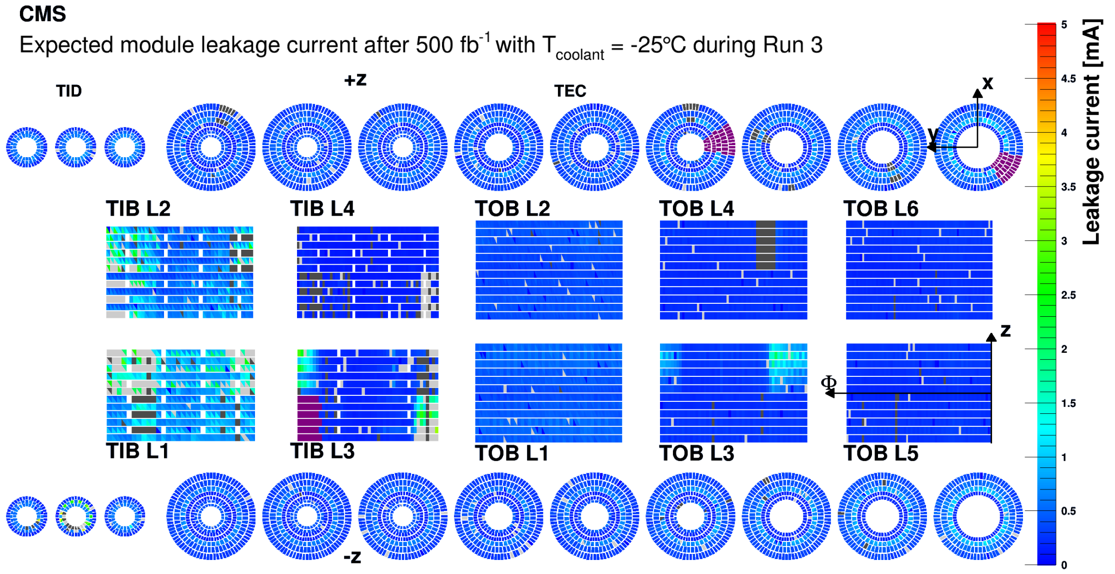

Figure 53. Tracker map of predicted leakage current at the end of life of the SST, where each silicon module is represented by a rectangle in the barrel and a trapezoid in the endcap; in stereo modules each submodule constitutes one half of this area. The color scale shows the projected sensor leakage current for a total integrated luminosity of 500 fb^{-1} with the SST operated at -25°C during all of Run 3. Modules in dark gray were already inoperable at the end of Run 2. Modules in light gray are expected to become inoperable during Run 3 because their projected leakage current will be too high. Regions in purple are control rings with DCU readout issues, implying no input data for the simulation.

7.2.3 Radiation damage projections

Simulation is used to predict the status of the SST at its end of life. This is assumed to be at the end of Run 3, after an integrated luminosity of 500 fb^{-1} while operating with a cooling fluid temperature of -25°C.

The SST was warm for about 160 days during LS2, over periods where cold operation was not possible. These were during the removal and reinstallation of the pixel detector, as well as during removal, reinstallation, and bake out of the central beam pipe, when there was insufficient humidity control, e.g., in the bulkhead. The simulation here assumes a total of 120 days at room temperature during LS2. Although this is slightly lower than the actual, the equilibrium temperature used in the simulation is $+18^{\circ}$C, whereas the actual temperature of the detector was around $+16^{\circ}$C during warm periods. During future year-end technical stops the temperature is assumed to be maintained near or below 0°C, by means of the primary detector cooling or with the thermal screen cooling, as described in section 2.

The predicted leakage current after 500 fb^{-1} of integrated luminosity is shown in figure 53. The gray areas of the detector in TIB layers 1, 2, and 3, and in the $-z$ disk 2 of the TID are regions where either the maximum power supply current of 12 mA per HV channel is reached or where one or more modules connected to the same HV channel have experienced thermal runaway. The purple regions are those that lacked appropriate input parameters for the simulation (TEC+ disks 6 and 9, and TIB layer 3, TOB layer 4) as DCU readout on these control rings was not possible. The modules that are expected to become inoperable from excessive leakage current correspond very closely to the regions with elevated

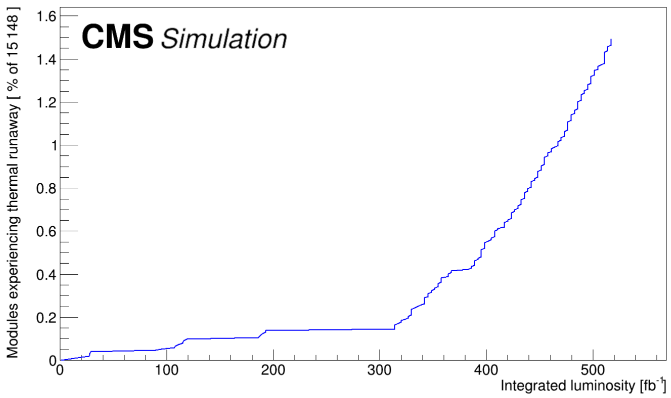

Figure 54. Fraction of modules affected by thermal runaway as a function of the integrated luminosity.

temperatures from figure 7. The total number of inactive modules is smaller than that anticipated in figure 2.24 of ref. [4], suggesting a less severe degradation of the system: fewer bad modules are expected especially in TIB layer 2 and TOB layer 4. Some groups of modules in the TIB layers 1, 2, and 3 show elevated leakage currents of around 2–3 mA per module and these could also potentially become inoperable. Because of their limited number, the overall assessment does not change.

In figure 54, the percentage of modules experiencing thermal runaway is shown as a function of the integrated luminosity. The number of such modules increases rapidly above 300 fb^{-1} and reaches about 1.5% at 500 fb^{-1}. A module is considered to reach thermal runaway if during the iterative simulation the self-heating contribution continues to increase.

Predictions are made for the full-depletion voltage at the end of life of the SST. The predicted full-depletion voltage at 500 fb^{-1} is shown in figure 55.

The highest full-depletion voltage is expected to be around 275 V, suggesting that there is ample margin with respect to the maximum bias voltage of 600 V that can be delivered by the power supply system. Modules that suffer most from reverse annealing due to high operating temperatures are not included here since they are expected to either reach the power supply current limit or experience thermal runaway before a possible limit in full-depletion voltage becomes relevant.

8 Summary and outlook

In this paper, the calibration, operation, and performance of the CMS silicon strip tracker (SST) were presented. The SST has successfully delivered measurements for the reconstruction of charged particle trajectories since the start of LHC operation.

First the calibration of the SST was discussed. It was demonstrated that the system behavior is well understood over 10 years of operation, which includes different operating temperatures and ever increasing instantaneous luminosities over the course of the data taking.

Next, the ingredients necessary for a proper simulation of the SST were considered. Measurements required as input to the simulation, obtained in special runs, were presented.

The performance with proton-proton collisions was then extensively discussed. The single-hit occupancy of the system is in line with expectations even while running at twice the design instantaneous luminosity. The dynamic identification of bad components, crucial for a proper handling

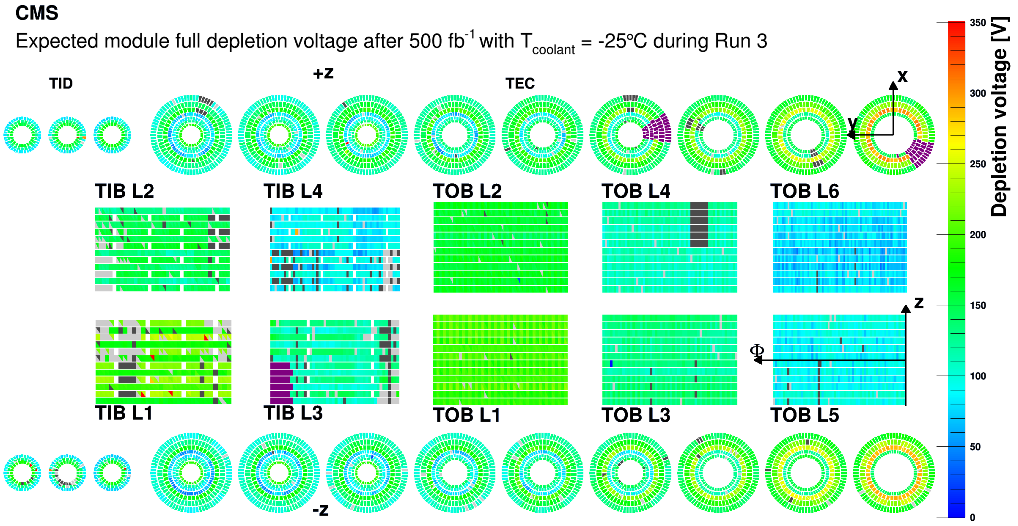

Figure 55. Tracker map of predicted full-depletion voltage at the end of life of the SST, where each silicon module is represented by a rectangle in the barrel and a trapezoid in the endcap; in stereo modules each submodule constitutes one half of this area. The color scale shows the projected full-depletion voltage for a total integrated luminosity of 500 fb^{-1} with the SST operated at -25°C during all of Run 3. Modules in dark gray were already inoperable at the end of Run 2. Modules in light gray are expected to become inoperable during Run 3 because their projected leakage current will be too high and are identical to the modules depicted in light grey in figure 53. Regions in purple are control rings with DCU readout issues, implying no input data for the simulation.

of missing hits in the subsequent reconstruction of particle tracks, was introduced and shown to work well. Saturation effects in the APV25 preamplifier, which resulted in a reduced track reconstruction efficiency, were identified during 2015–2016. This problem was understood and resolved in mid-2016. The signal-to-noise performance of the system was excellent even after almost 200 fb^{-1} of integrated luminosity. The outlook toward the expected end-of-life integrated luminosity is in line with expectations. As a result, the system shows excellent single-hit reconstruction efficiency because of the analog readout that enables a hit resolution significantly better than the binary limit for the most relevant cluster sizes. The evolution of the Lorentz angle as a function of the integrated luminosity was shown, as was a measurement of the specific energy loss of particles, made possible by the analog readout, which is useful for more sophisticated analyses of collision events.

Finally, radiation effects in the SST were examined, with focus on the effects in the laser diodes of the optical link system and the effects on the properties of the silicon sensors. The threshold current increase in the laser diodes was shown to behave as expected, leaving ample margin for the future operation of the SST. For the bulk damage of the silicon sensor, the resulting effects on the leakage current and full-depletion voltage were shown and compared with simulations. The evolution of both leakage current and depletion voltage is well described by models, and the outlook to the expected end of life of the SST shows that the vast majority of the modules should continue to function well. Those modules that are expected to become inoperable are in regions of the SST affected by cooling-related problems encountered during early operation; the extent of problems is expected to be lower than anticipated from earlier projections. The small fraction of about 1.5% of affected modules is not expected to severely affect the SST's ability to provide high-quality measurements for track reconstruction until the start of LS3, when the tracking system will be replaced for the High-Luminosity LHC era.

Acknowledgments

We congratulate our colleagues in the CERN accelerator departments for the excellent performance of the LHC and thank the technical and administrative staffs at CERN and at other CMS institutes for their contributions to the success of the CMS effort. In addition, we gratefully acknowledge the computing centers and personnel of the Worldwide LHC Computing Grid and other centers for delivering so effectively the computing infrastructure essential to our analyses. Finally, we acknowledge the enduring support for the construction and operation of the LHC, the CMS detector, and the supporting computing infrastructure provided by the following funding agencies: SC (Armenia), BMBWF and FWF (Austria); FNRS and FWO (Belgium); CNPq, CAPES, FAPERJ, FAPERGS, and FAPESP (Brazil); MES and BNSF (Bulgaria); CERN; CAS, MoST, and NSFC (China); MINCIENCIAS (Colombia); MSES and CSF (Croatia); RIF (Cyprus); SENESCYT (Ecuador); ERC PRG, RVTT3 and MoER TK202 (Estonia); Academy of Finland, MEC, and HIP (Finland); CEA and CNRS/IN2P3 (France); SRNSF (Georgia); BMBF, DFG, and HGF (Germany); GSRI (Greece); NKFIH (Hungary); DAE and DST (India); IPM (Iran); SFI (Ireland); INFN (Italy); MSIP and NRF (Republic of Korea); MES (Latvia); LMTLT (Lithuania); MOE and UM (Malaysia); BUAP, CINVESTAV, CONACYT, LNS, SEP, and UASLP-FAI (Mexico); MOS (Montenegro); MBIE (New Zealand); PAEC (Pakistan); MES and NSC (Poland); FCT (Portugal); MESTD (Serbia); MICIU/AEI and PCTI (Spain); MOSTR (Sri Lanka); Swiss Funding Agencies (Switzerland); MST (Taipei); MHESI and NSTDA (Thailand); TUBITAK and TENMAK (Turkey); NASU (Ukraine); STFC (United Kingdom); DOE and NSF (U.S.A.).

Individuals have received support from the Marie-Curie program and the European Research Council and Horizon 2020 Grant, contract Nos. 675440, 724704, 752730, 758316, 765710, 824093, 101115353, 101002207, and COST Action CA16108 (European Union); the Leventis Foundation; the Alfred P. Sloan Foundation; the Alexander von Humboldt Foundation; the Science Committee, project no. 22rl-037 (Armenia); the Fonds pour la Formation à la Recherche dans l'Industrie et dans l'Agriculture (FRIA-Belgium); the Beijing Municipal Science & Technology Commission, No. Z191100007219010 and Fundamental Research Funds for the Central Universities (China); the Ministry of Education, Youth and Sports (MEYS) of the Czech Republic; the Shota Rustaveli National Science Foundation, grant FR-22-985 (Georgia); the Deutsche Forschungsgemeinschaft (DFG), among others, under Germany's Excellence Strategy — EXC 2121 "Quantum Universe" — 390833306, and under project number 400140256 - GRK2497; the Hellenic Foundation for Research and Innovation (HFRI), Project Number 2288 (Greece); the Hungarian Academy of Sciences, the New National Excellence Program - ÚNKP, the NKFIH research grants K 131991, K 133046, K 138136, K 143460, K 143477, K 146913, K 146914, K 147048, 2020-2.2.1-ED-2021-00181, TKP2021-NKTA-64, and 2021-4.1.2-NEMZ_KI-2024-00036 (Hungary); the Council of Science and Industrial Research, India; ICSC — National Research Center for High Performance Computing, Big Data and Quantum Computing and FAIR — Future Artificial Intelligence Research, funded by the NextGenerationEU program (Italy); the Latvian Council of Science; the Ministry of Education and Science, project no. 2022/WK/14, and the National Science Center, contracts Opus 2021/41/B/ST2/01369 and 2021/43/B/ST2/01552 (Poland); the Fundação para a Ciência e a Tecnologia, grant CEECIND/01334/2018 (Portugal); the National Priorities Research Program by Qatar National Research Fund; MICIU/AEI/10.13039/501100011033, ERDF/EU, "European Union NextGenerationEU/PRTR", and Programa Severo Ochoa del Principado de Asturias (Spain); the Chulalongkorn Academic into Its 2nd Century Project Advancement Project, and the National Science, Research and Innovation Fund via the Program Management Unit for Human

Resources & Institutional Development, Research and Innovation, grant B39G670016 (Thailand); the Kavli Foundation; the Nvidia Corporation; the SuperMicro Corporation; the Welch Foundation, contract C-1845; and the Weston Havens Foundation (U.S.A.).

A Glossary of special terms and acronyms

ADC:	Analog-to-digital converter
AOH:	Analog Optohybrid, used in the auxiliary electronics of the CMS silicon strip tracker
APSP:	Analog pulse shape processor
APV:	Analog pipeline voltage
APV25:	Readout chip used in the CMS silicon strip tracker
APVMUX:	Auxiliary chip to multiplex the outputs of two APV25 chips
ASIC:	Application-specific integrated circuit
BX:	Bunch crossing
CCU:	Communication and Control Unit, used in the auxiliary electronics of the CMS silicon strip tracker
DAQ:	Data acquisition
DCU:	Detector Control Unit, used in the auxiliary electronics of the CMS silicon strip tracker
DOH:	Digital Optohybrid, used in the auxiliary electronics of the CMS silicon strip tracker
ENC:	Equivalent noise charge
FEC:	Front-End Controller, used in the DAQ system of the CMS silicon strip tracker
FED:	Front-End Driver, used in the DAQ system of the CMS silicon strip tracker
FEH:	Front-end hybrid
FET:	Field-effect transistor
HIP:	Highly ionizing particle
HL-LHC:	High-Luminosity LHC
HV:	High voltage
$\mathrm{I}^2\mathrm{C}$:	Inter-integrated circuit
I_{leak}:	Silicon sensor leakage current
λ_0:	Interaction length
L1A:	CMS level-1 trigger accept signal
LHC:	Large Hadron Collider
LLD:	Linear Laser Driver, used in the auxiliary electronics of the CMS silicon strip tracker
LS1:	Long Shutdown 1 (2013–2014)
LS2:	Long Shutdown 2 (2019–2021)
LS3:	Long Shutdown 3 (2026–2030)
LV:	Low voltage
MC:	Monte Carlo
mFEC:	Mezzanine card on the FEC, used in the DAQ system of the CMS silicon strip tracker, for the communication to an individual control ring
MIP:	Minimum-ionizing particle
MPV:	Most probable value, of a Landau distribution
N_{eff}:	Effective doping concentration of a silicon sensor
NIEL:	Non-ionizing energy loss
NZS:	Data with no zero suppression applied
PLL:	Phase-locked loop
PSU:	Power supply unit
PU:	Pileup
RMS:	Root-mean-square
Run 1:	First data-taking period at the LHC (2009–2012)
Run 2:	Second data-taking period at the LHC (2015–2018)
Run 3:	Third data-taking period at the LHC (2022–2026)
S/N:	Signal-to-noise ratio
SST:	Silicon strip tracker of the CMS experiment

TIB:	Tracker Inner Barrel, a subdetector of the SST
TID:	Tracker Inner Disk, a subdetector of the SST
TEC:	Tracker Endcap, a subdetector of the SST
TOB:	Tracker Outer Barrel, a subdetector of the SST
TTS:	Trigger throttling system
V_{dep}:	Silicon sensor full-depletion voltage
VFP:	Preamplifier feedback voltage bias, setting to control the discharge speed of the APV25 preamplifier
X_0:	Radiation length
ZS:	Zero-suppressed

Data Availability Statement. This article has associated data in a data repository. Release and preservation of data used by the CMS Collaboration as the basis for publications is guided by the CMS data preservation, re-use and open access policy.

Code Availability Statement. This article has associated code in a code repository. The CMS core software is publicly available on GitHub.

References

[1] CMS collaboration, *The CMS Experiment at the CERN LHC*, 2008 *JINST* **3** S08004.

[2] L. Evans and P. Bryant, *LHC Machine*, 2008 *JINST* **3** S08001.

[3] CMS collaboration, *The CMS tracker system project: Technical Design Report*, CERN-LHCC-98-06 (1998).

[4] A. Dominguez et al., *CMS Technical Design Report for the Pixel Detector Upgrade*, CERN-LHCC-2012-016 (2012).

[5] CMS Tracker collaboration, *The CMS Phase-1 Pixel Detector Upgrade*, 2021 *JINST* **16** P02027 [`arXiv:2012.14304`].

[6] CMS collaboration, *The CMS tracker: addendum to the Technical Design Report*, CERN-LHCC-2000-016, CERN, Geneva (2000).

[7] CMS collaboration, *Track Reconstruction with Cosmic Ray Data at the Tracker Integration Facility*, CMS-NOTE-2009-003, CERN, Geneva (2008).

[8] CMS Tracker collaboration, *Performance studies of the CMS Strip Tracker before installation*, 2009 *JINST* **4** P06009 [`arXiv:0901.4316`].

[9] CMS collaboration, *Commissioning and Performance of the CMS Silicon Strip Tracker with Cosmic Ray Muons*, 2010 *JINST* **5** T03008 [`arXiv:0911.4996`].

[10] CMS collaboration, *Public CMS luminosity information*, https://twiki.cern.ch/twiki/bin/view/CMSPublic/LumiPublicResults.

[11] CMS collaboration, *Description and Performance of Track and Primary-Vertex Reconstruction with the CMS Tracker*, 2014 *JINST* **9** P10009 [`arXiv:1405.6569`].

[12] CMS collaboration, *Development of the CMS detector for the CERN LHC Run 3*, 2024 *JINST* **19** P05064 [`arXiv:2309.05466`].

[13] L.L. Jones et al., *The APV25 deep submicron readout chip for CMS detectors*, *Conf. Proc. C* **9909201** (1999) 162 [`DOI:10.5170/CERN-1999-009.162`].

[14] G. Cervelli, A. Marchioro, P. Moreira and F. Vasey, *A linear laser-driver array for optical transmission in the LHC experiments*, in the proceedings of the *IEEE Nuclear Science Symposium*, Lyon, France, October 15–20 (2000) [`DOI:10.1109/nssmic.2000.949887`].

[15] J. Troska et al., *Optical readout and control systems for the CMS tracker*, *IEEE Trans. Nucl. Sci.* **50** (2003) 1067.

[16] J.A. Coughlan et al., *The CMS tracker front-end driver*, in the proceedings of the *9th Workshop on Electronics for LHC Experiments*, Amsterdam, Netherlands, September 29–October 3 (2003) CERN-2003-006, CERN, Geneva (2003) [`DOI:10.5170/CERN-2003-006.255`].

[17] C. Paillard, C. Ljuslin and A. Marchioro, *The CCU25: A network oriented communication and control unit integrated circuit in a 0.25* µ*m CMOS technology*, in the proceedings of the *8th Workshop on Electronics for LHC Experiments*, Colmar, France, September 09–13 (2002). [`DOI:10.5170/CERN-2002-003.174`]

[18] K. Gill et al., *Progress on the CMS Tracker control system*, in the proceedings of the *11th Workshop on Electronics for LHC and Future Experiments (LECC 2005)*, Heidelberg, Germany, September 12–16 (2005). [`DOI:10.5170/CERN-2005-011.353`]

[19] L. Borrello, A. Messineo, E. Focardi and A. Macchiolo, *Sensor Design for the CMS Silicon Strip Tracker*, CMS-NOTE-2003-020, CERN, Geneva (2003).

[20] S. Braibant et al., *Investigation of design parameters for radiation hard silicon microstrip detectors*, *Nucl. Instrum. Meth. A* **485** (2002) 343.

[21] S. Gadomski et al., *The deconvolution method of fast pulse shaping at hadron colliders*, *Nucl. Instrum. Meth. A* **320** (1992) 217.

[22] G. Magazzu, A. Marchioro and P. Moreira, *The detector control unit: An ASIC for the monitoring of the CMS silicon tracker*, *IEEE Trans. Nucl. Sci.* **51** (2004) 1333.

[23] P. Placidi, A. Marchioro, P. Moreira and K. Kloukinas, *A 40-MHz clock and trigger recovery circuit for the CMS tracker fabricated in a 0.25 upmum CMOS technology and using a selfcalibration technique*, in the proceedings of the *5th Workshop on Electronics for the LHC Experiments (LEB 99)*, Snowmass, U.S.A., September 20–24 (1999) [10.5170/CERN-1999-009.469].

[24] NXP, *I^2C-bus specification and user manual*, https://www.nxp.com/docs/en/user-guide/UM10204.pdf.

[25] S. Paoletti, A. Bocci, R. D'Alessandro, and G. Parrini, *The powering systems of the CMS tracker for HL-LHC*, 2022 *JINST* **17** C12015 [`DOI:10.5170/CERN-2004-010.194`].

[26] CMS collaboration, *Commissioning the CMS Silicon Strip Tracker prior to Operations with Cosmic Ray Muons*, CMS-NOTE-2009-021, CERN, Geneva (2009).

[27] S. Dris, K. Gill, J. Troska and F. Vasey, *Predicting the Gain Spread of the CMS Tracker Analog Readout Optical Links*, CMS-NOTE-2006-145, CERN, Geneva (2006).

[28] C. Delaere and L. Mirabito, *Timing of the CMS tracker*, CMS-NOTE-2007-027, CERN, Geneva (2007).

[29] M. Hildreth, V.N. Ivanchenko, D.J. Lange and M.J. Kortelainen, *CMS Full Simulation for Run-2*, *J. Phys. Conf. Ser.* **664** (2015) 072022.

[30] GEANT4 collaboration, *GEANT4 — A Simulation Toolkit*, *Nucl. Instrum. Meth. A* **506** (2003) 250.

[31] M. Jansova, *Search for the supersymmetric partner of the top quark and measurements of cluster properties in the silicon strip tracker of the CMS experiment at Run 2*, Ph.D. thesis, Université de Strasbourg, Strasbourg, France (2018).

[32] CMS collaboration, *Strategies and performance of the CMS silicon tracker alignment during LHC Run 2*, *Nucl. Instrum. Meth. A* **1037** (2022) 166795 [`arXiv:2111.08757`].

[33] Particle Data Group collaboration, *Review of particle physics*, *Phys. Rev. D* **110** (2024) 030001.

[34] C. Foudas et al., *The CMS tracker readout front end driver*, *IEEE Trans. Nucl. Sci.* **52** (2005) 2836 [`physics/0510229`].

[35] CMS collaboration, *Measurements of Inclusive W and Z Cross Sections in pp Collisions at* $\sqrt{s} = 7$ *TeV*, *JHEP* **01** (2011) 080 [`arXiv:1012.2466`].

[36] CMS collaboration, *Muon tracking performance in the CMS Run-2 Legacy data using the tag-and-probe technique*, CMS-DP-2020-035 (2020).

[37] L. Tuura, A. Meyer, I. Segoni and G. Della Ricca, *CMS data quality monitoring: Systems and experiences*, *J. Phys. Conf. Ser.* **219** (2010) 072020.

[38] L. Quertenmont, *Search for Heavy Stable Charged Particles with the CMS detector at the LHC*, Ph.D. thesis, Université catholique de Louvain, Louvain, Belgium (2010) [CERN-THESIS-2010-236].

[39] V. Bartsch et al., *An algorithm for calculating the Lorentz angle in silicon detectors*, *Nucl. Instrum. Meth. A* **497** (2003) 389 [`physics/0204078`].

[40] W. Adam et al., *The effect of highly ionising particles on the CMS silicon strip tracker*, *Nucl. Instrum. Meth. A* **543** (2005) 463.

[41] R. Bainbridge et al., *The Effect of Highly Ionising Events on the APV25 Readout Chip*, CMS-NOTE-2002-038, CERN, Geneva (2002).

[42] CMS Tracker collaboration, *Stand-alone Cosmic Muon Reconstruction Before Installation of the CMS Silicon Strip Tracker*, 2009 *JINST* **4** P05004 [`arXiv:0902.1860`].

[43] P. Aarnio, K. Ekman, T. Nyman and P. Salonen, *CMS, the Compact Muon Solenoid: Technical proposal*, CERN-LHCC-94-38 (1994).

[44] CMS collaboration, *Search for long-lived charged particles in proton-proton collisions at* $\sqrt{s} = 13$ *TeV*, *Phys. Rev. D* **94** (2016) 112004 [`arXiv:1609.08382`].

[45] M. Moll, *Radiation damage in silicon particle detectors: Microscopic defects and macroscopic properties*, Ph.D. thesis, Hamburg Univeristy, Hamburg, Germany (1999).

[46] K. Gill et al., *Radiation hardness assurance and reliability testing of InGaAs photodiodes for optical control links for the CMS experiment*, *IEEE Trans. Nucl. Sci.* **52** (2005) 1480.

[47] A. Ferrari, P.R. Sala, A. Fassò and J. Ranft, *FLUKA*, CERN-2005-010, CERN, Geneva (2005) [`DOI:10.5170/CERN-2005-010`].

[48] T.T. Böhlen et al., *The FLUKA Code: Developments and Challenges for High Energy and Medical Applications*, *Nucl. Data Sheets* **120** (2014) 211.

[49] R. Macias, *Laser threshold current and efficiency at temperatures between* $-20^\circ C$ *and* $+20^\circ C$, EDMS document, CMS-TK-TR-0036, 2003. https://edms.cern.ch/ui/file/430290/1/Thresh-Eff-Temp.pdf.

[50] K. Gill, R. Grabit, J. Troska and F. Vasey, *Radiation hardness qualification of InGaAsP/InP 1310-nm lasers for the CMS tracker optical links*, *IEEE Trans. Nucl. Sci.* **49** (2002) 2923.

[51] T. Kohriki et al., *First observation of thermal runaway in the radiation damaged silicon detector*, *IEEE Trans. Nucl. Sci.* **43** (1996) 1200.

The CMS collaboration

Yerevan Physics Institute, Yerevan, Armenia

A. Hayrapetyan, A. Tumasyan[1]

Institut für Hochenergiephysik, Vienna, Austria

W. Adam, J.W. Andrejkovic, T. Bergauer, S. Chatterjee, K. Damanakis, M. Dragicevic, M. Friedl, E. Frühwirth, P.S. Hussain, M. Jeitler[2], N. Krammer, A. Li, D. Liko, I. Mikulec, J. Schieck[2], R. Schöfbeck, D. Schwarz, M. Sonawane, H. Steininger, S. Templ, W. Waltenberger, C.-E. Wulz[2]

Universiteit Antwerpen, Antwerpen, Belgium

W. Beaumont, M.R. Darwish[3], T. Janssen, D. Ocampo Henao, T. Van Laer, P. Van Mechelen

Vrije Universiteit Brussel, Brussel, Belgium

J. Bierkens, E.S. Bols, N. Breugelmans, J. D'Hondt, S. Dansana, A. De Moor, M. Delcourt, F. Heyen, S. Lowette, I. Makarenko, D. Müller, S. Tavernier, M. Tytgat[4], G.P. Van Onsem, S. Van Putte, D. Vannerom

Université Libre de Bruxelles, Bruxelles, Belgium

Y. Allard, F. Caviglia Roman, B. Clerbaux, A.K. Das, G. De Lentdecker, E. Ducarme, H. Evard, L. Favart, P. Gianneios, D. Hohov, J. Jaramillo, I. Kalaitzidou, A. Khalilzadeh, F.A. Khan, M. Korntheuer, K. Lee, M. Mahdavikhorrami, A. Malara, S. Paredes, F. Robert, M.A. Shahzad, L. Thomas, M. Vanden Bemden, C. Vander Velde, P. Vanlaer, C. Yuan

Ghent University, Ghent, Belgium

M. De Coen, D. Dobur, Y. Hong, J. Knolle, L. Lambrecht, G. Mestdach, K. Mota Amarilo, C. Rendón, K. Skovpen, N. Van Den Bossche, J. van der Linden, L. Wezenbeek, Y. Yang

Université Catholique de Louvain, Louvain-la-Neuve, Belgium

A. Benecke, A. Bethani, G. Bruno, C. Caputo, J. De Favereau De Jeneret, C. Delaere, I.S. Donertas, A. Giammanco, A.O. Guzel, Sa. Jain, V. Lemaitre, J. Lidrych, P. Mastrapasqua, N. Szilasi, T.T. Tran, S. Wertz

Centro Brasileiro de Pesquisas Fisicas, Rio de Janeiro, Brazil

G.A. Alves, E. Coelho, C. Hensel, T. Menezes De Oliveira, A. Moraes, P. Rebello Teles, M. Soeiro, A. Vilela Pereira[5]

Universidade do Estado do Rio de Janeiro, Rio de Janeiro, Brazil

W.L. Aldá Júnior, M. Alves Gallo Pereira, M. Barroso Ferreira Filho, H. Brandao Malbouisson, W. Carvalho, J. Chinellato[6], E.M. Da Costa, G.G. Da Silveira[7], D. De Jesus Damiao, S. Fonseca De Souza, R. Gomes De Souza, M. Macedo, J. Martins[8], C. Mora Herrera, L. Mundim, H. Nogima, J.P. Pinheiro, A. Santoro, A. Sznajder, M. Thiel

Universidade Estadual Paulista, Universidade Federal do ABC, São Paulo, Brazil

C.A. Bernardes[7], L. Calligaris, T.R. Fernandez Perez Tomei, E.M. Gregores, I. Maietto Silverio, P.G. Mercadante, S.F. Novaes, B. Orzari, Sandra S. Padula

Institute for Nuclear Research and Nuclear Energy, Bulgarian Academy of Sciences, Sofia, Bulgaria
A. Aleksandrov, G. Antchev, R. Hadjiiska, P. Iaydjiev, M. Misheva, M. Shopova, G. Sultanov

University of Sofia, Sofia, Bulgaria
A. Dimitrov, L. Litov, B. Pavlov, P. Petkov, A. Petrov, E. Shumka

Instituto De Alta Investigación, Universidad de Tarapacá, Casilla 7 D, Arica, Chile
S. Keshri, S. Thakur

Beihang University, Beijing, China
T. Cheng, T. Javaid, L. Yuan

Department of Physics, Tsinghua University, Beijing, China
Z. Hu, Z. Liang, J. Liu, K. Yi[9,10]

Institute of High Energy Physics, Beijing, China
G.M. Chen[11], H.S. Chen[11], M. Chen[11], F. Iemmi, C.H. Jiang, A. Kapoor[12], H. Liao, Z.-A. Liu[13], R. Sharma[14], J.N. Song[13], J. Tao, C. Wang[11], J. Wang, Z. Wang[11], H. Zhang

State Key Laboratory of Nuclear Physics and Technology, Peking University, Beijing, China
A. Agapitos, Y. Ban, A. Levin, C. Li, Q. Li, Y. Mao, S. Qian, S.J. Qian, X. Sun, D. Wang, H. Yang, L. Zhang, Y. Zhao, C. Zhou

Sun Yat-Sen University, Guangzhou, China
Z. You

University of Science and Technology of China, Hefei, China
K. Jaffel, N. Lu

Nanjing Normal University, Nanjing, China
G. Bauer[15]

Institute of Modern Physics and Key Laboratory of Nuclear Physics and Ion-beam Application (MOE) - Fudan University, Shanghai, China
X. Gao[16]

Zhejiang University, Hangzhou, Zhejiang, China
Z. Lin, C. Lu, M. Xiao

Universidad de Los Andes, Bogota, Colombia
C. Avila, D.A. Barbosa Trujillo, A. Cabrera, C. Florez, J. Fraga, J.A. Reyes Vega

Universidad de Antioquia, Medellin, Colombia
J. Mejia Guisao, F. Ramirez, M. Rodriguez, J.D. Ruiz Alvarez

University of Split, Faculty of Electrical Engineering, Mechanical Engineering and Naval Architecture, Split, Croatia

D. Giljanovic, N. Godinovic, D. Lelas, A. Sculac

University of Split, Faculty of Science, Split, Croatia

M. Kovac, A. Petkovic, T. Sculac

Institute Rudjer Boskovic, Zagreb, Croatia

P. Bargassa, V. Brigljevic, B.K. Chitroda, D. Ferencek, K. Jakovcic, S. Mishra, A. Starodumov[17], T. Susa

University of Cyprus, Nicosia, Cyprus

A. Attikis, K. Christoforou, A. Hadjiagapiou, C. Leonidou, J. Mousa, C. Nicolaou, L. Paizanos, F. Ptochos, P.A. Razis, H. Rykaczewski, H. Saka, A. Stepennov

Charles University, Prague, Czech Republic

M. Finger, M. Finger Jr., A. Kveton

Escuela Politecnica Nacional, Quito, Ecuador

E. Ayala

Universidad San Francisco de Quito, Quito, Ecuador

E. Carrera Jarrin

Academy of Scientific Research and Technology of the Arab Republic of Egypt, Egyptian Network of High Energy Physics, Cairo, Egypt

A.A. Abdelalim[18,19], E. Salama[20,21]

Center for High Energy Physics (CHEP-FU), Fayoum University, El-Fayoum, Egypt

M. Abdullah Al-Mashad, M.A. Mahmoud

National Institute of Chemical Physics and Biophysics, Tallinn, Estonia

K. Ehataht, M. Kadastik, T. Lange, S. Nandan, C. Nielsen, J. Pata, M. Raidal, L. Tani, C. Veelken

Department of Physics, University of Helsinki, Helsinki, Finland

H. Kirschenmann, K. Osterberg, M. Voutilainen

Helsinki Institute of Physics, Helsinki, Finland

S. Bharthuar, E. Brücken, F. Garcia, T. Hilden, K.T.S. Kallonen, R. Kinnunen, T. Lampén, K. Lassila-Perini, S. Lehti, T. Lindén, L. Martikainen, M. Myllymäki, M.m. Rantanen, S. Saariokari, H. Siikonen, E. Tuominen, J. Tuominiemi

Lappeenranta-Lahti University of Technology, Lappeenranta, Finland

A. Karadzhinova, P. Luukka, H. Petrow, T. Tuuva[†], M.P. Vaananen

IRFU, CEA, Université Paris-Saclay, Gif-sur-Yvette, France
M. Besancon, F. Couderc, M. Dejardin, D. Denegri, J.L. Faure, F. Ferri, S. Ganjour, P. Gras, G. Hamel de Monchenault, V. Lohezic, J. Malcles, F. Orlandi, L. Portales, J. Rander, A. Rosowsky, M.Ö. Sahin, A. Savoy-Navarro[22], P. Simkina, M. Titov, M. Tornago

Laboratoire Leprince-Ringuet, CNRS/IN2P3, Ecole Polytechnique, Institut Polytechnique de Paris, Palaiseau, France
F. Beaudette, A. Buchot Perraguin, P. Busson, A. Cappati, C. Charlot, M. Chiusi, F. Damas, O. Davignon, A. De Wit, I.T. Ehle, B.A. Fontana Santos Alves, S. Ghosh, A. Gilbert, R. Granier de Cassagnac, A. Hakimi, B. Harikrishnan, L. Kalipoliti, G. Liu, J. Motta, M. Nguyen, C. Ochando, R. Salerno, J.B. Sauvan, Y. Sirois, A. Tarabini, E. Vernazza, A. Zabi, A. Zghiche

Université de Strasbourg, CNRS, IPHC UMR 7178, Strasbourg, France
J.-L. Agram[23], J. Andrea, D. Apparu, D. Bloch, C. Bonnin, J.-M. Brom, E.C. Chabert, L. Charles, C. Collard, E. Dangelser, S. Falke, U. Goerlach, C. Grimault, L. Gross, C. Haas, R. Haeberle, M. Krauth, A.-C. Le Bihan, M. Meena, N. Ollivier-henry, O. Poncet, G. Saha, M.A. Sessini, P. Van Hove, P. Vaucelle

Institut de Physique des 2 Infinis de Lyon (IP2I), Villeurbanne, France
D. Amram, G. Baulieu, S. Beauceron, B. Blancon, A. Bonnevaux, G. Boudoul, L. Caponetto, N. Chanon, D. Contardo, P. Depasse, T. Dupasquier, H. El Mamouni, J. Fay, G. Galbit, S. Gascon, M. Gouzevitch, C. Greenberg, G. Grenier, B. Ille, E. Jourd‘huy, I.B. Laktineh, M. Lethuillier, M. Marchisone, L. Mirabito, B. Nodari, S. Perries, A. Purohit, E. Schibler, F. Schirra, M. Vander Donckt, P. Verdier, S. Viret, J. Xiao

Georgian Technical University, Tbilisi, Georgia
D. Chokheli, I. Lomidze, Z. Tsamalaidze[24]

RWTH Aachen University, I. Physikalisches Institut, Aachen, Germany
K.F. Adamowicz, V. Botta, S. Consuegra Rodríguez, C. Ebisch, L. Feld, W. Karpinski, K. Klein, M. Lipinski, D. Louis, D. Meuser, P. Nattland, V. Oppenländer, I. Özen, A. Pauls, D. Pérez Adán, N. Röwert, M. Teroerde, M. Wlochal

RWTH Aachen University, III. Physikalisches Institut A, Aachen, Germany
S. Diekmann, A. Dodonova, N. Eich, D. Eliseev, F. Engelke, J. Erdmann, M. Erdmann, P. Fackeldey, B. Fischer, T. Hebbeker, K. Hoepfner, F. Ivone, A. Jung, M.y. Lee, F. Mausolf, M. Merschmeyer, A. Meyer, S. Mukherjee, D. Noll, F. Nowotny, A. Pozdnyakov, Y. Rath, W. Redjeb, F. Rehm, H. Reithler, U. Sarkar, V. Sarkisovi, A. Schmidt, A. Sharma, J.L. Spah, A. Stein, F. Torres Da Silva De Araujo[25], S. Wiedenbeck, S. Zaleski

RWTH Aachen University, III. Physikalisches Institut B, Aachen, Germany
M.R. Beckers, C. Dziwok, G. Flügge, W. Haj Ahmad[26], N. Hoeflich, T. Kress, A. Nowack, O. Pooth, A. Stahl, W.G. Wyszkowska, T. Ziemons, A. Zotz

Deutsches Elektronen-Synchrotron, Hamburg, Germany

H. Aarup Petersen, A. Abel, A. Agah, D.M. Albrecht, M. Aldaya Martin, J. Alimena, S. Amoroso, Y. An, J. Bach, S. Baxter, M. Bayatmakou, H. Becerril Gonzalez, O. Behnke, A. Belvedere, S. Bhattacharya, F. Blekman[27], K. Borras[28], L. Braga Da Rosa, A. Campbell, A. Cardini, C. Cheng, L.X. Coll Saravia, F. Colombina, G. Correia Silva, M. De Silva, G. Eckerlin, D. Eckstein, L.I. Estevez Banos, O. Filatov, E. Gallo[27], Y. Gavrikov, A. Geiser, A. Giraldi, V. Guglielmi, M. Guthoff, A. Hinzmann, L. Jeppe, B. Kaech, M. Kasemann, C. Kleinwort, R. Kogler, M. Komm, D. Krücker, W. Lange, H. Lemmermann, D. Leyva Pernia, K. Lipka[29], W. Lohmann[30], F. Lorkowski, R. Mankel, H. Maser, I.-A. Melzer-Pellmann, M. Mendizabal Morentin, A.B. Meyer, G. Milella, K. Moral Figueroa, A. Mussgiller, L.P. Nair, A. Nürnberg, Y. Otarid, J. Park, E. Ranken, A. Raspereza, D. Rastorguev, O. Reichelt, B. Ribeiro Lopes, J. Rübenach, L. Rygaard, A. Saggio, M. Scham[31,32], S. Schnake[28], P. Schütze, C. Schwanenberger[27], D. Selivanova, K. Sharko, M. Shchedrolosiev, R.E. Sosa Ricardo, L. Sreelatha Pramod, D. Stafford, F. Vazzoler, A. Velyka, A. Ventura Barroso, R. Walsh, D. Wang, Q. Wang, Y. Wen, K. Wichmann, L. Wiens[28], C. Wissing, Y. Yang, S. Zakharov, A. Zimermmane Castro Santos, G. Yakopov, A. Zuber

University of Hamburg, Hamburg, Germany

A. Albrecht, S. Albrecht, M. Antonello, S. Bein, L. Benato, S. Bollweg, M. Bonanomi, P. Connor, K. El Morabit, Y. Fischer, E. Garutti, A. Grohsjean, J. Haller, H.R. Jabusch, G. Kasieczka, P. Keicher, R. Klanner, W. Korcari, T. Kramer, C.c. Kuo, V. Kutzner, F. Labe, J. Lange, A. Lobanov, S. Martens, C. Matthies, L. Moureaux, M. Mrowietz, A. Nigamova, Y. Nissan, A. Paasch, K.J. Pena Rodriguez, T. Quadfasel, B. Raciti, M. Rieger, D. Savoiu, J. Schaarschmidt, J. Schindler, P. Schleper, M. Schröder, J. Schwandt, M. Sommerhalder, H. Stadie, G. Steinbrück, A. Tews, J. Wellhausen, M. Wolf

Karlsruher Institut fuer Technologie, Karlsruhe, Germany

L. E. Ardila-Perez, M. Balzer, T. Barvich, B. Berger, S. Brommer, M. Burkart, E. Butz, M. Caselle, T. Chwalek, A. Dierlamm, A. Droll, U. Elicabuk, N. Faltermann, M. Fuchs, M. Giffels, A. Gottmann, F. Hartmann[33], R. Hofsaess, M. Horzela, U. Husemann, J. Kieseler, M. Klute, R. Koppenhöfer, K. Krämer, H.A. Krause, J.M. Lawhorn, M. Link, A. Lintuluoto, B. Maier, S. Maier, S. Mallows, T. Mehner, S. Mitra, M. Mormile, Th. Müller, M. Neukum, M. Oh, E. Pfeffer, M. Presilla, G. Quast, K. Rabbertz, B. Regnery, W. Rehm, N. Shadskiy, I. Shvetsov, H.J. Simonis, P. Steck, L. Stockmeier, M. Toms, B. Topko, N. Trevisani, R.F. Von Cube, M. Wassmer, S. Wieland, F. Wittig, R. Wolf, X. Zuo

Institute of Nuclear and Particle Physics (INPP), NCSR Demokritos, Aghia Paraskevi, Greece

G. Anagnostou, G. Daskalakis, I. Kazas, A. Kyriakis, D. Loukas, A. Papadopoulos[33], A. Stakia

National and Kapodistrian University of Athens, Athens, Greece

P. Kontaxakis, G. Melachroinos, Z. Painesis, A. Panagiotou, I. Papavergou, I. Paraskevas, N. Saoulidou, K. Theofilatos, E. Tziaferi, K. Vellidis, I. Zisopoulos

National Technical University of Athens, Athens, Greece

G. Bakas, T. Chatzistavrou, G. Karapostoli, K. Kousouris, I. Papakrivopoulos, E. Siamarkou, G. Tsipolitis, A. Zacharopoulou

University of Ioánnina, Ioánnina, Greece

K. Adamidis, I. Bestintzanos, I. Evangelou, C. Foudas, C. Kamtsikis, P. Katsoulis, P. Kokkas, P.G. Kosmoglou Kioseoglou, N. Manthos, I. Papadopoulos, J. Strologas

HUN-REN Wigner Research Centre for Physics, Budapest, Hungary

T. Balazs, M. Bartók[34], C. Hajdu, D. Horvath[35,36], K. Márton, A.J. Rádl[37], F. Sikler, V. Veszpremi

MTA-ELTE Lendület CMS Particle and Nuclear Physics Group, Eötvös Loránd University, Budapest, Hungary

M. Csanád, K. Farkas, A. Fehérkuti[38], M.M.A. Gadallah[39], Á. Kadlecsik, P. Major, K. Mandal, G. Pásztor, G.I. Veres

Faculty of Informatics, University of Debrecen, Debrecen, Hungary

L. Olah, P. Raics, B. Ujvari

HUN-REN ATOMKI - Institute of Nuclear Research, Debrecen, Hungary

G. Bencze, S. Czellar, J. Molnar, Z. Szillasi

Karoly Robert Campus, MATE Institute of Technology, Gyongyos, Hungary

T. Csorgo[38], F. Nemes[38], T. Novak

Panjab University, Chandigarh, India

J. Babbar, S. Bansal, S.B. Beri, V. Bhatnagar, G. Chaudhary, S. Chauhan, N. Dhingra[40], A. Kaur, A. Kaur, H. Kaur, M. Kaur, S. Kumar, K. Sandeep, T. Sheokand, J.B. Singh, A. Singla

University of Delhi, Delhi, India

A. Ahmed, A. Bhardwaj, A. Chhetri, B.C. Choudhary, C. Jain, A. Kumar, A. Kumar, M. Naimuddin, K. Ranjan, S. Saumya, M. Sharma, K. Tiwari

Saha Institute of Nuclear Physics, HBNI, Kolkata, India

S. Baradia, S. Barman[41], S. Bhattacharya, S. Das Gupta, S. Dutta, S. Dutta, S. Sarkar

Indian Institute of Technology Madras, Madras, India

M.M. Ameen, P.K. Behera, S.C. Behera, S. Chatterjee, T. Chembakan, G. Dash, A. Dattamunsi, P. Jana, P. Kalbhor, S. Kamble, J.R. Komaragiri[42], D. Kumar[42], P.R. Pujahari, A. Sharma, A.K. Sikdar, R.K. Singh, P. Verma, S. Verma, A. Vijay, D.S. Yadav

Tata Institute of Fundamental Research-A, Mumbai, India

S. Dugad, M. Kumar, G.B. Mohanty, M. Shelake, P. Suryadevara

Tata Institute of Fundamental Research-B, Mumbai, India

A. Bala, S. Banerjee, R.M. Chatterjee, R.K. Dewanjee[43], M. Guchait, Sh. Jain, A. Jaiswal, S. Kumar, G. Majumder, K. Mazumdar, S. Parolia, A. Thachayath

National Institute of Science Education and Research, An OCC of Homi Bhabha National Institute, Bhubaneswar, Odisha, India

B. Gauda[44], S. Bahinipati[44], A. Das, C. Kar, R. Kumar Agrawal, D. Maity[45], P. Mal, T. Mishra, V.K. Muraleedharan Nair Bindhu[45], K. Naskar[45], A. Nayak[45], S. Nayak, K. Pal, D.K. Pattanaik, S. Pradhan, P. Sadangi, S. Sahu, D.P. Satapathy, S. Shuchi, S.K. Swain, S. Varghese[45], D. Vats[45]

Indian Institute of Science Education and Research (IISER), Pune, India

S. Acharya[46], A. Alpana, S. Dube, B. Gomber[46], P. Hazarika, B. Kansal, A. Laha, B. Sahu[46], S. Sharma, K.Y. Vaish

Isfahan University of Technology, Isfahan, Iran

H. Bakhshiansohi[47], A. Jafari[48], M. Zeinali[49]

Institute for Research in Fundamental Sciences (IPM), Tehran, Iran

S. Bashiri, S. Chenarani[50], S.M. Etesami, Y. Hosseini, M. Khakzad, E. Khazaie[51], M. Mohammadi Najafabadi, S. Tizchang[52]

University College Dublin, Dublin, Ireland

M. Grunewald

INFN Sezione di Bari[a], Università di Bari[b], Politecnico di Bari[c], Bari, Italy

M. Abbrescia[a,b], R. Aly[a,c,,18], G. Ciani[a], A. Colaleo[a,b], D. Creanza[a,c], B. D'Anzi[a,b], N. De Filippis[a,c], M. De Palma[a,b], G. De Robertis[a], A. Di Florio[a,c], W. Elmetenawee[a,b,,18], L. Fiore[a], G. Iaselli[a,c], F. Loddo[a], M. Louka[a,b], G. Maggi[a,c], M. Maggi[a], I. Margjeka[a,b], S. Martiradonna[a], V. Mastrapasqua[a,b], A. Mongelli[a,b], S. My[a,b], S. Nuzzo[a,b], A. Pellecchia[a,b], A. Pompili[a,b], G. Pugliese[a,c], R. Radogna[a], G. Ramirez-Sanchez[a,c], D. Ramos[a], A. Ranieri[a], G. Sala[a], L. Silvestris[a], F.M. Simone[a,b], A. Stamerra[a], Ü. Sözbilir[a], D. Troiano[a], R. Venditti[a], P. Verwilligen[a], A. Zaza[a,b]

INFN Sezione di Bologna[a], Università di Bologna[b], Bologna, Italy

G. Abbiendi[a], C. Battilana[a,b], D. Bonacorsi[a,b], L. Borgonovi[a], P. Capiluppi[a,b], A. Castro[a,b], F.R. Cavallo[a], M. Cuffiani[a,b], G.M. Dallavalle[a], T. Diotalevi[a,b], F. Fabbri[a], A. Fanfani[a,b], D. Fasanella[a,b], P. Giacomelli[a], L. Giommi[a,b], C. Grandi[a], L. Guiducci[a,b], S. Lo Meo[a,,53], M. Lorusso[a,b], L. Lunerti[a,b], S. Marcellini[a], G. Masetti[a], F.L. Navarria[a,b], A. Perrotta[a], F. Primavera[a,b], S. Rossi Tisbeni[a,b], A.M. Rossi[a,b], T. Rovelli[a,b], G.P. Siroli[a,b]

INFN Sezione di Catania[a], Università di Catania[b], Catania, Italy

S. Albergo[a,b,,54], S. Costa[a,b,,54], A. Di Mattia[a], A. Lapertosa[a], R. Potenza[a,b], A. Tricomi[a,b,,54], C. Tuve[a,b]

INFN Sezione di Firenze[a], Università di Firenze[b], Firenze, Italy

J. Altork[a,b], P. Assiouras[a], G. Barbagli[a], G. Bardelli[a,b], M. Bartolini[a,b], M. Brianzi[a], B. Camaiani[a,b], A. Cassese[a], R. Ceccarelli[a], V. Ciulli[a,b], C. Civinini[a], R. D'Alessandro[a,b],

L. Damenti[a,b], E. Focardi[a,b], T. Kello[a], G. Latino[a,b], P. Lenzi[a,b], M. Lizzo[a], M. Meschini[a], S. Paoletti[a], A. Papanastassiou[a,b], R. Ciaranfi[a], G. Sguazzoni[a], L. Viliani[a]

INFN Laboratori Nazionali di Frascati, Frascati, Italy

L. Benussi, S. Bianco, S. Meola[55], D. Piccolo

INFN Sezione di Genova[a], Università di Genova[b], Genova, Italy

P. Chatagnon[a], F. Ferro[a], E. Robutti[a], S. Tosi[a,b]

INFN Sezione di Milano-Bicocca[a], Università di Milano-Bicocca[b], Milano, Italy

A. Benaglia[a], G. Boldrini[a,b], F. Brivio[a], F. Cetorelli[a], F. De Guio[a,b], M.E. Dinardo[a,b], P. Dini[a], S. Gennai[a], R. Gerosa[a,b], A. Ghezzi[a,b], P. Govoni[a,b], L. Guzzi[a], M.T. Lucchini[a,b], M. Malberti[a], S. Malvezzi[a], A. Massironi[a], D. Menasce[a], L. Moroni[a], M. Paganoni[a,b], S. Palluotto[a,b], D. Pedrini[a], B.S. Pinolini[a], G. Pizzati[a,b], S. Ragazzi[a,b], T. Tabarelli de Fatis[a,b]

INFN Sezione di Napoli[a], Università di Napoli 'Federico II'[b], Napoli, Italy, Università della Basilicata[c], Potenza, Italy, Scuola Superiore Meridionale (SSM)[d], Napoli, Italy

S. Buontempo[a], A. Cagnotta[a,b], F. Carnevali[a,b], N. Cavallo[a,c], F. Fabozzi[a,c], A.O.M. Iorio[a,b], L. Lista[a,b,,56], P. Paolucci[a,,33], B. Rossi[a], C. Sciacca[a,b]

INFN Sezione di Padova[a], Università di Padova[b], Padova, Italy, Universita degli Studi di Cagliari[c], Cagliari, Italy

R. Ardino[a], P. Azzi[a], N. Bacchetta[a,,57], D. Bisello[a,b], P. Bortignon[a], G. Bortolato[a,b], A. Bragagnolo[a,b], A.C.M. Bulla[a], R. Carlin[a,b], P. Checchia[a], T. Dorigo[a,,58], U. Gasparini[a,b], F. Gonella[a], A. Gozzelino[a], E. Lusiani[a], M. Margoni[a,b], F. Marini[a], A.T. Meneguzzo[a,b], M. Migliorini[a,b], J. Pazzini[a,b], P. Ronchese[a,b], R. Rossin[a,b], G. Strong[a], M. Tosi[a,b], A. Triossi[a,b], S. Ventura[a], M. Zanetti[a,b], P. Zotto[a,b], A. Zucchetta[a,b], G. Zumerle[a,b]

INFN Sezione di Pavia[a], Università di Pavia[b], Pavia, Italy

S. Abu Zeid[a,,59], C. Aimè[a,b], A. Braghieri[a], S. Calzaferri[a], D. Fiorina[a], L. Gaioni[a], M. Manghisoni[a], P. Montagna[a,b], L. Ratti[a], V. Re[a], C. Riccardi[a,b], E. Riceputi[a], P. Salvini[a], G. Traversi[a], I. Vai[a,b], P. Vitulo[a,b]

INFN Sezione di Perugia[a], Università di Perugia[b], Perugia, Italy

S. Ajmal[a,b], K. Aouadj[a], M.E. Ascioti[a,b], G. Baldinelli[a], F. Bianchi[a], G.M. Bilei[a], S. Bizzaglia[a], M. Bizzarri[a,b], W.D. Buitrago Ceballos[a], M. Caprai[a], C. Carrivale[a,b], B. Checcucci[a], D. Ciangottini[a,b], T. Croci[a], L. Della Penna[a,b], L. Fanò[a,b], L. Farnesini[a], A. Fondacci[a], M. Ionica[a], M. Magherini[a,b], V. Mariani[a,b], M. Menichelli[a], A. Morozzi[a,b], F. Moscatelli[a,,60], D. Passeri[a,b], P. Placidi[a,b], A. Rossi[a,b], A. Santocchia[a,b], D. Spiga[a], L. Storchi[a], T. Tedeschi[a,b], C. Turrioni[a]

INFN Sezione di Pisa[a], Università di Pisa[b], Scuola Normale Superiore di Pisa[c], Pisa, Italy, Università di Siena[d], Siena, Italy

C.A. Alexe[a,c], P. Asenov[a,b], P. Azzurri[a], G. Bagliesi[a], G. Balestri[a], A. Basti[a,b], R. Beccherle[a], D. Benvenuti[a], R. Bhattacharya[a], L. Bianchini[a,b], S. Bianucci[a], M. Bitossi[a], T. Boccali[a], L. Borrello[a], F. Bosi[a], E. Bossini[a], D. Bruschini[a,c], R. Castaldi[a], F. Cattafesta[a,c], M. Ceccanti[a], M.A. Ciocci[a,b], M. Cipriani[a,b], V. D'Amante[a,d], R. Dell'Orso[a], S. Donato[a],

R. Forti[a,b], A. Giassi[a], F. Ligabue[a,c], G. Magazzu[a], P. Mammini[a], M. Massa[a], D. Matos Figueiredo[a], E. Mazzoni[a], A. Messineo[a,b], A. Moggi[a], M. Musich[a,b,,61], F. Palla[a], F. Palmonari[a], A. Profeti[a], P. Prosperi[a], F. Raffaelli[a], M. Riggirello[a,c], A. Rizzi[a,b], G. Rolandi[a,c], S. Roy Chowdhury[a], T. Sarkar[a], A. Scribano[a], P. Spagnolo[a], F. Tenchini[a,b], R. Tenchini[a], G. Tonelli[a,b], N. Turini[a,d], F. Vaselli[a,c], A. Venturi[a], P.G. Verdini[a]

INFN Sezione di Roma[a], Sapienza Università di Roma[b], Roma, Italy

C. Baldenegro Barrera[a,b], P. Barria[a], C. Basile[a,b], M. Campana[a,b], F. Cavallari[a], L. Cunqueiro Mendez[a,b], D. Del Re[a,b], E. Di Marco[a], M. Diemoz[a], F. Errico[a,b], E. Longo[a,b], P. Meridiani[a], J. Mijuskovic[a,b], G. Organtini[a,b], F. Pandolfi[a], R. Paramatti[a,b], C. Quaranta[a,b], S. Rahatlou[a,b], C. Rovelli[a], F. Santanastasio[a,b], L. Soffi[a]

INFN Sezione di Torino[a], Università di Torino[b], Torino, Italy, Università del Piemonte Orientale[c], Novara, Italy

N. Amapane[a,b], R. Arcidiacono[a,c], S. Argiro[a,b], M. Arneodo[a,c], N. Bartosik[a], F. Bashir[a,b], R. Bellan[a,b], A. Bellora[a,b], C. Biino[a], C. Borca[a,b], N. Cartiglia[a], S. Coli[a], M. Costa[a,b], R. Covarelli[a,b], N. Demaria[a], L. Finco[a], S. Garrafa Botta[a], M. Grippo[a,b], B. Kiani[a,b], F. Legger[a], F. Luongo[a,b], C. Mariotti[a], L. Markovic[a,b], S. Maselli[a], A. Mecca[a,b], E. Migliore[a,b], M. Monteno[a], R. Mulargia[a], M.M. Obertino[a,b], G. Ortona[a], L. Pacher[a,b], N. Pastrone[a], M. Pelliccioni[a], F. Rotondo[a], M. Ruspa[a,c], F. Siviero[a,b], V. Sola[a,b], A. Solano[a,b], A. Staiano[a], C. Tarricone[a,b], D. Trocino[a], G. Umoret[a,b], E. Vlasov[a,b], R. White[a,b]

INFN Sezione di Trieste[a], Università di Trieste[b], Trieste, Italy

S. Belforte[a], V. Candelise[a,b], M. Casarsa[a], F. Cossutti[a], K. De Leo[a], G. Della Ricca[a,b]

Kyungpook National University, Daegu, Korea

S. Dogra, J. Hong, C. Huh, B. Kim, D.H. Kim, J. Kim, H. Lee, S.W. Lee, C.S. Moon, Y.D. Oh, M.S. Ryu, S. Sekmen, Y.C. Yang

Department of Mathematics and Physics - GWNU, Gangneung, Korea

M.S. Kim

Chonnam National University, Institute for Universe and Elementary Particles, Kwangju, Korea

G. Bak, P. Gwak, H. Kim, D.H. Moon

Hanyang University, Seoul, Korea

E. Asilar, J. Choi[62], D. Kim, T.J. Kim, J.A. Merlin

Korea University, Seoul, Korea

S. Choi, S. Han, B. Hong, K. Lee, K.S. Lee, S. Lee, J. Park, S.K. Park, J. Yoo

Kyung Hee University, Department of Physics, Seoul, Korea

J. Goh, S. Yang

Sejong University, Seoul, Korea

H. S. Kim, Y. Kim, S. Lee

Seoul National University, Seoul, Korea
J. Almond, J.H. Bhyun, J. Choi, W. Jun, J. Kim, S. Ko, H. Kwon, H. Lee, J. Lee, J. Lee, B.H. Oh, S.B. Oh, H. Seo, U.K. Yang, I. Yoon

University of Seoul, Seoul, Korea
W. Jang, D.Y. Kang, Y. Kang, S. Kim, B. Ko, J.S.H. Lee, Y. Lee, I.C. Park, Y. Roh, I.J. Watson

Yonsei University, Department of Physics, Seoul, Korea
S. Ha, H.D. Yoo

Sungkyunkwan University, Suwon, Korea
M. Choi, M.R. Kim, H. Lee, Y. Lee, I. Yu

College of Engineering and Technology, American University of the Middle East (AUM), Dasman, Kuwait
T. Beyrouthy

Riga Technical University, Riga, Latvia
K. Dreimanis, A. Gaile, G. Pikurs, A. Potrebko, M. Seidel

University of Latvia (LU), Riga, Latvia
N.R. Strautnieks

Vilnius University, Vilnius, Lithuania
M. Ambrozas, A. Juodagalvis, A. Rinkevicius, V. Tamosiunas, G. Tamulaitis

National Centre for Particle Physics, Universiti Malaya, Kuala Lumpur, Malaysia
N. Bin Norjoharuddeen, I. Yusuff[63], Z. Zolkapli

Universidad de Sonora (UNISON), Hermosillo, Mexico
J.F. Benitez, A. Castaneda Hernandez, H.A. Encinas Acosta, L.G. Gallegos Maríñez, M. León Coello, J.A. Murillo Quijada, A. Sehrawat, L. Valencia Palomo

Centro de Investigacion y de Estudios Avanzados del IPN, Mexico City, Mexico
G. Ayala, H. Castilla-Valdez, H. Crotte Ledesma, E. De La Cruz-Burelo, I. Heredia-De La Cruz[64], R. Lopez-Fernandez, C.A. Mondragon Herrera, A. Sánchez Hernández

Universidad Iberoamericana, Mexico City, Mexico
C. Oropeza Barrera, M. Ramírez García

Benemerita Universidad Autonoma de Puebla, Puebla, Mexico
I. Bautista, I. Pedraza, H.A. Salazar Ibarguen, C. Uribe Estrada

University of Montenegro, Podgorica, Montenegro
I. Bubanja, N. Raicevic

University of Canterbury, Christchurch, New Zealand
P.H. Butler

National Centre for Physics, Quaid-I-Azam University, Islamabad, Pakistan
A. Ahmad, M.I. Asghar, A. Awais, M.I.M. Awan, H.R. Hoorani, W.A. Khan, S. Muhammad, I. Sohail

AGH University of Krakow, Faculty of Computer Science, Electronics and Telecommunications, Krakow, Poland
V. Avati, L. Grzanka, M. Malawski

National Centre for Nuclear Research, Swierk, Poland
H. Bialkowska, M. Bluj, B. Boimska, M. Górski, M. Kazana, M. Szleper, P. Zalewski

Institute of Experimental Physics, Faculty of Physics, University of Warsaw, Warsaw, Poland
K. Bunkowski, K. Doroba, A. Kalinowski, M. Konecki, J. Krolikowski, A. Muhammad

Warsaw University of Technology, Warsaw, Poland
K. Pozniak, W. Zabolotny

Laboratório de Instrumentação e Física Experimental de Partículas, Lisboa, Portugal
M. Araujo, D. Bastos, C. Beirão Da Cruz E Silva, A. Boletti, M. Bozzo, T. Camporesi, G. Da Molin, P. Faccioli, M. Gallinaro, J. Hollar, N. Leonardo, G.B. Marozzo, T. Niknejad, A. Petrilli, M. Pisano, J. Seixas, J. Varela, J.W. Wulff

Faculty of Physics, University of Belgrade, Belgrade, Serbia
P. Adzic, P. Milenovic

VINCA Institute of Nuclear Sciences, University of Belgrade, Belgrade, Serbia
M. Dordevic, J. Milosevic, V. Rekovic

Centro de Investigaciones Energéticas Medioambientales y Tecnológicas (CIEMAT), Madrid, Spain
M. Aguilar-Benitez, J. Alcaraz Maestre, Cristina F. Bedoya, Oliver M. Carretero, M. Cepeda, M. Cerrada, N. Colino, B. De La Cruz, A. Delgado Peris, A. Escalante Del Valle, D. Fernández Del Val, J.P. Fernández Ramos, J. Flix, M.C. Fouz, O. Gonzalez Lopez, S. Goy Lopez, J.M. Hernandez, M.I. Josa, D. Moran, C. M. Morcillo Perez, Á. Navarro Tobar, C. Perez Dengra, A. Pérez-Calero Yzquierdo, J. Puerta Pelayo, I. Redondo, D.D. Redondo Ferrero, L. Romero, S. Sánchez Navas, L. Urda Gómez, J. Vazquez Escobar, C. Willmott

Universidad Autónoma de Madrid, Madrid, Spain
J.F. de Trocóniz

Universidad de Oviedo, Instituto Universitario de Ciencias y Tecnologías Espaciales de Asturias (ICTEA), Oviedo, Spain
B. Alvarez Gonzalez, J. Cuevas, J. Fernandez Menendez, S. Folgueras, I. Gonzalez Caballero, J.R. González Fernández, P. Leguina, E. Palencia Cortezon, C. Ramón Álvarez, V. Rodríguez Bouza, A. Soto Rodríguez, A. Trapote, C. Vico Villalba, P. Vischia

Instituto de Física de Cantabria (IFCA), CSIC-Universidad de Cantabria, Santander, Spain

S. Bhowmik, S. Blanco Fernández, J.A. Brochero Cifuentes, I.J. Cabrillo, A. Calderon, J. Duarte Campderros, M. Fernandez, G. Gomez, J. Gonzalez Sanchez, R.W. Jaramillo Echeverria, C. Lasaosa García, R. Lopez Ruiz, A. Lopez Virto, C. Martinez Rivero, P. Martinez Ruiz del Arbol, F. Matorras, P. Matorras Cuevas, D. Moya, E. Navarrete Ramos, J. Piedra Gomez, C. Quintana San Emeterio, L. Scodellaro, I. Vila, J.M. Vizan Garcia

University of Colombo, Colombo, Sri Lanka

M.K. Jayananda, B. Kailasapathy[65], D.U.J. Sonnadara, D.D.C. Wickramarathna

University of Ruhuna, Department of Physics, Matara, Sri Lanka

W.G.D. Dharmaratna[66], K. Liyanage, N. Perera, N. Wickramage

CERN, European Organization for Nuclear Research, Geneva, Switzerland

D. Abbaneo, M. Abbas, I. Ahmed, E. Albert, B. Allongue, C. Amendola, D. Andreou, E. Auffray, G. Auzinger, J. Baechler, L. Balocchi, D. Barney, A. Bermúdez Martínez, M. Bianco, B. Bilin, A.A. Bin Anuar, L. Bistoni, G. Blanchot, A. Bocci, C. Botta, F. Boyer, E. Brondolin, C. Caillol, A. Caratelli, R. Carnesecchi, D. Ceresa, G. Cerminara, N. Chernyavskaya, J. Christiansen, E. Christidou, P. Cianchetta[67], D. d'Enterria, A. Dabrowski, J. Daguin, A. David, A. De Roeck, M.M. Defranchis, M. Deile, A. Diamantis, M. Dobson, A. Dwivedi, A. Eugeni, L. Forthomme, N. Frank, G. Franzoni, T. French, W. Funk, S. Giani, D. Gigi, K. Gill, F. Glege, D. Golyzniak, L. Gouskos, J. Grundy, B. Grygiel, M. Haranko, M. Hassouna, J. Hegeman, B. Huber, V. Innocente, T. James, P. Janot, O. Kaluzinska, K. Kloukinas, L.J. Kottelat, M.I. Kovács, R. Kristic, D. Langedijk, S. Laurila, P. Lecoq, M. Ledoux, P. Lenoir, E. Leutgeb, R. Loos, J. Lopes, C. Lourenço, M. Magherini, L. Malgeri, M. Mannelli, A. Marchioro, A.C. Marini[68,69], M. Matthewman, A. Mehta, F. Meijers, S. Mersi, E. Meschi, S. Michelis, V. Milosevic, F. Monti, F. Moortgat, M. Mulders, S. Musaed, M. Najafabadi[70], I. Neutelings, L. Olantera, A. Onnela, S. Orfanelli, T. Pakulski, B. Paluch, F. Pantaleo, A. Papadopoulos, F. Perea Albela, A. Perez, F. Perez Gomez, J.F. Pernot, P. Petagna, G. Petrucciani, A. Pfeiffer, Q. Piazza, M. Pierini, D. Piparo, H. Qu, D. Rabady, P. Rose, M. Rovere, H. Sakulin, S. Scarfi, C. Schwick, M. Selvaggi, A. Sharma, K. Shchelina, N. Siegrist, P. Silva, P. Sphicas[71], A.G. Stahl Leiton, A. Steen, C. Stile, A. Sultan[70], S. Summers, P. Szydlik, D. Treille, P. Tropea, J. Troska, A. Tsirou, F. Vasey, P. Vichoudis, R. Vrancianu, D. Walter, J. Wanczyk[72], J. Wang, S. Wlodarczyk, S. Wuchterl, K. Wyllie, P. Zehetner, P. Zejdl, W.D. Zeuner, G. Zevi Della Porta, A. Zimmermann, A. Zografos

PSI Center for Neutron and Muon Sciences, Villigen, Switzerland

W. Bertl[†], T. Bevilacqua[73], L. Caminada[73], A. Ebrahimi, W. Erdmann, R. Horisberger, Q. Ingram, H.C. Kaestli, D. Kotlinski, C. Lange, B. Meier, M. Missiroli[73], L. Noehte[73], N. Pique, T. Rohe, A. Samalan, S. Streuli

ETH Zurich - Institute for Particle Physics and Astrophysics (IPA), Zurich, Switzerland

T.K. Aarrestad, K. Androsov[72], M. Backhaus, R. Becker, G. Bonomelli, A. Calandri, C. Cazzaniga, D.R. Da Silva Di Calafiori, K. Datta, A. De Cosa, G. Dissertori, M. Dittmar, M. Donegà, F. Eble, M. Galli, K. Gedia, F. Glessgen, C. Grab, N. Härringer, T.G. Harte, D. Hits, W. Lustermann, A.-M. Lyon, R.A. Manzoni, M. Marchegiani, L. Marchese,

C. Martin Perez, A. Mascellani[72], F. Nessi-Tedaldi, F. Pauss, V. Perovic, S. Pigazzini, C. Reissel, T. Reitenspiess, B. Ristic, F. Riti, S. Rohletter, P.M. Sander, R. Seidita, J. Soerensen, J. Steggemann[72], D. Valsecchi, R. Wallny

Universität Zürich, Zurich, Switzerland

C. Amsler[74], P. Bärtschi, F. Bilandzija, K. Bösiger, M.F. Canelli, G. Celotto, K. Cormier, N. Gadola, J.K. Heikkilä, W. Jin, A. Jofrehei, B. Kilminster, T.H. Kwok, S. Leontsinis, S.P. Liechti, V. Lukashenko, A. Macchiolo, R. Maier, P. Meiring, F. Meng, U. Molinatti, A. Reimers, P. Robmann, S. Sanchez Cruz, M. Senger, E. Shokr, F. Stäger, Y. Takahashi, R. Tramontano, D. Wolf

National Central University, Chung-Li, Taiwan

C. Adloff[75], D. Bhowmik, C.M. Kuo, W. Lin, P.K. Rout, P.C. Tiwari[42], S.S. Yu

National Taiwan University (NTU), Taipei, Taiwan

L. Ceard, Y. Chao, K.F. Chen, P.H. Chen, P.s. Chen, Z.g. Chen, A. De Iorio, W.-S. Hou, T.h. Hsu, Y.w. Kao, S. Karmakar, R. Khurana, G. Kole, Y.y. Li, R.-S. Lu, E. Paganis, X.f. Su, J. Thomas-Wilsker, L.s. Tsai, H.y. Wu, E. Yazgan

High Energy Physics Research Unit, Department of Physics, Faculty of Science, Chulalongkorn University, Bangkok, Thailand

C. Asawatangtrakuldee, N. Srimanobhas, V. Wachirapusitanand

Çukurova University, Physics Department, Science and Art Faculty, Adana, Turkey

D. Agyel, F. Boran, Z.S. Demiroglu, F. Dolek, I. Dumanoglu[76], E. Eskut, Y. Guler[77], E. Gurpinar Guler[77], C. Isik, O. Kara, A. Kayis Topaksu, U. Kiminsu, G. Onengut, K. Ozdemir[78], A. Polatoz, B. Tali[79], U.G. Tok, S. Turkcapar, E. Uslan, I.S. Zorbakir

Middle East Technical University, Physics Department, Ankara, Turkey

G. Sokmen, M. Yalvac[80]

Bogazici University, Istanbul, Turkey

B. Akgun, I.O. Atakisi, E. Gülmez, M. Kaya[81], O. Kaya[82], S. Tekten[83]

Istanbul Technical University, Istanbul, Turkey

A. Cakir, K. Cankocak[76,84], G.G. Dincer[76], Y. Komurcu, S. Sen[85]

Istanbul University, Istanbul, Turkey

O. Aydilek[26], S. Cerci[79], V. Epshteyn, B. Hacisahinoglu, I. Hos[86], B. Kaynak, S. Ozkorucuklu, O. Potok, H. Sert, C. Simsek, C. Zorbilmez

Yildiz Technical University, Istanbul, Turkey

B. Isildak[87], D. Sunar Cerci[79]

Institute for Scintillation Materials of National Academy of Science of Ukraine, Kharkiv, Ukraine

A. Boyaryntsev, B. Grynyov

National Science Centre, Kharkiv Institute of Physics and Technology, Kharkiv, Ukraine
L. Levchuk

University of Bristol, Bristol, United Kingdom
D. Anthony, J.J. Brooke, A. Bundock, F. Bury, E. Clement, D. Cussans, H. Flacher, M. Glowacki, J. Goldstein, H.F. Heath, M.-L. Holmberg, L. Kreczko, S. Paramesvaran, L. Robertshaw, M.S. Sanjrani[47], S. Seif El Nasr-Storey, V.J. Smith, N. Stylianou[88], K. Walkingshaw Pass

Rutherford Appleton Laboratory, Didcot, United Kingdom
A.H. Ball, K.W. Bell, A. Belyaev[89], C. Brew, R.M. Brown, D.J.A. Cockerill, C. Cooke, K.V. Ellis, K. Harder, S. Harper, J. Linacre, K. Manolopoulos, D.M. Newbold, E. Olaiya, D. Petyt, T. Reis, A.R. Sahasransu, G. Salvi, T. Schuh, C.H. Shepherd-Themistocleous, I.R. Tomalin, T. Williams

Imperial College, London, United Kingdom
R. Bainbridge, P. Bloch, C.E. Brown, O. Buchmuller, V. Cacchio, C.A. Carrillo Montoya, G.S. Chahal[90], D. Colling, J.S. Dancu, I. Das, P. Dauncey, G. Davies, J. Davies, M. Della Negra, S. Fayer, G. Fedi, G. Hall, M.H. Hassanshahi, A. Howard, G. Iles, M. Knight, J. Langford, J. León Holgado, L. Lyons, A.-M. Magnan, S. Malik, A. Mastronikolis, M. Mieskolainen, J. Nash[91], D. Parker, M. Pesaresi, P.B. Pradeep, B.C. Radburn-Smith, A. Richards, A. Rose, K. Savva, C. Seez, R. Shukla, A. Tapper, K. Uchida, G.P. Uttley, L.H. Vage, T. Virdee[33], M. Vojinovic, N. Wardle, D. Winterbottom

Brunel University, Uxbridge, United Kingdom
K. Coldham, J.E. Cole, A. Khan, P. Kyberd, I.D. Reid

Baylor University, Waco, Texas, U.S.A.
S. Abdullin, A. Brinkerhoff, B. Caraway, E. Collins, J. Dittmann, K. Hatakeyama, J. Hiltbrand, B. McMaster, J. Samudio, S. Sawant, C. Sutantawibul, J. Wilson

Catholic University of America, Washington, DC, U.S.A.
R. Bartek, A. Dominguez, C. Huerta Escamilla, R. Khatri, S. Raj, A.E. Simsek, R. Uniyal, A.M. Vargas Hernandez

The University of Alabama, Tuscaloosa, Alabama, U.S.A.
B. Bam, R. Chudasama, S.I. Cooper, C. Crovella, S.V. Gleyzer, E. Pearson, C.U. Perez, P. Rumerio[92], E. Usai, R. Yi

Boston University, Boston, Massachusetts, U.S.A.
A. Akpinar, D. Arcaro, S. Cholak, C. Cosby, G. De Castro, Z. Demiragli, C. Erice, C. Fangmeier, C. Fernandez Madrazo, E. Fontanesi, J. Fulcher, D. Gastler, F. Golf, S. Jeon, G. Linney, A. Madorsky, I. Reed, J. Rohlf, K. Salyer, D. Sperka, D. Spitzbart, I. Suarez, A. Tsatsos, S. Yuan, A.G. Zecchinelli

Brown University, Providence, Rhode Island, U.S.A.
Y. Acevedo, G. Barone, G. Benelli, X. Coubez[28], D. Cutts, S. Ellis, M. Hadley, U. Heintz, N. Hinton, J.M. Hogan[93], A. Honma, A. Korotkov, T. Kwon, G. Landsberg, K.T. Lau,

M. LeBlanc, D. Li, J. Luo, S. Mondal, M. Narain[†], N. Pervan, J. Roloff, T. Russell, S. Sagir[94], X. Shen, F. Simpson, E. Spencer, M. Stamenkovic, S. Sunnarborg, N. Venkatasubramanian, X. Yan, W. Zhang

University of California, Davis, Davis, California, U.S.A.
S. Abbott, B. Barton, J. Bonilla, C. Brainerd, R. Breedon, H. Cai, M. Calderon De La Barca Sanchez, E. Cannaert, M. Chertok, M. Citron, J. Conway, P.T. Cox, R. Erbacher, D. Hemer, F. Jensen, O. Kukral, G. Mocellin, M. Mulhearn, D. Pellett, J. Thomson, W. Wei, F. Zhang

University of California, Los Angeles, California, U.S.A.
M. Bachtis, R. Cousins, A. Datta, G. Flores Avila, J. Hauser, M. Ignatenko, M.A. Iqbal, T. Lam, E. Manca, A. Nunez Del Prado, D. Saltzberg, V. Valuev

University of California, Riverside, Riverside, California, U.S.A.
R. Clare, J.W. Gary, M. Gordon, G. Hanson, W. Si, S. Wimpenny[†]

University of California, San Diego, La Jolla, California, U.S.A.
A. Aportela, A. Arora, J.G. Branson, J. Chismar, S. Cittolin, S. Cooperstein, D. Diaz, J. Duarte, L. Giannini, Y. Gu, J. Guiang, R. Kansal, V. Krutelyov, R. Lee, J. Letts, M. Masciovecchio, F. Mokhtar, S. Mukherjee, M. Pieri, M. Quinnan, B.V. Sathia Narayanan, V. Sharma, M. Tadel, E. Vourliotis, F. Würthwein, Y. Xiang, A. Yagil

University of California, Santa Barbara - Department of Physics, Santa Barbara, California, U.S.A.
A. Barzdukas, L. Brennan, C. Campagnari, J. Incandela, J. Kim, S. Kyre, A.J. Li, P. Masterson, H. Mei, J. Richman, U. Sarica, R. Schmitz, F. Setti, J. Sheplock, D. Stuart, T.Á. Vámi, S. Wang

California Institute of Technology, Pasadena, California, U.S.A.
A. Bornheim, O. Cerri, A. Latorre, J. Mao, H.B. Newman, G. Reales Gutiérrez, M. Spiropulu, J.R. Vlimant, C. Wang, S. Xie, R.Y. Zhu

Carnegie Mellon University, Pittsburgh, Pennsylvania, U.S.A.
J. Alison, S. An, M.B. Andrews, P. Bryant, M. Cremonesi, V. Dutta, T. Ferguson, A. Harilal, A. Kallil Tharayil, C. Liu, T. Mudholkar, S. Murthy, P. Palit, K. Park, M. Paulini, A. Roberts, A. Sanchez, W. Terrill

University of Colorado Boulder, Boulder, Colorado, U.S.A.
J.P. Cumalat, W.T. Ford, A. Hart, A. Hassani, M. Herrmann, G. Karathanasis, N. Manganelli, J. Pearkes, A. Perloff, C. Savard, N. Schonbeck, K. Stenson, K.A. Ulmer, S.R. Wagner, N. Zipper, D. Zuolo

Cornell University, Ithaca, New York, U.S.A.
J. Alexander, S. Bright-Thonney, X. Chen, D.J. Cranshaw, A. Duquette, J. Fan, X. Fan, A. Filenius, J. Grassi, S. Hogan, P. Kotamnives, K. Krzyzanska, S. Lantz, J. Monroy, G. Niendorf,

M. Oshiro, J.R. Patterson, H. Postema, M. Reid, D. Riley, A. Ryd, S. Shikha, K. Smolenski, C. Strohman, J. Thom, H.A. Weber, B. Weiss, P. Wittich, Y. Wu, R. Zou

Fermi National Accelerator Laboratory, Batavia, Illinois, U.S.A.

M. Albrow, M. Alyari, O. Amram, G. Apollinari, A. Apresyan, L.A.T. Bauerdick, D. Berry, J. Berryhill, P.C. Bhat, K. Burkett, D. Butler, J.N. Butler, A. Canepa, G.B. Cerati, H.W.K. Cheung, F. Chlebana, G. Cummings, G. Derylo, J. Dickinson, I. Dutta, V.D. Elvira, Y. Feng, J. Freeman, A. Gandrakota, Z. Gecse, A. Ghosh, H. Gonzalez, L. Gray, D. Green, A. Grummer, S. Grünendahl, D. Guerrero, O. Gutsche, R.M. Harris, R. Heller, T.C. Herwig, J. Hirschauer, L. Horyn, B. Jayatilaka, S. Jindariani, M. Johnson, U. Joshi, P. Klabbers, T. Klijnsma, B. Klima, K.H.M. Kwok, S. Lammel, C. Lee, D. Lincoln, R. Lipton, T. Liu, S. Los, C. Madrid, K. Maeshima, C. Mantilla, D. Mason, P. McBride, P. Merkel, S. Mrenna, S. Nahn, J. Ngadiuba, D. Noonan, V. Papadimitriou, N. Pastika, K. Pedro, C. Pena[95], F. Ravera, A. Reinsvold Hall[96], L. Ristori, R. Rivera, E. Sexton-Kennedy, N. Smith, A. Soha, L. Spiegel, S. Stoynev, J. Strait, L. Taylor, S. Tkaczyk, N.V. Tran, L. Uplegger, E.W. Vaandering, E. Voirin, A. Whitbeck, I. Zoi

University of Florida, Gainesville, Florida, U.S.A.

C. Aruta, P. Avery, D. Bourilkov, L. Cadamuro, P. Chang, V. Cherepanov, R.D. Field, E. Koenig, M. Kolosova, J. Konigsberg, A. Korytov, K. Matchev, N. Menendez, G. Mitselmakher, K. Mohrman, A. Muthirakalayil Madhu, N. Rawal, D. Rosenzweig, S. Rosenzweig, J. Wang

Florida State University, Tallahassee, Florida, U.S.A.

T. Adams, A. Al Kadhim, A. Askew, S. Bower, R. Habibullah, V. Hagopian, R. Hashmi, R.S. Kim, S. Kim, T. Kolberg, G. Martinez, H. Prosper, P.R. Prova, M. Wulansatiti, R. Yohay, J. Zhang

Florida Institute of Technology, Melbourne, Florida, U.S.A.

B. Alsufyani, M.M. Baarmand, S. Butalla, S. Das, T. Elkafrawy[59], M. Hohlmann, R. Kumar Verma, M. Rahmani, E. Yanes

University of Illinois Chicago, Chicago, Illinois, U.S.A.

M.R. Adams, A. Baty, C. Bennett, R. Cavanaugh, R. Escobar Franco, A. Evdokimov, O. Evdokimov, C.E. Gerber, H. Gupta, M. Hawksworth, A. Hingrajiya, D.J. Hofman, J.h. Lee, D. S. Lemos, A.H. Merrit, C. Mills, S. Nanda, G. Oh, B. Ozek, D. Pilipovic, R. Pradhan, E. Prifti, T. Roy, S. Rudrabhatla, D. Shekar, N. Singh, A. Thielen, M.B. Tonjes, N. Varelas, M.A. Wadud, Z. Ye, J. Yoo

The University of Iowa, Iowa City, Iowa, U.S.A.

M. Alhusseini, D. Blend, K. Dilsiz[97], L. Emediato, G. Karaman, O.K. Köseyan, J.-P. Merlo, A. Mestvirishvili[98], J. Nachtman, O. Neogi, H. Ogul[99], Y. Onel, A. Penzo, C. Snyder, E. Tiras[100]

Johns Hopkins University, Baltimore, Maryland, U.S.A.

B. Blumenfeld, L. Corcodilos, J. Davis, A.V. Gritsan, L. Kang, S. Kyriacou, P. Maksimovic, M. Roguljic, J. Roskes, S. Sekhar, M.V. Srivastav, M. Swartz

The University of Kansas, Lawrence, Kansas, U.S.A.

A. Abreu, L.F. Alcerro Alcerro, J. Anguiano, S. Arteaga Escatel, P. Baringer, A. Bean, Z. Flowers, D. Grove, J. King, G. Krintiras, M. Lazarovits, C. Le Mahieu, J. Marquez, N. Minafra, M. Murray, M. Nickel, M. Pitt, S. Popescu[101], C. Rogan, C. Royon, R. Salvatico, S. Sanders, C. Smith, Q. Wang, G. Wilson

Kansas State University, Manhattan, Kansas, U.S.A.

B. Allmond, R. Gujju Gurunadha, A. Ivanov, K. Kaadze, A. Kalogeropoulos, Y. Maravin, J. Natoli, D. Roy, G. Sorrentino, R. Taylor

Lawrence Livermore National Laboratory, Livermore, California, U.S.A.

F. Rebassoo, D. Wright

University of Maryland, College Park, Maryland, U.S.A.

A. Baden, A. Belloni, J. Bistany-riebman, Y.M. Chen, S.C. Eno, N.J. Hadley, S. Jabeen, R.G. Kellogg, T. Koeth, B. Kronheim, Y. Lai, S. Lascio, A.C. Mignerey, S. Nabili, C. Palmer, C. Papageorgakis, M.M. Paranjpe, L. Wang

Massachusetts Institute of Technology, Cambridge, Massachusetts, U.S.A.

J. Bendavid, I.A. Cali, P.c. Chou, M. D'Alfonso, J. Eysermans, C. Freer, G. Gomez-Ceballos, M. Goncharov, G. Grosso, P. Harris, D. Hoang, D. Kovalskyi, J. Krupa, L. Lavezzo, Y.-J. Lee, K. Long, A. Novak, C. Paus, D. Rankin, C. Roland, G. Roland, S. Rothman, G.S.F. Stephans, Z. Wang, B. Wyslouch, T. J. Yang

University of Minnesota, Minneapolis, Minnesota, U.S.A.

B. Crossman, B.M. Joshi, C. Kapsiak, M. Krohn, D. Mahon, J. Mans, B. Marzocchi, S. Pandey, M. Revering, R. Rusack, R. Saradhy, N. Schroeder, N. Strobbe

University of Mississippi, Oxford, Mississippi, U.S.A.

L.M. Cremaldi

University of Nebraska-Lincoln, Lincoln, Nebraska, U.S.A.

K. Bloom, D.R. Claes, G. Haza, J. Hossain, C. Joo, I. Kravchenko, J.E. Siado, W. Tabb, A. Vagnerini, A. Wightman, F. Yan, D. Yu

State University of New York at Buffalo, Buffalo, New York, U.S.A.

H. Bandyopadhyay, L. Hay, H.w. Hsia, I. Iashvili, A. Kharchilava, M. Morris, D. Nguyen, S. Rappoccio, H. Rejeb Sfar, A. Williams, P. Young

Northeastern University, Boston, Massachusetts, U.S.A.

G. Alverson, E. Barberis, J. Dervan, Y. Haddad, Y. Han, A. Krishna, J. Li, M. Lu, G. Madigan, R. Mccarthy, D.M. Morse, V. Nguyen, T. Orimoto, A. Parker, L. Skinnari, E. Tsai, D. Wood

Northwestern University, Evanston, Illinois, U.S.A.

J. Bueghly, Z. Chen, S. Dittmer, K.A. Hahn, B. Lawrence-sanderson, Y. Liu, M. Mcginnis, Y. Miao, D.G. Monk, S. Nanampattu Mohammed Noorudhin, M.H. Schmitt, A. Taliercio, M. Velasco

University of Notre Dame, Notre Dame, Indiana, U.S.A.

G. Agarwal, R. Band, R. Bucci, S. Castells, A. Das, R. Goldouzian, M. Hildreth, K.W. Ho, K. Hurtado Anampa, T. Ivanov, C. Jessop, K. Lannon, J. Lawrence, N. Loukas, L. Lutton, J. Mariano, N. Marinelli, I. Mcalister, T. McCauley, C. Mcgrady, C. Moore, Y. Musienko[17], H. Nelson, M. Osherson, A. Piccinelli, R. Ruchti, A. Townsend, Y. Wan, M. Wayne, H. Yockey, M. Zarucki, L. Zygala

The Ohio State University, Columbus, Ohio, U.S.A.

A. Basnet, B. Bylsma, M. Carrigan, R. De Los Santos, L.S. Durkin, C. Hill, M. Joyce, M. Nunez Ornelas, K. Wei, B.L. Winer, B. R. Yates

Princeton University, Princeton, New Jersey, U.S.A.

F.M. Addesa, H. Bouchamaoui, P. Das, G. Dezoort, P. Elmer, A. Frankenthal, B. Greenberg, N. Haubrich, G. Kopp, S. Kwan, D. Lange, A. Loeliger, D. Marlow, I. Ojalvo, J. Olsen, A. Shevelev, D. Stickland, C. Tully

University of Puerto Rico, Mayaguez, Puerto Rico, U.S.A.

S. Malik, R. Sharma

Purdue University, West Lafayette, Indiana, U.S.A.

V.E. Barnes[†], S. Chandra, E. Colbert, B.R. Denos, A. Gu, L. Gutay, M. Huwiler, M. Jones, A.W. Jung, S. Karmarkar, I.G. Karslioglu, D. Kondratyev, M. Liu, G. Negro, N. Neumeister, G. Paspalaki, S. Piperov, N.R. Saha, V. Scheurer, J.F. Schulte, M. Stojanovic[102], A. K. Virdi, F. Wang, W. Xie, Y. Yao, Y. Zhong

Purdue University Northwest, Hammond, Indiana, U.S.A.

J. Dolen, N. Parashar, A. Pathak

Rice University, Houston, Texas, U.S.A.

D. Acosta, A. Agrawal, T. Carnahan, K.M. Ecklund, P.J. Fernández Manteca, S. Freed, P. Gardner, F.J.M. Geurts, W. Li, J. Lin, O. Miguel Colin, T. Nussbaum, B.P. Padley, R. Redjimi, J. Rotter, E. Yigitbasi, Y. Zhang

University of Rochester, Rochester, New York, U.S.A.

A. Bodek, P. de Barbaro[†], R. Demina, J.L. Dulemba, A. Garcia-Bellido, A. Herrera, O. Hindrichs, A. Khukhunaishvili, N. Parmar, P. Parygin[103], E. Popova[103], R. Taus

The Rockefeller University, New York, New York, U.S.A.

K. Goulianos

Rutgers, The State University of New Jersey, Piscataway, New Jersey, U.S.A.

B. Chiarito, J.P. Chou, S.V. Clark, D. Gadkari, Y. Gershtein, E. Halkiadakis, M. Heindl, C. Houghton, D. Jaroslawski, O. Karacheban[30], A. Kobert, S. Konstantinou, C. Kurup, I. Laflotte, A. Lath, R. Montalvo, K. Nash, J. Reichert, H. Routray, P. Saha, S. Salur, S. Schnetzer, S. Somalwar, R. Stone, S.A. Thayil, S. Thomas, J. Vora, H. Wang

University of Tennessee, Knoxville, Tennessee, U.S.A.

H. Acharya, D. Ally, A.G. Delannoy, S. Fiorendi, J. Harris, S. Higginbotham, T. Holmes, A.R. Kanuganti, N. Karunarathna, J. Lawless, L. Lee, E. Nibigira, B. Skipworth, S. Spanier

Texas A&M University, College Station, Texas, U.S.A.

D. Aebi, M. Ahmad, O. Bouhali[104], R. Eusebi, J. Gilmore, T. Huang, T. Kamon[105], H. Kim, S. Luo, R. Mueller, D. Overton, D. Rathjens, A. Safonov

Texas Tech University, Lubbock, Texas, U.S.A.

N. Akchurin, J. Damgov, N. Gogate, V. Hegde, A. Hussain, Y. Kazhykarim, K. Lamichhane, S.W. Lee, A. Mankel, T. Peltola, I. Volobouev

Vanderbilt University, Nashville, Tennessee, U.S.A.

E. Appelt, Y. Chen, P. D'Angelo, S. Greene, A. Gurrola, W. Johns, R. Kunnawalkam Elayavalli, A. Melo, F. Romeo, P. Sheldon, S. Tuo, J. Velkovska, J. Viinikainen

University of Virginia, Charlottesville, Virginia, U.S.A.

B. Cardwell, B. Cox, J. Hakala, R. Hirosky, A. Ledovskoy, C. Neu, C.E. Perez Lara

Wayne State University, Detroit, Michigan, U.S.A.

S. Bhattacharya, P.E. Karchin

University of Wisconsin - Madison, Madison, Wisconsin, U.S.A.

A. Aravind, S. Banerjee, K. Black, T. Bose, S. Dasu, I. De Bruyn, P. Everaerts, C. Galloni, H. He, M. Herndon, A. Herve, C.K. Koraka, A. Lanaro, R. Loveless, J. Madhusudanan Sreekala, A. Mallampalli, A. Mohammadi, S. Mondal, G. Parida, L. Pétré, D. Pinna, A. Savin, V. Shang, V. Sharma, W.H. Smith, D. Teague, H.F. Tsoi, W. Vetens, A. Warden

An institute or international laboratory covered by a cooperation agreement with CERN

S. Afanasiev, D. Budkouski, I. Golutvin, I. Gorbunov, V. Karjavine, V. Korenkov, A. Lanev, A. Malakhov, V. Matveev[17], V. Palichik, V. Perelygin, M. Savina, V. Shalaev, S. Shmatov, S. Shulha, V. Smirnov, O. Teryaev, N. Voytishin, B.S. Yuldashev[106], A. Zarubin, I. Zhizhin

An institute formerly covered by a cooperation agreement with CERN

V. Chekhovsky, V. Makarenko, G. Gavrilov, V. Golovtcov, Y. Ivanov, V. Kim[17], P. Levchenko[107], V. Murzin, V. Oreshkin, D. Sosnov, V. Sulimov, L. Uvarov, A. Vorobyev[†], Yu. Andreev, A. Dermenev, S. Gninenko, N. Golubev, A. Karneyeu, D. Kirpichnikov, M. Kirsanov, N. Krasnikov, I. Tlisova, A. Toropin, T. Aushev, V. Gavrilov, N. Lychkovskaya, A. Nikitenko[108,109], V. Popov, A. Zhokin, M. Chadeeva[17], S. Polikarpov[17], V. Rusinov, V. Andreev, M. Azarkin, M. Kirakosyan, A. Terkulov, A. Belyaev, E. Boos, M. Dubinin[95], L. Dudko, A. Ershov, A. Gribushin, A. Kaminskiy, V. Klyukhin, O. Kodolova[110], S. Obraztsov, S. Petrushanko, V. Savrin, A. Snigirev, V. Blinov[17], T. Dimova[17], A. Kozyrev[17], O. Radchenko[17], Y. Skovpen[17], I. Azhgirey, V. Kachanov, D. Konstantinov, R. Ryutin, S. Slabospitskii, A. Uzunian, A. Babaev, V. Borshch, D. Druzhkin[111], E. Tcherniaev

[†] *Deceased*

[1] *Also at Yerevan State University, Yerevan, Armenia*

[2] *Also at TU Wien, Vienna, Austria*

[3] *Also at Institute of Basic and Applied Sciences, Faculty of Engineering, Arab Academy for Science, Technology and Maritime Transport, Alexandria, Egypt*

[4] *Also at Ghent University, Ghent, Belgium*

[5] *Also at Universidade do Estado do Rio de Janeiro, Rio de Janeiro, Brazil*

[6] *Also at Universidade Estadual de Campinas, Campinas, Brazil*

[7] *Also at Federal University of Rio Grande do Sul, Porto Alegre, Brazil*

[8] *Also at UFMS, Nova Andradina, Brazil*

[9] *Also at Nanjing Normal University, Nanjing, China*

[10] *Now at The University of Iowa, Iowa City, Iowa, U.S.A.*

[11] *Also at University of Chinese Academy of Sciences, Beijing, China*

[12] *Also at China Center of Advanced Science and Technology, Beijing, China*

[13] *Also at University of Chinese Academy of Sciences, Beijing, China*

[14] *Also at China Spallation Neutron Source, Guangdong, China*

[15] *Now at Henan Normal University, Xinxiang, China*

[16] *Also at Université Libre de Bruxelles, Bruxelles, Belgium*

[17] *Also at another institute formerly covered by a cooperation agreement with CERN*

[18] *Also at Helwan University, Cairo, Egypt*

[19] *Now at Zewail City of Science and Technology, Zewail, Egypt*

[20] *Also at British University in Egypt, Cairo, Egypt*

[21] *Now at Ain Shams University, Cairo, Egypt*

[22] *Also at Purdue University, West Lafayette, Indiana, U.S.A.*

[23] *Also at Université de Haute Alsace, Mulhouse, France*

[24] *Also at another institute or international laboratory covered by a cooperation agreement with CERN*

[25] *Also at The University of the State of Amazonas, Manaus, Brazil*

[26] *Also at Erzincan Binali Yildirim University, Erzincan, Turkey*

[27] *Also at University of Hamburg, Hamburg, Germany*

[28] *Also at RWTH Aachen University, III. Physikalisches Institut A, Aachen, Germany*

[29] *Also at Bergische University Wuppertal (BUW), Wuppertal, Germany*

[30] *Also at Brandenburg University of Technology, Cottbus, Germany*

[31] *Also at Forschungszentrum Jülich, Juelich, Germany*

[32] *Now at RWTH Aachen University, III. Physikalisches Institut A, Aachen, Germany*

[33] *Also at CERN, European Organization for Nuclear Research, Geneva, Switzerland*

[34] *Also at Institute of Physics, University of Debrecen, Debrecen, Hungary*

[35] *Also at HUN-REN ATOMKI - Institute of Nuclear Research, Debrecen, Hungary*

[36] *Now at Universitatea Babes-Bolyai - Facultatea de Fizica, Cluj-Napoca, Romania*

[37] *Also at MTA-ELTE Lendület CMS Particle and Nuclear Physics Group, Eötvös Loránd University, Budapest, Hungary*

[38] *Also at HUN-REN Wigner Research Centre for Physics, Budapest, Hungary*

[39] *Also at Physics Department, Faculty of Science, Assiut University, Assiut, Egypt*

[40] *Also at Punjab Agricultural University, Ludhiana, India*

[41] *Also at University of Visva-Bharati, Santiniketan, India*

[42] *Also at Indian Institute of Science (IISc), Bangalore, India*

[43] *Also at Birla Institute of Technology, Mesra, Mesra, India*

[44] *Also at IIT Bhubaneswar, Bhubaneswar, India*

[45] *Also at Institute of Physics, Bhubaneswar, India*

[46] *Also at University of Hyderabad, Hyderabad, India*

[47] *Also at Deutsches Elektronen-Synchrotron, Hamburg, Germany*

[48] *Also at Isfahan University of Technology, Isfahan, Iran*

[49] *Also at Sharif University of Technology, Tehran, Iran*

[50] *Also at Department of Physics, University of Science and Technology of Mazandaran, Behshahr, Iran*

[51] *Also at Department of Physics, Isfahan University of Technology, Isfahan, Iran*

[52] *Also at Department of Physics, Faculty of Science, Arak University, ARAK, Iran*

[53] *Also at Italian National Agency for New Technologies, Energy and Sustainable Economic Development, Bologna, Italy*
[54] *Also at Centro Siciliano di Fisica Nucleare e di Struttura Della Materia, Catania, Italy*
[55] *Also at Università degli Studi Guglielmo Marconi, Roma, Italy*
[56] *Also at Scuola Superiore Meridionale, Università di Napoli 'Federico II', Napoli, Italy*
[57] *Also at Fermi National Accelerator Laboratory, Batavia, Illinois, U.S.A.*
[58] *Also at Luleå University of Technology, Luleå, Sweden*
[59] *Also at Ain Shams University, Cairo, Egypt*
[60] *Also at Consiglio Nazionale delle Ricerche - Istituto Officina dei Materiali, Perugia, Italy*
[61] *Now at CERN, European Organization for Nuclear Research, Geneva, Switzerland*
[62] *Also at Institut de Physique des 2 Infinis de Lyon (IP2I), Villeurbanne, France*
[63] *Also at Department of Applied Physics, Faculty of Science and Technology, Universiti Kebangsaan Malaysia, Bangi, Malaysia*
[64] *Also at Consejo Nacional de Ciencia y Tecnología, Mexico City, Mexico*
[65] *Also at Trincomalee Campus, Eastern University, Sri Lanka, Nilaveli, Sri Lanka*
[66] *Also at Saegis Campus, Nugegoda, Sri Lanka*
[67] *Also at Università di Perugia , Perugia, Italy*
[68] *Now at INFN Sezione di Pisa , Pisa, Italy*
[69] *Now at Università di Pisa , Pisa, Italy*
[70] *Also at National Centre for Physics, Quaid-I-Azam University, Islamabad, Pakistan*
[71] *Also at National and Kapodistrian University of Athens, Athens, Greece*
[72] *Also at Ecole Polytechnique Fédérale Lausanne, Lausanne, Switzerland*
[73] *Also at Universität Zürich, Zurich, Switzerland*
[74] *Also at Stefan Meyer Institute for Subatomic Physics, Vienna, Austria*
[75] *Also at Laboratoire d'Annecy-le-Vieux de Physique des Particules, IN2P3-CNRS, Annecy-le-Vieux, France*
[76] *Also at Near East University, Research Center of Experimental Health Science, Mersin, Turkey*
[77] *Also at Konya Technical University, Konya, Turkey*
[78] *Also at Izmir Bakircay University, Izmir, Turkey*
[79] *Also at Adiyaman University, Adiyaman, Turkey*
[80] *Also at Bozok Universitetesi Rektörlügü, Yozgat, Turkey*
[81] *Also at Marmara University, Istanbul, Turkey*
[82] *Also at Milli Savunma University, Istanbul, Turkey*
[83] *Also at Kafkas University, Kars, Turkey*
[84] *Now at Istanbul Okan University, Istanbul, Turkey*
[85] *Also at Hacettepe University, Ankara, Turkey*
[86] *Also at Istanbul University - Cerrahpasa, Faculty of Engineering, Istanbul, Turkey*
[87] *Also at Yildiz Technical University, Istanbul, Turkey*
[88] *Also at Vrije Universiteit Brussel, Brussel, Belgium*
[89] *Also at School of Physics and Astronomy, University of Southampton, Southampton, United Kingdom*
[90] *Also at IPPP Durham University, Durham, United Kingdom*
[91] *Also at Monash University, Faculty of Science, Clayton, Australia*
[92] *Also at Università di Torino, Torino, Italy*
[93] *Also at Bethel University, St. Paul, Minnesota, U.S.A.*
[94] *Also at Karamanoğlu Mehmetbey University, Karaman, Turkey*
[95] *Also at California Institute of Technology, Pasadena, California, U.S.A.*
[96] *Also at United States Naval Academy, Annapolis, Maryland, U.S.A.*
[97] *Also at Bingol University, Bingol, Turkey*
[98] *Also at Georgian Technical University, Tbilisi, Georgia*
[99] *Also at Sinop University, Sinop, Turkey*
[100] *Also at Erciyes University, Kayseri, Turkey*
[101] *Also at Horia Hulubei National Institute of Physics and Nuclear Engineering (IFIN-HH), Bucharest, Romania*
[102] *Now at VINCA Institute of Nuclear Sciences, University of Belgrade, Belgrade, Serbia*
[103] *Now at Another institute formerly covered by a cooperation agreement with CERN*
[104] *Also at Texas A&M University at Qatar, Doha, Qatar*

[105] *Also at Kyungpook National University, Daegu, Korea*
[106] *Also at Institute of Nuclear Physics of the Uzbekistan Academy of Sciences, Tashkent, Uzbekistan*
[107] *Also at Northeastern University, Boston, Massachusetts, U.S.A.*
[108] *Also at Imperial College, London, United Kingdom*
[109] *Now at Yerevan Physics Institute, Yerevan, Armenia*
[110] *Also at Yerevan Physics Institute, Yerevan, Armenia*
[111] *Also at Universiteit Antwerpen, Antwerpen, Belgium*